

NATIONAL CENTRE FOR NUCLEAR RESEARCH

DOCTORAL THESIS

Search for a new light boson in meson
decays

Author:

Damian PSZCZEL

Supervisor:

Prof. dr. hab. Joanna STEPANIAK

*A thesis submitted in fulfilment of the requirements
for the degree of Doctor of Philosophy*

October 2017

"There is no first principle which is in itself unknowable, not to be captured by a flash of insight (...) The difficulty has its seat in the empirical side (...) Sometimes we see an elephant, and sometimes we do not. The result is that an elephant, when present, is noticed."

Alfred North Whitehead

NATIONAL CENTRE FOR NUCLEAR RESEARCH

Abstract

Doctor of Philosophy

Search for a new light boson in meson decays

by Damian PSZCZEL

The data sample used in this work was collected by the WASA-at-COSY collaboration in proton-proton collisions at 1.4 GeV kinetic beam energy. The experiment took place in 2012 at Forschungszentrum Jülich in Germany at the COSY storage ring. An internal proton beam interacted with a pellet target of frozen hydrogen.

We implemented a set of selection criteria in order to extract the $\eta \rightarrow e^+e^-\gamma$ event candidates. This is a rare electromagnetic decay of the η meson with branching ratio equal to $6.9 \cdot 10^{-3}$. The resulting set of events served as the basis for three analysis.

First, we extracted the η transition form factor that is a function depending on the inner quark and gluon structure of the meson. We implemented a specific method to reduce the contribution of background channels from direct pion production.

The second analysis was the search for a narrow structure on the e^+e^- invariant mass in the selected sample of $\eta \rightarrow e^+e^-\gamma$ candidates. Many theoretical models and some astrophysical and particle physics measurements suggest the existence of a new boson, also called the dark photon, that couples to both dark and to Standard Model particles. This particle would decay to e^+e^- pairs of well defined mass and therefore could be detected by looking for narrow peaks in the e^+e^- invariant mass spectra. Since no statistically significant signal was observed, we set an upper limit on the coupling parameter ϵ^2 .

The third objective of this work was to select a sample of $\eta \rightarrow e^+e^-$ candidates. This is a very rare decay and therefore sensitive to physics beyond the Standard Model. No signal from $\eta \rightarrow e^+e^-$ was observed, therefore we were able to set an upper limit on the branching ratio for this decay.

Streszczenie

Dane wykorzystane w tej pracy zostały zebrane przez zespół badawczy WASA-at-COSY w zderzeniach proton-proton przy energii kinetycznej wiązki 1.4 GeV. Eksperyment został przeprowadzony w 2012 w Forschungszentrum Jülich w Niemczech z użyciem pierścienia akumulacyjnego COSY. Wewnętrzna wiązka protonów oddziaływała z tarczą złożoną ze spadających zamrożonych kropeł wodoru.

Opracowaliśmy zbiór warunków selekcyjnych mających na celu wyodrębnienie kanału $\eta \rightarrow e^+e^-\gamma$. Jest to rzadki elektromagnetyczny rozpad mezonu η , ze stosunkiem rozgałęzień równym $6,9 \cdot 10^{-3}$. Zbiór wybranych w ten sposób zdarzeń stanowi podstawę do trzech przeprowadzonych analiz.

Po pierwsze, zmierzaliśmy czynnik przejścia mezonu η , który zależy od jego wewnętrznej struktury kwarkowo-gluonowej. Zastosowaliśmy specjalną metodę odcinającą wkład od kanałów z bezpośrednią produkcją pionów.

Druga analiza polegała na poszukiwaniu wąskiej struktury w rozkładzie masy niezmienniczej e^+e^- dla próbki przypadków-kandydatów na rozpad $\eta \rightarrow e^+e^-\gamma$. Wiele teoretycznych modeli jak również niektóre pomiary astrofizyczne wskazują możliwość istnienia nowego bozonu, zwanego także ciemnym fotonem, który sprzęgałby się zarówno do cząstek ciemnej materii jak i do cząstek Modelu Standardowego. Bozon ten, mógłby rozpadać się na pary e^+e^- o dobrze zdefiniowanej masie, byłyby więc możliwe do odkrycia poprzez poszukiwanie wąskich struktur w rozkładzie masy niezmienniczej e^+e^- . Ponieważ nie zaobserwowaliśmy statystycznie znaczącego sygnału - postawiliśmy górną granicę na parametr sprzężenia ϵ^2 .

Trzecim celem tej pracy było wybranie próbki zdarzeń-kandydatów na rozpad $\eta \rightarrow e^+e^-$. Jest to bardzo rzadki proces i z tego powodu wyjątkowo czuły na wkład od fizyki spoza Modelu Standardowego. Nie zaobserwowaliśmy sygnału z kanału $\eta \rightarrow e^+e^-$ co umożliwiło nam postawienie górnego ograniczenia na stosunek rozgałęzień dla tego rozpadu.

Acknowledgements

I would like to express my gratitude to all people without whom this thesis would not have been possible.

First of all, I would like to thank my supervisor Prof. Joanna Stepaniak for hours spent discussing about all the small and bigger problems that came out during the realization of this work. Her deep understanding of physics concatenated with an incredible amount of patience were my major assets during all those years of scientific investigations. Thank You very much Professor for the pleasant atmosphere You create everywhere You are.

I am also sincerely grateful to my “Swedish” supervisor dr.hab. Andrzej Kupść for his wise suggestions and enormous knowledge that he was always willing to share.

Special thanks to Marcin Berłowski, for his incredible insight, critical mind and huge help in solving my many frustrating technical issues.

I would also like to thank all the smart people that I had the chance to discuss with during my PhD studies, Andrzej Pyszniak, Lena Heijkenskjöld, Wojciech Krzemień, Carl-Oscar Gullström, Józef Złomańczuk, Patrick Adlarson, Volker Hejny, Paweł Marciniewski, Magnus Wolke, Tord Johansson, Kjell Eriksson, Florian Bergmann and many others.

A very special thanks to my grandmother for the delicious meals that kept me in good health during most difficult moments...

Thank you Bartłomiej Fałkowski for the joyful moments that we shared and for all the nightlong discussions about physics and the mysteries of the universe.

Last but not least, I want to thank my parents, my brother and my beloved wife for their continuous support and especially for the extraordinary patience they shown while I was working on this thesis.

Contents

Abstract	ii
Acknowledgements	iv
Contents	v
List of Figures	viii
List of Tables	xii
Abbreviations	xiii
1 Theory and motivation	1
1.1 The Standard Model	1
1.2 The η meson and its decay channels	2
1.3 Dark matter and search for a new light boson	3
1.4 Dalitz decays of pseudoscalar mesons	5
1.4.1 Form factors	6
1.4.1.1 Electromagnetic form factor	6
1.4.1.2 Transition form factor	6
1.4.1.3 Vector Meson Dominance model	7
1.4.2 Search for dark photon in $\pi^0 \rightarrow e^+e^-\gamma$ channel	8
1.4.3 $\eta \rightarrow e^+e^-\gamma$ channel	10
1.5 Rare leptonic decays of pseudoscalar mesons	12
1.5.1 $\pi^0 \rightarrow e^+e^-$ channel	13
1.5.2 $\eta \rightarrow e^+e^-$ channel	14
1.6 Analysis outlook	14
2 Experimental set-up	16
2.1 The COSY storage ring	16
2.2 The WASA detector	17
2.2.1 Pellet Target	18
2.2.2 Central Detector	19
2.2.2.1 Mini Drift Chamber	20
2.2.2.2 Plastic Scintillator Barrel	21

2.2.2.3	Superconducting solenoid	21
2.2.2.4	Scintillating Electromagnetic Calorimeter	22
2.2.3	Forward Detector	24
2.2.3.1	Forward Window Counter	25
2.2.3.2	Forward Proportional Chamber	25
2.2.3.3	Forward Trigger Hodoscope	26
2.2.3.4	Forward Range Hodoscope	26
2.3	The Data Acquisition and Trigger System	27
2.4	Description of the trigger	29
3	Event reconstruction	30
3.1	Energy Calibration	30
3.1.1	Forward Range Hodoscope energy calibration	30
3.1.1.1	Non-uniformity calibration.	30
3.1.1.2	Non-linearity calibration.	31
3.1.2	The energy calibration of the Central Detector.	32
3.2	Track reconstruction in MDC	35
4	Monte Carlo simulations	36
4.1	Pluto simulation framework	36
4.2	WASA Monte Carlo	37
4.3	Production of the η meson	37
4.4	The decays of η meson	39
4.4.1	The $\eta \rightarrow \gamma\gamma$ decay channel	39
4.4.2	The $\eta \rightarrow e^+e^-\gamma$ decay channel	41
4.4.3	The $\eta \rightarrow \pi^+\pi^-\pi^0$ decay channel	43
4.4.4	The $\eta \rightarrow \pi^0\pi^0\pi^0$ decay channel	43
4.4.5	The $\eta \rightarrow \pi^+\pi^-\gamma$ decay channel	43
4.5	Direct production of π mesons	43
4.5.1	The $pp \rightarrow pp\pi^+\pi^-$ reaction channel	43
4.5.2	The $pp \rightarrow pp\pi^0\pi^0$ reaction channel	44
4.5.3	The $pp \rightarrow pp\pi^+\pi^-\pi^0$ reaction channel	44
5	Data set	45
5.1	Initial data sample reduction.	45
5.2	Normalization with $\eta \rightarrow \gamma\gamma$ channel	49
5.3	Analysis of the main trigger.	56
5.3.1	Trigger efficiency	57
5.3.1.1	Trigger efficiency: $\eta \rightarrow \gamma\gamma$ channel.	57
5.3.1.2	Trigger efficiency: $\eta \rightarrow e^+e^-\gamma$ channel.	58
5.3.2	Trigger stability	58
6	Analysis of $\eta \rightarrow e^+e^-\gamma$ channel	60
6.1	Multiplicity conditions.	60
6.2	Time conditions.	65
6.3	Particle identification method.	66
6.3.1	ΔE -p method - basics.	66
6.3.2	ΔE -p method - developed procedure.	67

6.4	Rejection of the background from external pair production	70
6.5	Selection based on total missing energy versus total missing mass plot.	72
6.6	Angular distributions in the $\eta \rightarrow e^+e^-\gamma$ channel	73
6.6.1	Angle between the η meson and the beam direction in laboratory frame.	73
6.6.2	Angle between γ^* and γ in η meson rest frame.	74
6.7	Summary of the $\eta \rightarrow e^+e^-\gamma$ selection	76
6.8	Radius of closest approach after selection.	76
6.9	Method for non- η background suppression.	77
6.10	Combinatorial background.	80
6.10.1	Estimation of the number of random coincidences	80
6.10.2	Invariant mass distribution of random coincidences	82
7	Analysis of $\eta \rightarrow e^+e^-$ channel	83
7.1	Summary of $\eta \rightarrow e^+e^-$ selection criteria	83
7.2	Selection of $\eta \rightarrow e^+e^-$ event candidates	86
7.2.1	$pp \rightarrow pp\pi^+\pi^-$ background	86
7.2.2	$\eta \rightarrow e^+e^-\gamma$ background	86
7.2.3	Baryonic resonance background	86
7.2.4	Combinatorial background	87
7.2.5	Data selection	87
7.3	Summary of $\eta \rightarrow e^+e^-$ selection	87
8	Results and Discussion	89
8.1	Determination of the transition form factor.	89
8.1.1	Background subtraction using $\eta \rightarrow e^+e^-\gamma$ selection cuts.	89
8.1.2	Background subtraction using the fit to two proton missing mass distribution.	93
8.2	Constraint on the $U - \gamma$ coupling.	98
8.3	Results from $\eta \rightarrow e^+e^-$ channel	104
8.4	Summary and outlook	109

List of Figures

1.1	Elementary particles	1
1.2	Pseudoscalar meson nonet	3
1.3	Positron fraction in cosmic rays	4
1.4	Feynman diagram of the $\eta \rightarrow e^+e^-\gamma$ decay	6
1.5	Feynman diagram of the $\eta \rightarrow e^+e^-\gamma$ decay in the VMD model	8
1.6	Invariant mass of e^+e^- from $\pi^0 \rightarrow e^+e^-\gamma$ decay	9
1.7	Upper limits of $(\epsilon^2, m_{A'})$ parameter space	9
1.8	Experimental determination of η transition form factor from $\eta \rightarrow \mu^+\mu^-\gamma$.	10
1.9	Experimental determination of η transition form factor	11
1.10	$P \rightarrow l^+l^-$ decay	12
1.11	Theoretical predictions of $BR(\pi^0 \rightarrow e^+e^-)$ and KTeV experimental value .	13
2.1	The COSY facility	17
2.2	The WASA set-up	18
2.3	The WASA coordinate system	18
2.4	The WASA Pellet Target	19
2.5	The MDC detector	20
2.6	Transverse sections of forward, central and backward parts of the PS detector	21
2.7	A longitudinal detection module of PS and the light guides (D)	21
2.8	The 3D model of the central part of the PS surrounding the MDC detector	22
2.9	Calculated distribution of the magnetic flux density in the SCS	23
2.10	The electromagnetic calorimeter of WASA	23
2.11	SEC module, light guide and the photomultiplier tube	24
2.12	Angular coverage of the calorimeter layers	24
2.13	The Forward Window Counter detector	25
2.14	The Forward Proportional Chamber detector	26
2.15	The Forward Trigger Hodoscope detector	26
2.16	Schematic view of the Forward Range Hodoscope detector	27
2.17	The data acquisition system	28
2.18	The trigger system	28
3.1	Illustration of non-uniformity in FRH	31
3.2	Energy deposits FRH2 vs FRH1	32
3.3	Non-linearity fitting graphical interface	33
3.4	Energy deposit in calorimeter versus $q/e \times$ momentum.	34
3.5	Calorimeter calibration plot	34
4.1	The cross section for $pp \rightarrow pp\eta$ and $pp \rightarrow pp\eta'$	38

4.2	The mechanism of $pp \rightarrow pp\eta$ production	39
4.3	Monte Carlo simulation (Pluto) for 10^6 events: proton kinetic energy	39
4.4	Monte Carlo simulation (Pluto) for 10^6 events: proton θ angle	40
4.5	Monte Carlo simulation (Pluto) for 10^6 events: θ angle of the η meson	40
4.6	Monte Carlo simulation (Pluto) for 10^6 events: angle between dilepton and photon in the laboratory frame	41
4.7	Geometrical variables involved in the description of a Dalitz process in PLUTO	42
4.8	Effect of the transition form factor on the invariant mass of e^+e^- spectra	42
4.9	Missing mass of two protons for $pp \rightarrow pp\pi^+\pi^-\pi^0$	44
5.1	Missing mass of two proton-like tracks in FD	46
5.2	Time difference between charged tracks in FD	46
5.3	Missing mass of two protons - selection with charged decays	48
5.4	Missing mass of two protons - selection with neutral decays	48
5.5	Missing mass of two protons vs invariant mass of two photons - selection with neutral decays	49
5.6	The invariant mass of $\gamma\gamma$: data and $\eta \rightarrow \gamma\gamma$ Monte Carlo simulation (WMC).	50
5.7	The invariant mass of $\gamma\gamma$: data and simulations	52
5.8	The invariant mass of $\gamma\gamma$: fit with different binning	53
5.9	The invariant mass of $\gamma\gamma$: fit with different fit range	54
5.10	List of triggers	56
5.11	The trigger stability	59
6.1	Invariant mass of two charged particles system (with the assumption of electron masses): $5 \cdot 10^6 \eta \rightarrow e^+e^-\gamma$ events	61
6.2	Invariant mass of two charged particles system (with the assumption of electron masses): $8 \cdot 10^5 \eta \rightarrow \pi^+\pi^-\gamma$ events	62
6.3	Invariant mass of two charged particles system (with the assumption of electron masses): $1 \cdot 10^7 \eta \rightarrow \gamma\gamma$ events	62
6.4	Invariant mass of two charged particles system (with the assumption of electron masses): $14 \cdot 10^6 pp \rightarrow pp\pi^+\pi^-$ events	63
6.5	Invariant mass of two charged particles system (with the assumption of electron masses): $1 \cdot 10^6 pp \rightarrow pp\pi^+\pi^-\pi^0$ events	63
6.6	Invariant mass of two charged particles system (with the assumption of electron masses): $1 \cdot 10^7 pp \rightarrow pp\pi^0 (\rightarrow \gamma\gamma) \pi^0 (\rightarrow e^+e^-\gamma)$ events	64
6.7	Invariant mass of two charged particles system (with the assumption of electron masses): $10^6 pp \rightarrow p\Delta^+ \rightarrow ppe^+e^-$ events	64
6.8	Cuts applied on the time differences of particles in CD and FD.	65
6.9	Effect of temporal cuts relative to protons in FD on the time difference between particles in CD.	66
6.10	Energy deposit in SEC versus charge \times momentum plot - data	67
6.11	Energy deposit in CD versus charge \times momentum plot - graphical cut	67
6.12	Particle identification fit	68
6.13	Normalized distances from the e^+ fitted line	69
6.14	Photon conversion into e^+e^- in the beam pipe material	70
6.15	Radius of closest approach versus the invariant mass of e^+e^- at the beam pipe.	71

6.16	Data with conversion graphical cut	71
6.17	Total missing energy versus total missing mass for $\eta \rightarrow \pi^+\pi^-\gamma$ simulation	72
6.18	Total missing energy versus total missing mass for $\eta \rightarrow e^+e^-\gamma$ simulation	72
6.19	Total missing energy versus total missing mass for $pp \rightarrow pp\pi^+\pi^-$ simulation	73
6.20	Total missing energy versus total missing mass for $pp \rightarrow pp\pi^+\pi^-\pi^0$ simulation	73
6.21	Theta angle of η meson in laboratory reference frame - Monte Carlo simulations	74
6.22	Theta angle of η meson in laboratory reference frame - data	75
6.23	Distributions of the angle between γ^* and γ in η rest frame.	75
6.24	Radius of closest approach	76
6.25	Missing mass of two protons versus invariant mass of e^+e^- (data)	78
6.26	Global fit to the missing mass of two protons	78
6.27	Fits to eight 50 MeV/ c^2 slices in protons missing mass	79
6.28	Invariant mass of e^+e^- - extracted η content	79
6.29	Charged tracks multiplicity after particle identification	81
6.30	Invariant mass of e^+e^- distribution for combinatorial background	82
7.1	Angle between e^+e^- pair (laboratory frame): $\eta \rightarrow e^+e^-$ simulation	84
7.2	Energy of e^+ and e^- : $\eta \rightarrow e^+e^-$ simulation	84
7.3	Illustration of angular condition applied for data and $\eta \rightarrow e^+e^-$ simulation.	87
7.4	Illustration of energy condition applied for data and $\eta \rightarrow e^+e^-$ simulation.	87
7.5	Illustration of invariant mass condition applied for data and $\eta \rightarrow e^+e^-$ simulation.	88
8.1	Direct form factor determination (20 MeV/ c^2 bin width): Sample A.	91
8.2	Direct form factor determination (20 MeV/ c^2 bin width): Sample B.	91
8.3	Direct form factor determination (20 MeV/ c^2 bin width): Sample C.	91
8.4	Transition form factor fits for 20 MeV/ c^2 bin width	91
8.5	Direct form factor determination (40 MeV/ c^2 bin width): Sample A.	92
8.6	Direct form factor determination (40 MeV/ c^2 bin width): Sample B.	92
8.7	Direct form factor determination (40 MeV/ c^2 bin width): Sample C.	92
8.8	Transition form factor fits for 40 MeV/ c^2 bin width	92
8.9	Form factor resulting from fit based background subtraction	93
8.10	Form factor fit based background subtraction (bin width modified for 0 – 100 MeV/ c^2)	94
8.11	Form factor fit based background subtraction (bin width modified for 100– 400 MeV/ c^2)	95
8.12	Form factor comparison between this work and other measurements	97
8.13	Invariant mass of e^+e^- - data and background simulations	98
8.14	Invariant mass of e^+e^- - difference between data and sum of background Monte Carlo simulations	99
8.15	Illustration of reconstruction effects	100
8.16	Smearing and acceptance effects for different M_U values	101
8.17	Upper limit on β as a function of U boson mass M_U	102
8.18	Upper limit on ϵ^2 as a function of e^+e^- invariant mass (systematics)	103
8.19	Upper limit on ϵ^2 as a function e^+e^- invariant mass	103
8.20	Fit to the $\eta \rightarrow e^+e^-$ missing mass distribution	104

8.21	2 MeV/c ² bin width	105
8.22	5 MeV/c ² bin width	105
8.23	10 MeV/c ² bin width	105
8.24	Fits to the two protons missing mass (530 – 560 MeV/c ² mass range)	105
8.25	2 MeV/c ² bin width	106
8.26	5 MeV/c ² bin width	106
8.27	10 MeV/c ² bin width	106
8.28	Fits to the two protons missing mass (530 – 580 MeV/c ² mass range)	106
8.29	2 MeV/c ² bin width	107
8.30	5 MeV/c ² bin width	107
8.31	10 MeV/c ² bin width	107
8.32	Fits to the two protons missing mass (520 – 590 MeV/c ² mass range)	107

List of Tables

1.1	Non-exhaustive list of pseudoscalar mesons	2
1.2	Decay modes of η	3
1.3	Theoretical predictions of $\eta \rightarrow e^+e^-$ branching ratio	14
2.1	Basic characteristics of the PT system	19
2.2	Stopping power of the FRH for different particles	27
5.1	Effect of the selection conditions	47
5.2	Events in the final sample	49
5.3	Number of η mesons ($/10^6$) extracted from fits with second order polynomial	52
5.4	Number of η mesons ($/10^6$) extracted from fits with third order polynomial	52
5.5	Number of η mesons ($/10^6$) extracted from fits without additional polynomial	55
5.6	Number of η mesons ($/10^6$) extracted from fits without additional polynomial	55
5.7	Neutral selection trigger combinations	58
5.8	Charged selection trigger combinations	58
6.1	$\eta \rightarrow e^+e^-\gamma$ and background reactions	76
7.1	$\eta \rightarrow e^+e^-$ and background reactions	88
8.1	Results of the form factor fits	90
8.2	Results of the form factor fits	96
8.3	FF fits from various experiments	97
8.4	Results of the BR_{limit} fits	108

Abbreviations

BR	B ranching R atio
SM	S tandard M odel
QCD	Q uantum C hromo D ynamics
QED	Q uantum E lectro D ynamics
ChPT	C hiral P erturbation T heory
COSY	C Ooler S Ynchrotron
WASA	W ide A ngle S hower A pparatus
WMC	W ASA M onte C arlo
FD	F orward D etector
FDC	F orward D etector C harged particle
FRH	F orward R ange H odoscope
FWC	F orward W indow C ounter
FPC	F orward P roportional C hamber
FTH	F orward T rigger H odoscope
FVH	F orward V eta H odoscope
CD	C entral D etector
PSB	P lastic S cintillator B arrel
MDC	M ini D rift C hamber
SEC	S cintillating E lectromagnetic C alorimeter
PT	P ellet T arget
CDC	C entral D etector C harged particle
CDN	C entral D etector N eutral particle
SEC	S cintillator E lectromagnetic C alorimeter

To my parents, my wife and my brother...

Chapter 1

Theory and motivation

1.1 The Standard Model

The Standard Model (SM) is a physical theory developed in the latter 20th century. It describes the reality as emerging from different combinations of 12 elementary particles, quarks and leptons (left side of figure 1.1), that interact through the exchange of 5 so called gauge bosons (right side of figure 1.1).

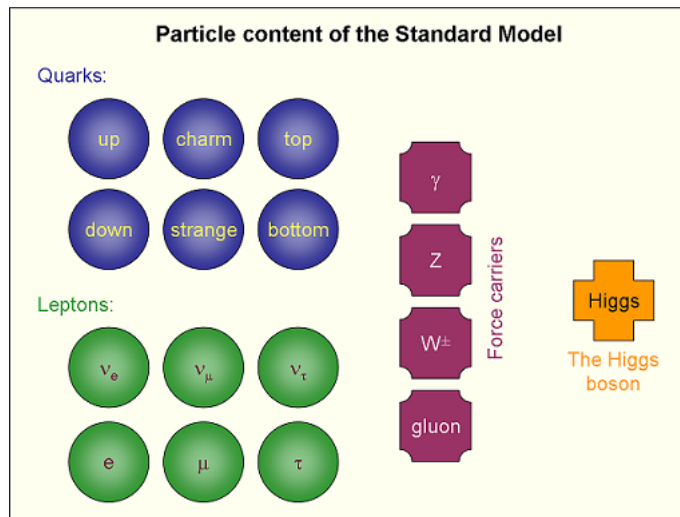


FIGURE 1.1: Elementary particles.

The Higgs boson occupies a special place in this picture for it is responsible for particle masses. Its recent (2012) discovery at CERN (Aad et al. [1], Chatrchyan et al. [2]) reaffirmed the SM is one of the most successful physical model of all time.

TABLE 1.1: Non-exhaustive list of pseudoscalar mesons

Particle	Quark content	Mass (MeV/c ²)	I^G	J^{PC}	Mean lifetime (ns)
π^+/π^-	$u\bar{d}/\bar{u}d$	139.57	1^-	0^-	2.6×10^{-8}
π^0	$\frac{u\bar{u}-d\bar{d}}{\sqrt{2}}$	134.97	1^-	0^{-+}	8.52×10^{-17}
η	$\frac{u\bar{u}+d\bar{d}-s\bar{s}}{\sqrt{3}}$	547.86	0^+	0^{-+}	5.02×10^{-19}
K^+/K^-	$u\bar{s}/\bar{u}s$	493.68	$\frac{1}{2}$	0^-	1.24×10^{-8}
K_S^0	$\frac{d\bar{s}-s\bar{d}}{\sqrt{2}}$	497.61	$\frac{1}{2}$	0^-	8.95×10^{-11}
K_L^0	$\frac{d\bar{s}+s\bar{d}}{\sqrt{2}}$	497.61	$\frac{1}{2}$	0^-	5.12×10^{-8}

1.2 The η meson and its decay channels

The etymology of the word *meson* comes from the Greek *mesos* which means *middle*. Hideki Yukawa, in the 1930s, first used this term to characterize particles with masses between those of electrons and protons. Those particles are known today as pions (π mesons). Mesons interact strongly so they are hadrons and they are composed of quark-anti-quark pair thus their baryon number is zero.

The η particle is a pseudoscalar meson. The list of pseudoscalar mesons, along with their basic characteristics such as the quark content, mass, mean lifetime, isospin (I), G-parity (G), total angular momentum (J), parity (P) and C-parity (C) is presented in table 1.1. The total spin of pseudoscalars is zero and they have odd parity $J^P = 0^-$. The pseudoscalar mesons consisting of up, down, and strange quarks only - pions, kaons, η and η' mesons - form a nonet (see figure 1.2). In terms of the SU(3) flavour symmetry group, introducing a mixing angle θ , one can represent the η meson as a superposition of a singlet and an octet states η_1 and η_8 :

$$|\eta_1\rangle = \frac{1}{\sqrt{3}}(u\bar{u} + d\bar{d} + s\bar{s}) \quad (1.1)$$

$$|\eta_8\rangle = \frac{1}{\sqrt{6}}(u\bar{u} + d\bar{d} - 2s\bar{s}) \quad (1.2)$$

and (see Kullander et al. [3])

$$|\eta\rangle = \cos\theta |\eta_8\rangle - \sin\theta |\eta_1\rangle \approx \frac{1}{\sqrt{3}}u\bar{u} + d\bar{d} - s\bar{s} \quad (1.3)$$

TABLE 1.2: Decay modes of η

Decay mode	Branching ratio
$\eta \rightarrow \gamma\gamma$	$(39.41 \pm 0.20)\%$
$\eta \rightarrow \pi^0\pi^0\pi^0$	$(32.68 \pm 0.23)\%$
$\eta \rightarrow \pi^+\pi^-\pi^0$	$(22.92 \pm 0.28)\%$
$\eta \rightarrow \pi^+\pi^-\gamma$	$(4.22 \pm 0.08)\%$
$\eta \rightarrow e^+e^-\gamma$	$(6.9 \pm 0.4) \times 10^{-3}$

where the θ value estimations vary between -15.4° (Feldmann et al. [4]) and -18.4° (Hsiao et al. [5]) while combined BABAR and CLEO data provide $\theta \sim -16.84^\circ$.

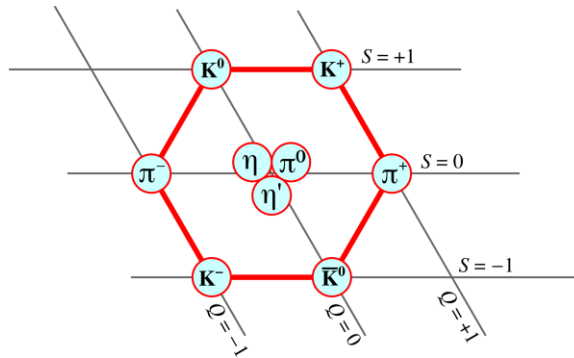


FIGURE 1.2: Pseudoscalar meson nonet.

The approximation that the three lightest quarks (u, d and s) have zero masses leads to an exact $SU(3)$ flavour symmetry, also known as chiral symmetry of the quantum chromodynamical (QCD) Lagrangian. In this picture, the pseudoscalar mesons would be the massless Goldstone bosons¹. Since we know that quark masses are non zero, this symmetry is broken and the pseudoscalar mesons acquire their masses.

The lifetime of the η (see 1.1) meson is relatively long since all its strong, electromagnetic and weak decays are forbidden in the first-order (C, CP, G parity conservation). Its main decay channels are shown in table 1.2.

1.3 Dark matter and search for a new light boson

The SM of particle physics provides a very satisfactory description of the interactions between fields and matter that fill the space we live in. However, the unexplained nature of Dark Matter motivates searches for an extension of this model to a more fundamental

¹Only η' meson would have a non zero mass.

theory. One of many possible approaches to solve this issue consists in introducing the concept of the Dark Sector.

Dark Sector particles interact weakly with the usual matter through one or more mediators that are coupled to the SM via a *portal*. There are different types of portals depending on the mediator spin and parity - scalar, pseudoscalar, fermion or vector. Some astrophysics observations such as the positron and/or electron excesses observed by PAMELA (Adriani et al. [6]) (see spectra in figure 1.3 from Adriani et al. [7]), ATIC (Chang et al. [8]), H.E.S.S. (Aharonian et al. [9]) and AMS (Vecchi [10]) as well as the narrow 0.511 MeV γ ray emission from the galactic bulge observed by INTEGRAL (Jean et al. [11]) may indicate the presence of new undiscovered particles that decay to e^+e^- pairs. Those measurements are our principal motivation to focus on the hypothetical vector portal and its associated vector mediator.

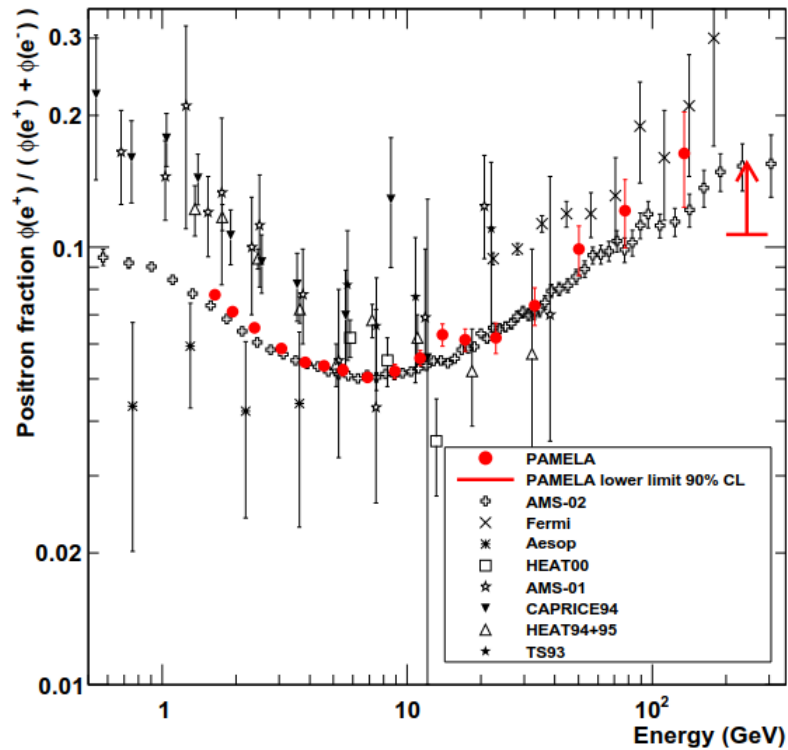


FIGURE 1.3: Positron fraction in cosmic rays (see Adriani et al. [7]).

The hypothesis of a new boson solving the problem of the dark matter content in the Universe is an idea that emerged in the 80's. Multiple authors postulated an extra $U(1)_{dark}$ abelian gauge field and the associated light vector boson, also called the dark photon, in the $\mathcal{O}(\text{MeV}-\text{GeV})$ mass range, as a possible extension of the SM (Fayet [12], Dobroliubov and Ignatiev [13], Boehm and Fayet [14]).

The dark photon is a vector field A'_μ with Lagrangian:

$$\mathcal{L}_{A'} = -\frac{1}{4}F'^{\mu\nu}F'_{\mu\nu} + \frac{\epsilon}{2\cos\theta_W}B^{\mu\nu}F'_{\mu\nu} - \frac{1}{2}m_{A'}^2 A'^{\mu}A'_{\mu} \quad (1.4)$$

where $F'_{\mu\nu} \equiv \partial_{\mu}A'_{\nu} - \partial_{\nu}A'_{\mu}$ is the dark photon field strength and $B_{\mu\nu} \equiv \partial_{\mu}B_{\nu} - \partial_{\nu}B_{\mu}$ is the SM hypercharge field strength. This model of the minimal kinetically mixed dark photon (Alexander et al. [15]) is parametrized by the dark photon mass $m_{A'}$ and the kinetic mixing parameter ϵ . For $m_{A'}$ in the range of MeV-GeV, the dominant effect of this kinetic mixing (after electroweak symmetry breaking) is an analogous mixing with the SM electromagnetic field strength $F^{\mu\nu}$ expressed by $\frac{\epsilon}{2}F'_{\mu\nu}F^{\mu\nu}$. The result of this mixing is that the dark photon acquires a coupling of strength ϵe to the electromagnetic current.

1.4 Dalitz decays of pseudoscalar mesons

A (single) Dalitz decay of a pseudoscalar meson, also called a conversion decay, is shown in figure 1.4 for η . The meson decays into one real and one virtual photon. The latest converts into a lepton-antilepton pair (electrons or muons). The squared four-momentum of the virtual photon, \mathbf{q}^2 is equal to the invariant mass of the resulting l^+l^- system:

$$\mathbf{q}^2 = M_{l^+l^-}^2 = (E_{l^+} + E_{l^-})^2 - (\mathbf{p}_{l^+} + \mathbf{p}_{l^-})^2 \quad (1.5)$$

where E denotes the particle energy and \mathbf{p} its momentum vector.

In the point-like QED approximation, the differential cross section² of the Dalitz decay is given by:

$$\frac{d\Gamma_{P \rightarrow l^+l^-\gamma}}{dq^2 d\Gamma_{P \rightarrow \gamma\gamma}} = \frac{2\alpha}{3\pi q^2} \sqrt{1 - \frac{4m_l^2}{q^2}} \left(1 + \frac{2m_l^2}{q^2}\right) \left(1 - \frac{q^2}{M_P^2}\right)^{3/2} \quad (1.6)$$

The equation 1.6 holds as long as we neglect the inner structure of the pseudoscalar meson, i.e. its quark and gluon content. In section 1.4.1 we will describe the formalism used to take into account this effect.

²Normalized with respect to the double photon channel.

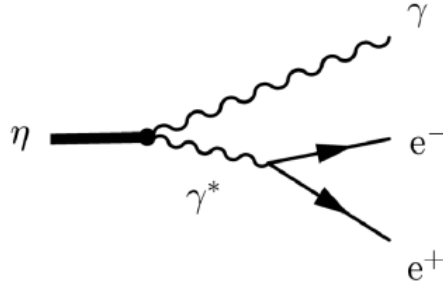


 FIGURE 1.4: Feynman diagram of the $\eta \rightarrow e^+e^-\gamma$ decay.

1.4.1 Form factors

1.4.1.1 Electromagnetic form factor

When we consider the scattering on charged composite particles, we need to take into account the inner electromagnetic structure of those objects. Quantum electrodynamics (QED) allows us to calculate the interaction properties of point-like particles. The inner electromagnetic structure of a composite particle can be represented by a function called the *form factor*. The differential cross-section for the scattering of an electron (elementary point-like particle) with a composite particle (such as protons, mesons, etc) can then be written in the form:

$$\frac{d\sigma}{dq^2} = \left| \frac{d\sigma}{dq^2} \right|_{QED} |F(q^2)|^2 \quad (1.7)$$

where $\left| \frac{d\sigma}{dq^2} \right|_{QED}$ is the differential cross-section for the scattering of an electron on another point-like charged particle calculated in the QED framework, and $F(q^2)$ is the electromagnetic form factor function depending on the transferred four-momentum q . In the non-relativistic limit, the electromagnetic form factor is the Fourier transform of the charge distribution function.

1.4.1.2 Transition form factor

In subsection 1.4.1.1, we have seen how to determine the electromagnetic form factor of a non-elementary charged particle - we basically just need to bombard it with a structureless particle such as electrons and calculate the deviation of the observed differential cross-section with respect to theoretical predictions. For a pseudoscalar meson such as η this is more complicated because it is short-lived and electrically neutral. Moreover,

the conservation of C-parity forbids the processes involving neutral mesons and a single-photon exchange.

In order to investigate the inner (quark and gluon) structure of a pseudoscalar meson we have to adopt a more subtle approach. We study the decay of the form:

$$\eta \rightarrow \gamma + \gamma^* \rightarrow \gamma + e^+ + e^- \quad (1.8)$$

This is the Dalitz decay of the η meson. As already seen in 1.4, it involves two photons - one real, massless, and one virtual with non-zero mass that converts into an electron-positron pair³. The term *transition* is generally used in processes such as $A \rightarrow B\gamma$ where A and B are neutral mesons. The *transition form factor* describes the effects of the electromagnetic dynamic structure arising at the *transition vertex* of this process. The Dalitz decay is a special case since it only involves one neutral meson. Therefore, the corresponding *transition form factor* depends only on the electromagnetic structure of this meson. The virtual photon carries a time-like > 0 four-momentum q , which is defined by 1.5. The probability of formation of a lepton pair with some mass $m_{e^+e^-}$ is proportional to the probability of emission of a virtual photon with four-momentum q . In case of a Dalitz decay $q = m_{e^+e^-}$. Analogically to the approach presented in section 1.4.1.1, we can express the invariant mass spectrum of e^+e^- system as a product of two contributions: a QED part corresponding to the point-like approximation (see equation 1.6) and the *transition form factor* that contains the effect of the inner structure of the η meson.

1.4.1.3 Vector Meson Dominance model

In the 60's, J.J. Sakurai predicted the existence of vector mesons coupled to the hadronic isospin and hypercharge currents (?]).

The VMD model was introduced in order to explain the fact that the interaction between (energetic) photons and hadrons is much more intense than expected by the sole interaction of photons with the hadron's electric charge⁴. The model tries to solve this issue by assuming that the photon ($J^P = 1^-$) is a superposition of the pure electromagnetic photon which interacts only with electric charges and neutral vector mesons (also $J^P = 1^-$). It follows that the interaction between photons and hadrons occurs by the exchange of vector mesons and it is these mesons that give rise to the enhancement⁵.

³More generally, lepton-antilepton pair.

⁴Moreover, the interaction between photons and protons is comparable to the interaction of photons with neutrons in spite of the difference of their electric charge structure.

⁵Through their resonant, i.e. possessing a complex pole, propagators.

This effect is especially well pronounced in the case of time-like photons ($q^2 > 0$) when the squared 4-momentum approaches the squared mass of one of the vector meson (e.g. $q^2 \approx m_\rho^2$).

Therefore, in the framework of the VMD model the form factor takes the form of:

$$F(q^2) = \sum_V \frac{M_V^2}{M_V^2 - q^2 - iM_V\Gamma_V(q^2)} \cong \frac{1}{1 - \frac{q^2}{M_V^2}} \quad (1.9)$$

where $V = \rho, \omega, \phi$ ⁶, $\Gamma_V(q^2)$ is the total width and M_V the mass of the vector meson, q^2 was already described by 1.5.

The illustration of the VMD model in case of $\eta \rightarrow e^+e^-\gamma$ decay is shown in figure 1.5. One can compare it to the diagram from figure 1.4.

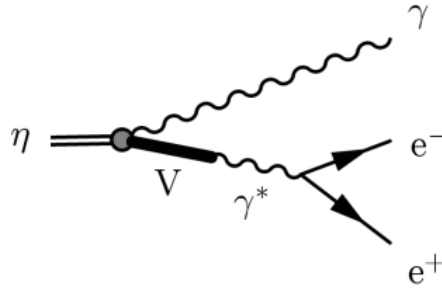


FIGURE 1.5: Feynman diagram of the $\eta \rightarrow e^+e^-\gamma$ decay in the VMD model.

The equation 1.9 is often used as a fit function. The M_V vector meson mass is replaced by a free parameter Λ and, for convenience, the value of Λ^{-2} (sometimes called b_η) is provided as result of form factor calculations.

1.4.2 Search for dark photon in $\pi^0 \rightarrow e^+e^-\gamma$ channel

The search for a dark photon was already performed by WASA-at-COSY collaboration in the $\pi^0 \rightarrow e^+e^-\gamma$ channel. The results were published in Adlarson et al. [16]. The idea of the analysis was to search for a narrow structure in the invariant mass spectrum of e^+e^- pair (see figure 1.6) for dark photon mass in 20-100 MeV/ c^2 range (less than twice the muon mass). For $\epsilon^2 > 10^{-6}$ the average path traveled by a dark photon emitted in a low energy π^0 decay should be less than a millimeter, therefore we are, in principle, able to detect its decay inside our detector. Neglecting higher-order electromagnetic and

⁶For the energy range considered in our experiment the most important contribution originates from the ρ meson.

tiny weak contributions and assuming that the dark photon doesn't decay to light dark scalars and/or fermions, the total width of the dark photon can be expressed as:

$$\Gamma_{A'} = \Gamma_{A' \rightarrow e^+e^-} = \frac{1}{3} \alpha \epsilon^2 m_{A'} \sqrt{1 - \frac{4m_e^2}{m_{A'}^2}} \left(1 + \frac{2m_e^2}{m_{A'}^2}\right) \quad (1.10)$$

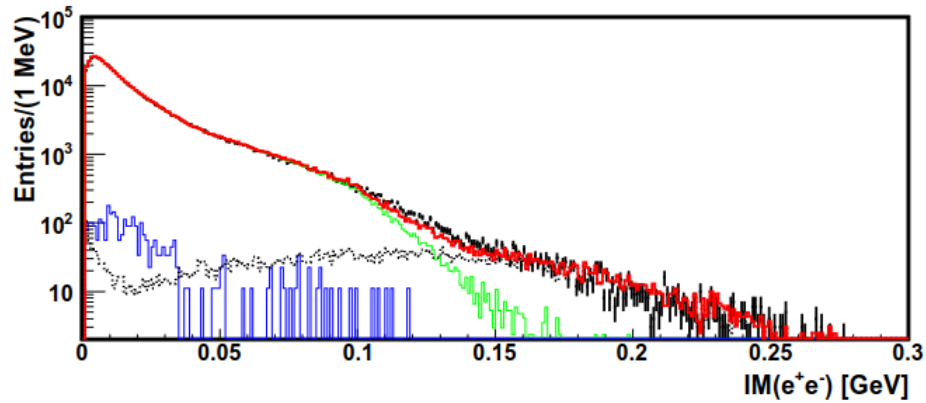


FIGURE 1.6: Invariant mass of e^+e^- from $\pi^0 \rightarrow e^+e^-\gamma$ decay from Adlarson et al. [16]

A sample of $5 \cdot 10^5$ $\pi^0 \rightarrow e^+e^-\gamma$ decays were selected and since no signal from dark photon decay was observed an upper limit for the model parameters $(\epsilon^2, m_{A'})$ was established. This is shown in figure 1.7.

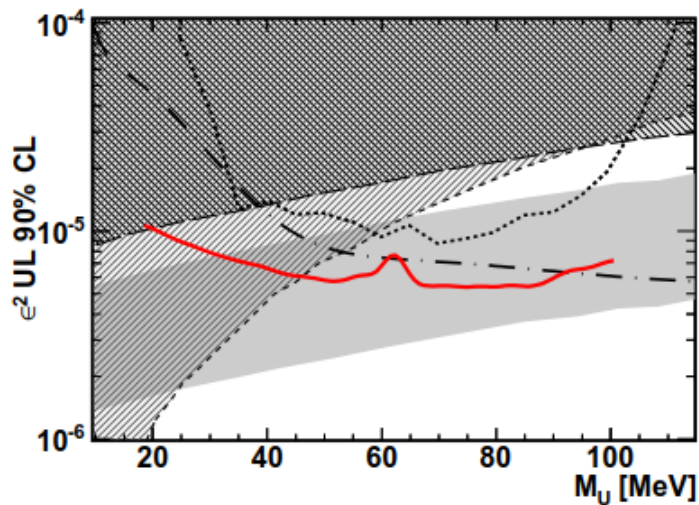


FIGURE 1.7: Upper limits of $(\epsilon^2, m_{A'})$ parameter space from Adlarson et al. [16]

1.4.3 $\eta \rightarrow e^+e^-\gamma$ channel

The first observations of $\eta \rightarrow e^+e^-\gamma$ (and $\pi^0 \rightarrow e^+e^-\gamma$) channel was performed in the 70's (Kotlewski [17] and Jane et al. [18]). They were based on limited data samples with high background contribution (mostly from photon conversion in target and set-up material). A very insightful treatment of electromagnetic decays of light mesons, including $\eta \rightarrow e^+e^-\gamma$, is presented in Landsberg [19]. The main reason for present day focus on the $\eta \rightarrow e^+e^-\gamma$ decay is related to the determination of η transition form factor. This is done through two decay modes $\eta \rightarrow e^+e^-\gamma$ and $\eta \rightarrow \mu^+\mu^-\gamma$. The latter channel was studied in IHEP with Lepton-G spectrometer (Dzhelyadin et al. [20]) and by NA60 experiment (Arnaldi et al. [21] and, more recently, Arnaldi et al. [22]). The results of Lepton-G and NA60 experiments are based on respectively 600 and 9000 event candidates and are shown, along with the VMD prediction, in figure 1.8. One can observe there is no information about the form factor below two muon masses for it corresponds to the lower kinematic limit of the squared four-momentum transfer.

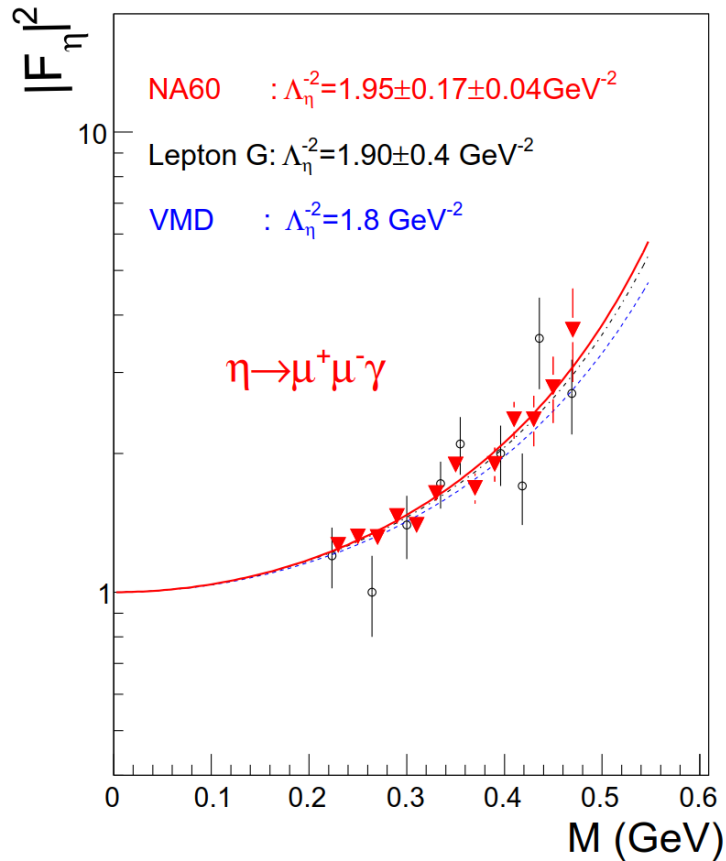


FIGURE 1.8: Results of the Lepton-G (open circles) and the NA60 (triangles) measurements of the $\eta \rightarrow \mu^+\mu^-\gamma$ decay. The solid and dashed-dotted lines are fits to the NA60 data while the dotted line is the VMD model prediction. Picture is taken from Dzhelyadin et al. [20]

The $\eta \rightarrow e^+e^-\gamma$ channel was analyzed in SND detector at VEPP-2M collider (Novosibirsk) in 1996 and 1998 (Achasov et al. [23]). Here, 109 candidates were found. Another experiment was performed at MAMI-C accelerator with Crystal Ball (CB) and TABS detectors (Berghauer et al. [24]). It collected 1345 $\eta \rightarrow e^+e^-\gamma$ candidates. Both results, along with NA60 data points and a theoretical calculation from Terschlusen and Leupold [25], are shown on figure 1.9.

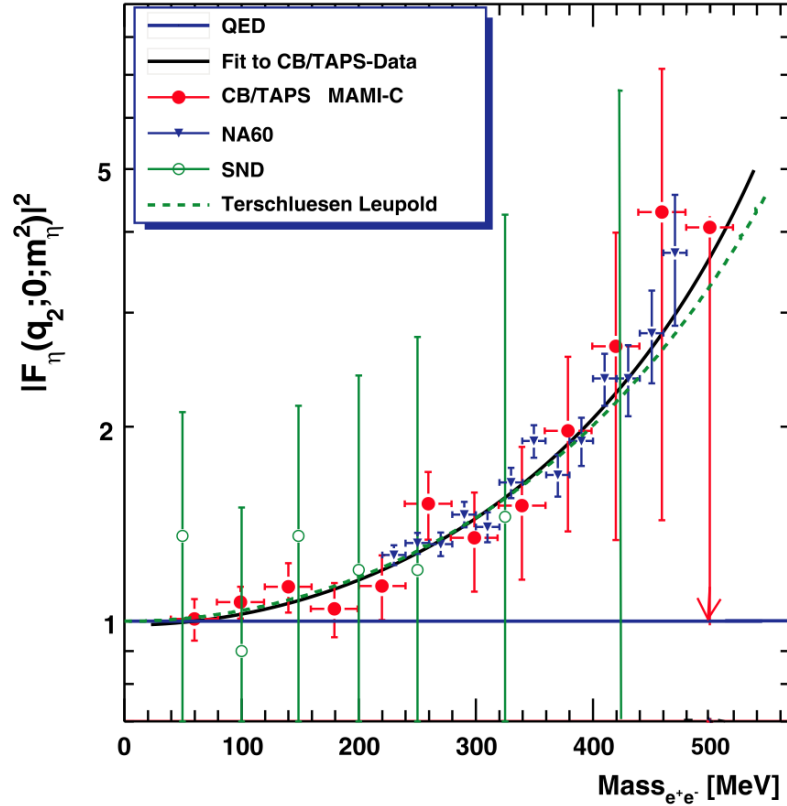


FIGURE 1.9: The red circles are the data of Berghauer et al. [24] (the black curve is the fit to the data). The green (open) circles show the result of the SND experiment (Achasov et al. [23]). The blue (inverted) triangles represent the result obtained by NA60 (Dzhelyadin et al. [20]). The green (dashed) curve is a calculation performed by Terschlusen and Leupold [25]. Picture is taken from Berghauer et al. [24]

The most precise measurements of the Λ^{-2} parameter up to date were performed by the NA60 experiment [22] $\Lambda^{-2} = (1.934 \pm 0.067_{\text{stat}} \pm 0.050_{\text{sys}}) \text{ GeV}^{-2}$ and the most recent result is from MAMI (CB/TABS detectors) [26] $\Lambda^{-2} = (1.97 \pm 0.11_{\text{tot}}) \text{ GeV}^{-2}$.

The analysis of this channel will be detailed in chapter 6. It will be a double track approach. On the one hand, we will extract the η transition form factor and on the other hand we will search for the dark photon. The latter will proceed similarly to the $\pi^0 \rightarrow e^+e^-\gamma$ analysis described in 1.4.2 as we look for a peak in the invariant mass of e^+e^- from $\eta \rightarrow e^+e^-\gamma$ decay.

1.5 Rare leptonic decays of pseudoscalar mesons

The rare leptonic decays of pseudoscalar mesons, $P \rightarrow l^+l^-$, provide a very sensitive probe of physics beyond the SM. Historically, the first decay of this type to be discovered experimentally was $\eta \rightarrow \mu^+\mu^-$ (Hyams et al. [27]). In those fourth-order electromagnetic processes, the hadron vertex is connected to the leptonic pair by two virtual photons (see figure 1.10). This decay cannot go through one virtual photon stage (tree level) since a photon cannot couple to spin 0. It is suppressed with respect to $P \rightarrow \gamma\gamma$ reaction by two orders of $\alpha \sim 10^{-2}$ for it has two more vertices. In the particular case of decay into e^+e^- , highly relativistic, the conservation of helicity reduces this branching ratio even more, by a factor of $2(m_e/m_P)^2$. Those effects are responsible for the extremely low SM value of those processes. Following Landsberg [19], the branching ratio can be written in the form:

$$\begin{aligned} BR(P \rightarrow l^+l^-) &= \Gamma(P \rightarrow l^+l^-)/\Gamma(P \rightarrow \text{all channels}) \\ &= BR(P \rightarrow \gamma\gamma) 2\alpha^2\xi^2\beta[|X|^2 + |Y|^2] \end{aligned} \quad (1.11)$$

where α is the fine structure constant, $\xi = m_l/m_P$, $\beta = (1 - 4\xi^2)^{1/2}$, X and Y are, respectively, the real (dispersive) and imaginary (absorptive) components of the normalized dimensionless amplitude in the $P \rightarrow l^+l^-$ decay. If we neglect the dispersive part, the imaginary component $|Y|^2 = \frac{1}{4}\beta^{-2} \left(\ln \frac{1+\beta^2}{1-\beta^2}\right)^2$ provides a way, using the so-called unitarity bound⁷, to set a theoretical lower limit on the branching ratio. The dispersive part diverges logarithmically for a pointlike vertex. Therefore we must introduce a cutoff related to the vertex structure, the form factor $F_P(q_{\gamma 1}^2; q_{\gamma 2}^2; m_P^2)$ (see figure 1.10). A more detailed description of the form factor is presented in section 1.4.1.

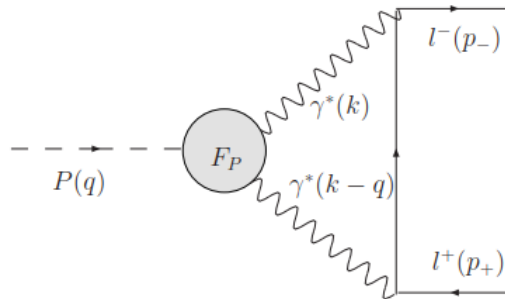


FIGURE 1.10: $P \rightarrow l^+l^-$ decay.

⁷Based on the fact that $|Y|^2 \geq (\text{Im}Y)^2$

1.5.1 $\pi^0 \rightarrow e^+e^-$ channel

The unitary bound for this channel constrains its branching ratio: $\text{BR}(\pi^0 \rightarrow e^+e^-) \geq 4.69 \times 10^{-8}$. Taking into account the data from CELLO and CLEO experiments (Behrend et al. [28]) and (Gronberg et al. [29]) to determine the form factor parameters, a value of $\text{BR}^{th}(\pi^0 \rightarrow e^+e^-) = (6.23 \pm 0.09) \times 10^{-8}$ is obtained in Dorokhov [30]. This result is 3.3σ below the experimental value from KTeV experiment at Fermilab $\text{BR}^{exp}(\pi^0 \rightarrow e^+e^-) = (7.48 \pm 0.29_{stat} \pm 0.25_{sys}) \times 10^{-8}$ (Abouzaid et al. [31]). KTeV measured 794 $\pi^0 \rightarrow e^+e^-$ events candidates where π^0 's produced and tagged by $K_L \rightarrow 3\pi^0$ reaction. This enhancement is hard to explain by SM contributions (radiative and mass corrections). On the graph 1.11 from Dorokhov [32] we see many theoretical calculations of this branching ratio (using different models), the unitary bound and the CLEO bound (form factor data) along with the experimental KTeV value.

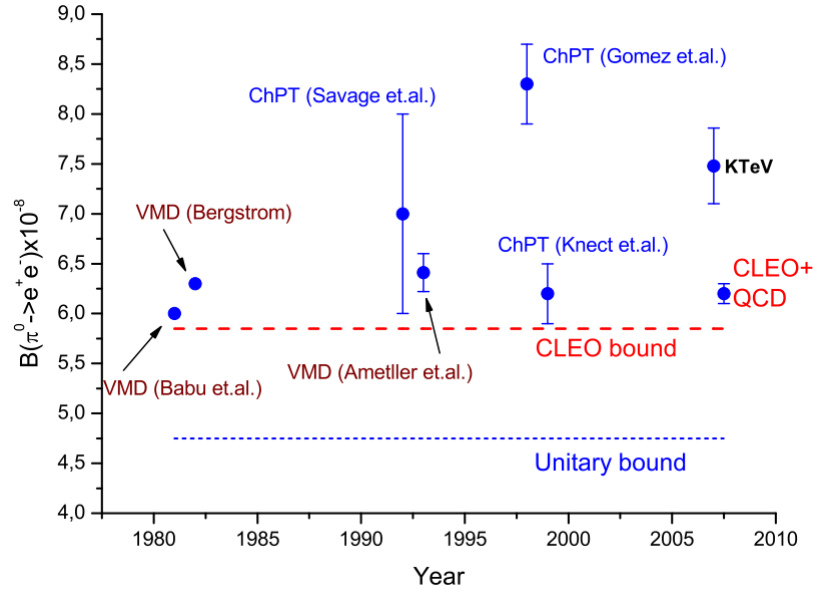


FIGURE 1.11: Theoretical predictions of $\text{BR}(\pi^0 \rightarrow e^+e^-)$ and KTeV experimental value (taken from Dorokhov [32])

Although some of the theoretical predictions Savage et al. [33] (very large uncertainties) and Gomez Dumm and Pich [34] reported in figure 1.11 are consistent with the experimental value, the result calculated by Dorokhov and Ivanov [35] in 2007 is the most precise and therefore relevant estimation to searches related to this channel.

We can neglect any weak SM contribution since the Z boson is much more massive than the pion $m_Z/m_{\pi^0} \sim 10^3$. The discrepancy between theoretical predictions and experimental results described in this section leads to speculations about the existence of yet undiscovered light particles.

TABLE 1.3: Theoretical predictions of $\eta \rightarrow e^+e^-$ branching ratio

Model	Ref	$\text{BR}(\eta \rightarrow e^+e^-) \times 10^9$
LMD large-Nc	Knecht et al. [38]	4.5 ± 0.02
CLOE+OPE	Dorokhov and Ivanov [35]	4.6 ± 0.06
Modified VMD	Petri [36]	4.65 ± 0.01
Hidden gauge	Petri [36]	4.68 ± 0.01
ChPT	Savage et al. [33]	5 ± 1
Mass corrections	Dorokhov et al. [37]	5.24
ChPT large-Nc	Gomez Dumm and Pich [34]	5.8 ± 0.2

1.5.2 $\eta \rightarrow e^+e^-$ channel

The most recent theoretical calculations of this decay branching ratio provide values around 10^{-9} . They use different models, among other ChPT (Savage et al. [33]), modified VMD, hidden gauge (Petri [36]) and take into account various corrections (such as mass correction Dorokhov et al. [37]). Those results are listed in table 1.3.

In 2008, a branching ratio upper limit of $2.7 \cdot 10^{-5}$ at 90% C.L. was established for this channel in WASA-at-CELSIUS experiment and published in Berłowski et al. [39]. WASA-at-CELSIUS set-up consisted of the same WASA detector we use in this work while it operated at the CELSIUS storage ring located in Uppsala (Sweden) at The Svedberg Laboratory. This limit was extracted from a sample of $2.41 \cdot 10^5$ η mesons produced in $pd \rightarrow {}^3\text{He} \eta$ reaction at 893 MeV incident proton energy (close to η production threshold).

The best actual upper limit is $< 4.9 \cdot 10^{-6}$ (at 90% confidence level) and it was established by HADES experiment in 2012 (Agakishiev et al. [40]). HADES operates at GSI research centre in Darmstadt (Germany). This result was based on data collected in pp collisions at 3.5 GeV.

Up till now, there are only upper limits for $\eta \rightarrow e^+e^-$ decay but if one were to determine a $\text{BR}(\eta \rightarrow e^+e^-)$ value exceeding $\sim 6 \cdot 10^{-9}$ it might be seen as a signature of physics beyond the SM.

The analysis of 2012 WASA-at-COSY data with respect to $\eta \rightarrow e^+e^-$ channel is described in chapter 7.

1.6 Analysis outlook

The structure of this work is the following. In chapter 2, we present the experimental set-up, the technical parameters of the COSY storage ring and a detailed description of

the WASA detector together with its data acquisition system. Chapter 3 is dedicated to event reconstruction i.e. the process used in WASA-at-COSY in order to extract real particle tracks from raw detector responses. In chapter 4, we describe the methods of event simulation that are used in this work. We illustrate some of reconstruction effects on those simulations and we briefly discuss about rest gas influence. Chapter 5 presents the data sample used in this work and describe the initial data reduction. Chapter 6 and chapter 7 report the analysis of, respectively, $\eta \rightarrow e^+e^-\gamma$ and $\eta \rightarrow e^+e^-$ channels based on this data sample. Results of those analysis and the related discussions are presented in chapter 8. At the end of this chapter, there is a short summary and the outlook for future activity is sketched.

Chapter 2

Experimental set-up

2.1 The COSY storage ring

COSY (**C**ooler **S**ynchrotron) is a particle accelerator coupled with a storage ring (184 m of circumference) operated by the Institute of Nuclear Physics (IKP) at Forschungszentrum Jülich in Germany. It provides polarized and unpolarized beams of protons or deuterons with momentum range between 0.3 and 3.7 GeV/c.

The schematic view of the COSY facility is shown in figure 2.1. It has the form of a race track (roman hippodrome) with two 40 m long straight sections. COSY is able to provide beams to both internal and external targets.

The isochronous cyclotron JULIC starts the acceleration process imparting up to 296 MeV/c momenta to ions. The beam is then injected into the COSY ring where it is accelerated until the desired momentum is reached. In order to reduce the phase-space volume, up to $\Delta p/p \sim 10^{-4}$, electron and stochastic cooling are implemented (see ref [41]).

The COSY ring can store around 10^{11} particles per accelerated bunch. This allows for typical luminosities around $10^{31} \text{cm}^{-2} \text{s}^{-1}$ in case of experiments with an internal target. The beam intensity is reduced due to collisions with the internal target (or beam extraction). The duration of typical acceleration cycles in case of our experiment is of the order of a few minutes. The average beam momentum also decreases with time - this effect is compensated by the use of “barrier bucket”, a nonlinear radio frequency cavity (see ref [42] for details).

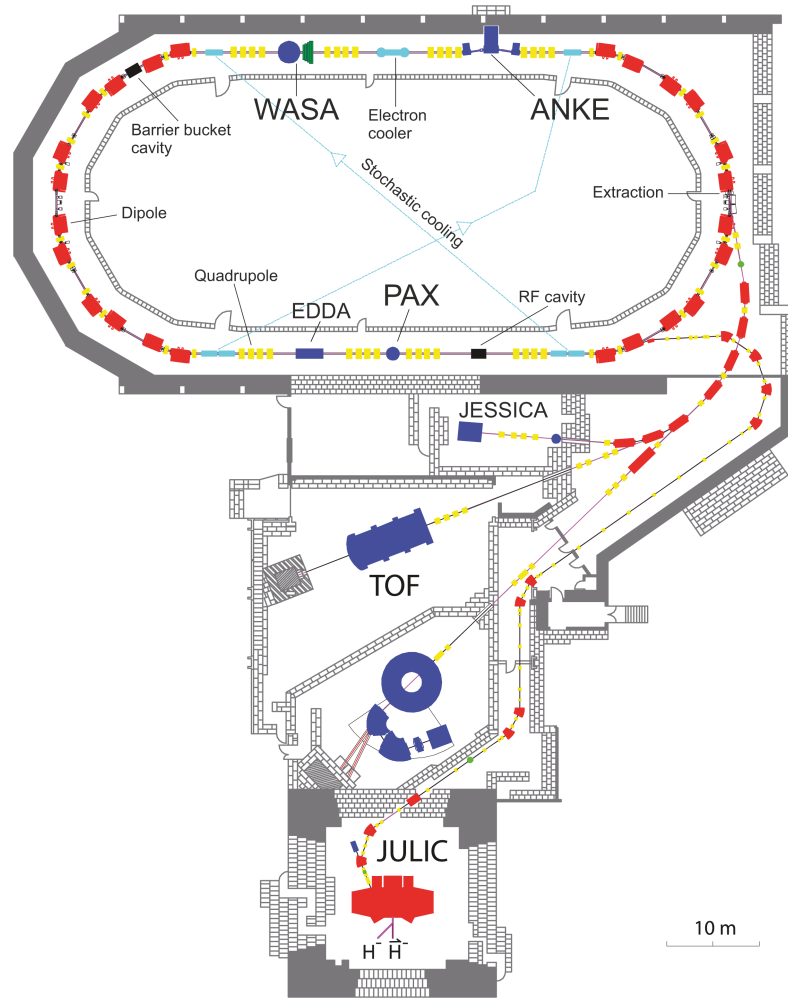


FIGURE 2.1: The COSY facility.

2.2 The WASA detector

WASA (**Wide Angle Shower Apparatus**) is a large-acceptance detector (almost 4π) for charged and neutral particles. It operated at the CELSIUS storage ring at The Svedberg Laboratory in Uppsala (Sweden) until June 2005. After the shutdown of CELSIUS, the detector was transported to COSY. Installed in summer 2006, it collected data until middle of 2014. In 2015 the central detector and the pellet target were removed while the forward detector is used as azimuthally symmetric polarimeter for the Electric Dipole Moment (EDM) experiment.

The WASA detector is an internal experiment situated at one of the straight sections of the COSY storage ring. It was designed to study rare decays of mesons (π^0 , η , η' or ω) and to investigate the structure of hadrons and symmetry breaking mechanisms. The cross section of the detector together with the acronyms of its sub-parts are shown on figure 2.2.

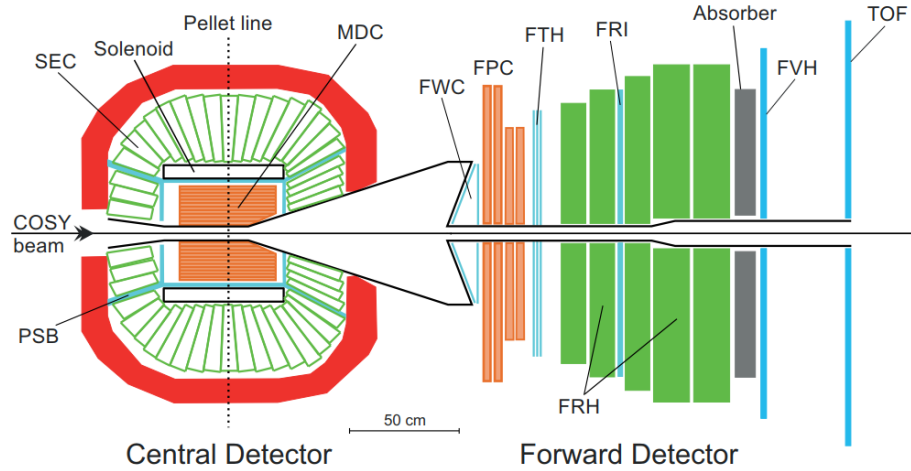


FIGURE 2.2: The WASA set-up.

In the following sections, we divide the WASA detector into three components: the pellet target (PT), the central detector (CD) and the forward detector (FD) and we describe their sub-parts.

The WASA coordinate system (used in this analysis) is sketched on figure 2.3.

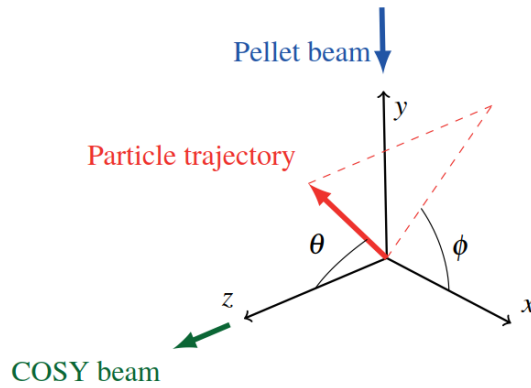


FIGURE 2.3: The WASA coordinate system

2.2.1 Pellet Target

The WASA target is based on a unique design that provides droplets of frozen hydrogen or deuterium. To form those pellets from an initial jet, a piezoelectric vibrating nozzle is used. The pellets are then collimated and injected into the scattering chamber where they freeze by evaporation¹ and interact with the accelerator beam. The pellet guiding

¹The temperature and pressure conditions in the scattering chamber are kept below the hydrogen triple point.

TABLE 2.1: Basic characteristics of the PT system

Pellet parameter	Value	units
Diameter	25 – 35	μm
Frequency	5 – 7	kHz
Velocity	70 – 80	m/s
Stream divergence	0.04	$^\circ$
Effective thickness	$\sim 10^{15}$	atoms/cm ²

tube is connected to the beam pipe COSY tube - to its top - in order to allow the pellet stream injection from above and to its bottom - to collect the droplets in the pellet beam dump.

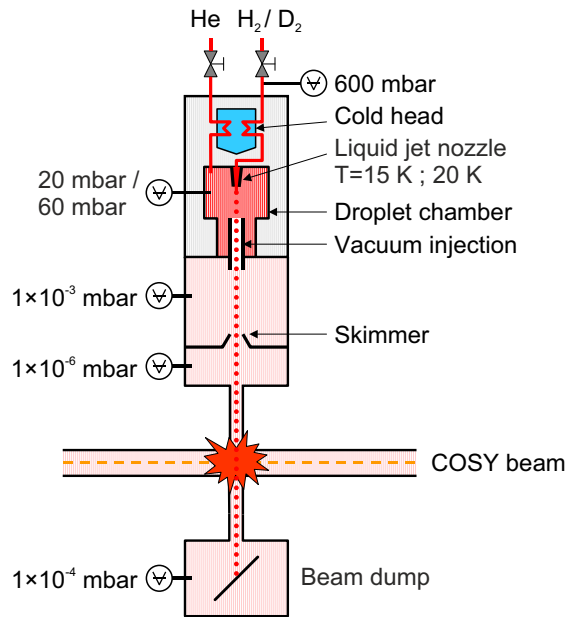


FIGURE 2.4: The WASA Pellet Target

This particular setup was developed and tested at the CELSIUS storage ring (see [43] and [44]). It allows for high luminosities (up to $10^{32} \text{ cm}^{-2} \text{ s}^{-1}$) and significantly limits the internal photon conversion inside the interaction region (IR). The system design provides the necessary space to insert the 4π detector around the IR.

A schematic description of the PT is shown in figure 2.4 and some of its basic characteristics are listed in table 2.1

2.2.2 Central Detector

The main objective of this part of the WASA detector is the detection and identification of the particles produced in the collisions of beam and pellet target streams. Those

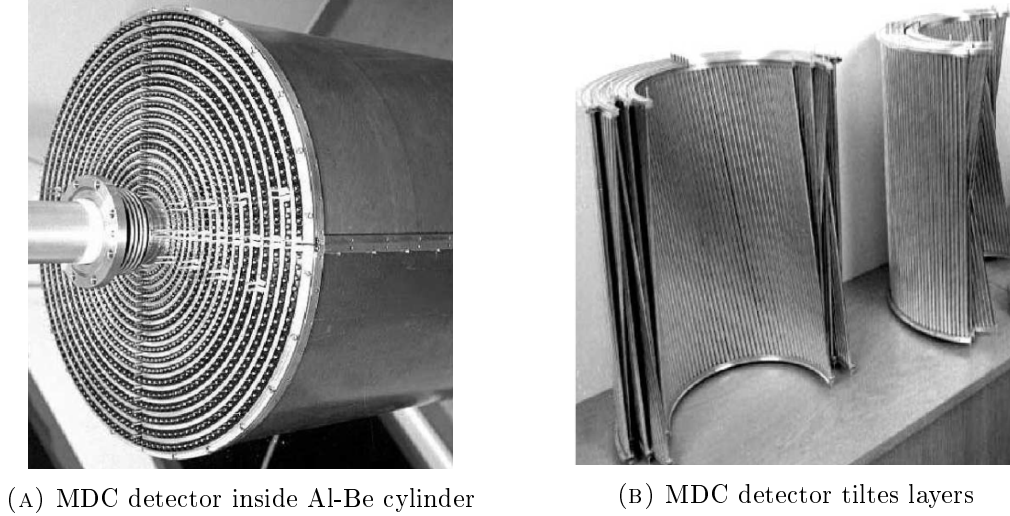


FIGURE 2.5: The MDC detector

particles are directly produced in the interaction process or indirectly as a decay product of other particles. The WASA CD, surrounding the interaction region, consists of three sub-detectors and a solenoid. It is able to measure energies and momenta of charged and neutral particles in an almost 4π solid angle range.

2.2.2.1 Mini Drift Chamber

The so-called Mini Drift Chamber (MDC) consists of 1738 aluminized Mylar drift tubes arranged in 17 cylindrical layers with layer radius between 41 mm and 204 mm (see figure 2.5a). Each straw (drift tube) is filled with a mixture of argon and methane (80%-20%) and contains a central anode made of a $20\ \mu\text{m}$ diameter gold plated tungsten wire. The diameter of those straws varies between 2 mm (five inner layers), 3 mm (six central layers) and 4 mm (six outer layers). In order to allow for z coordinate determination, the tubes in eight of the layers are slightly skewed (tilted) with respect to the beam direction (from 6° to 9°) forming a hyperboloidal shape (see figure 2.5b). The tubes in the remaining nine layers are aligned with the COSY beam axis. Each layer of straws is held in place by semi-ring plates made of Al-Be (50%-50%) alloy and the whole structure is placed inside an Al-Be cylinder.

The MDC detector surrounds the interaction region. It is used to reconstruct vertex positions and charged particle momenta, charges and energies based on the characteristic of their tracks in the magnetic field provided by the solenoid (see section 2.2.2.3). It covers a polar angle (θ on figure 2.3) range from 24° to 159° . The precision of vertex reconstruction for the scattered protons is $\sigma_{x,y} \sim 1$ mm (transverse directions) and of $\sigma_z \sim 3$ mm (beam axis). A detailed description of the MDC detector can be found in [45].

2.2.2.2 Plastic Scintillator Barrel

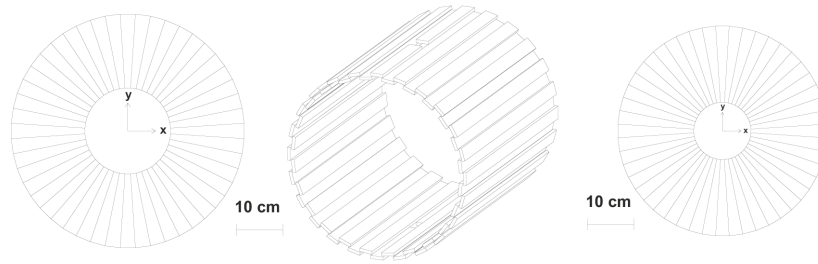


FIGURE 2.6: Transverse sections of forward, central and backward parts of the PS detector.

The PSB is a collection of thin, 8 mm thick, BC-408 plastic scintillators. It has cylindrical shape and is placed directly outside the MDC detector (see figure 2.8). The central part (PSC), made of 50 rectangular bars², forms two partially overlapping layers and surrounds the drift chamber (MDC). Its extremities are closed with forward and backward end caps each one consisting of 48 trapezoidal shaped elements. The forward end cap (PSF) is placed at 90° with respect to the beam axis and the backward cap (PSB) is inclined at 30° forming a conical shape. A longitudinal PS detection module is shown in figure 2.7 while the figure 2.6 represents its transverse section.

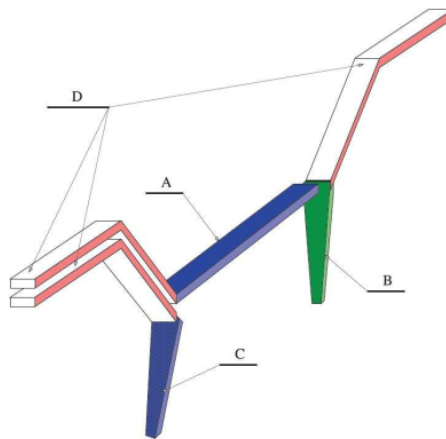


FIGURE 2.7: A longitudinal detection module formed by the forward (B), central (A), backward (C) elements of PS and the light guides (D).

2.2.2.3 Superconducting solenoid

To determine the polarity and momenta of charged particles in WASA, we need a magnetic field. Therefore a superconducting solenoid was inserted between the SEC and

²Two of the initial 48 elements are divided into two halves in order to make space for the pellet injection tube.

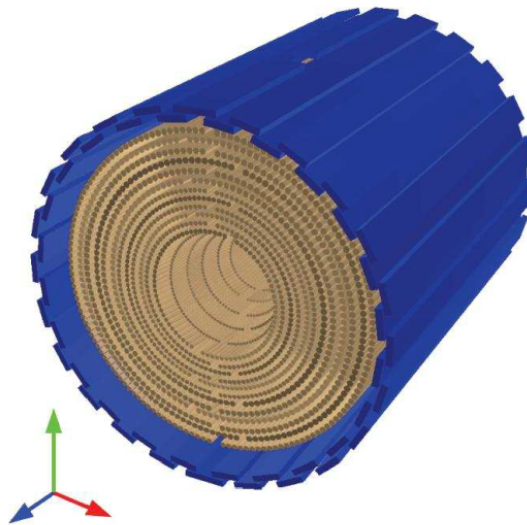


FIGURE 2.8: The 3D model of the central part of the PS (blue) surrounding the MDC detector (light brown).

the PSB detectors. It is cooled by a liquid Helium cryostat that keeps the operating temperature at 4.5 K and it provides an axial (parallel to the beam) magnetic field. The flux density in the interaction region can reach 1.3 T (see figure 2.9). The experiment that provided data for the analysis described here used a field of 1 T.

In order to reduce the negative effect on the accuracy of the energy measurements in SEC, the walls of the SCS are made of 16 mm thick aluminium which is equivalent to 0.18 radiation length. A 5 tons iron yoke, enclosing the whole CD, provide the return path for the magnetic flux. It also shields the photomultipliers from the magnetic field.

2.2.2.4 Scintillating Electromagnetic Calorimeter

The electromagnetic calorimeter (see figure 2.10) is the outermost active component of the CD placed between the solenoid and the yoke. It is formed by 1012 sodium-doped CsI scintillating crystals which have the shape of a truncated pyramid (see figure 2.11). They are arranged in 24 ring-layers along the beam axis and cover an angular range from 20° to 169° . Those layers form three groups:

- the central part (SEC) consists of 17 layers, each with 48 crystals (30 cm each)
- the forward part (SEF) consists of 4 layers, each with 36 crystals (25 cm each)
- the backward part (SEB) consist of 3 layers, two with 24 crystals and one with 12 crystals (20 cm each)

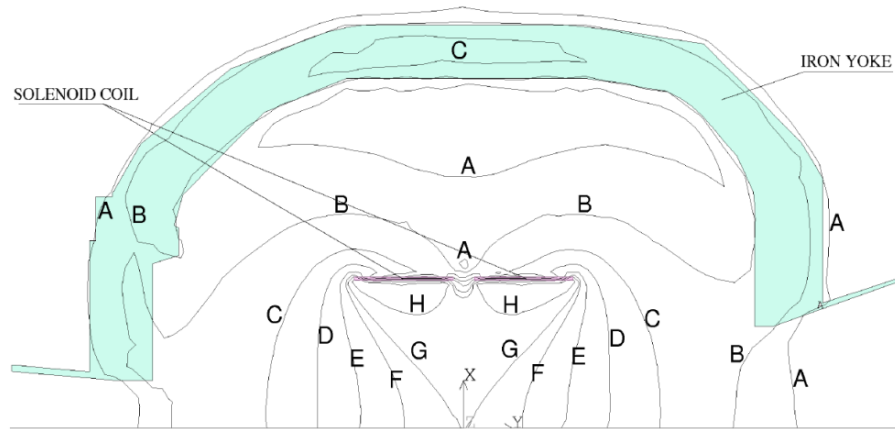


FIGURE 2.9: Calculated distribution of the magnetic flux density for a coil carrying current of 667 A (see [46]). Contour maxima are indicated by lines marked A-H, where: A=0.10 T, B=0.25 T, C=0.050 T, D=0.75 T, E=1.00 T, F=1.20 T, G=1.30 T and H=1.50 T.

The crystal length varies from SEF to SEB - it is equivalent to ~ 16 radiation lengths and ~ 0.8 of hadronic interaction length. The stopping power of the crystals is around 190 MeV for pions, 400 MeV for protons and 450 MeV for deuterons (see reference [47]). The schematic structure of the calorimeter layers and their angular coverage is shown in figure 2.12

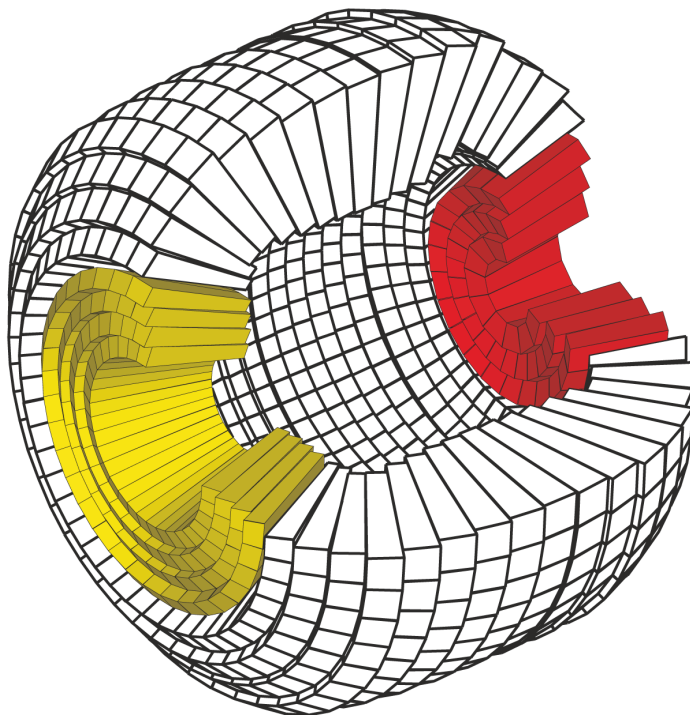


FIGURE 2.10: The electromagnetic calorimeter of WASA.



FIGURE 2.11: A fully equipped SEC module consisting of a CsI crystal, light guide and the photomultiplier tube.

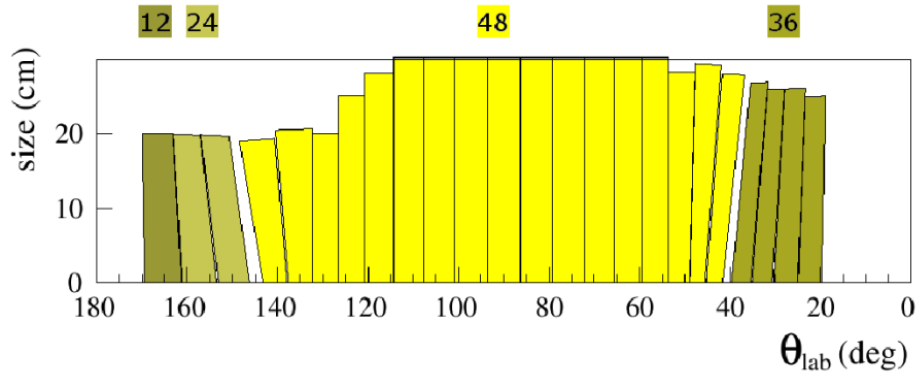


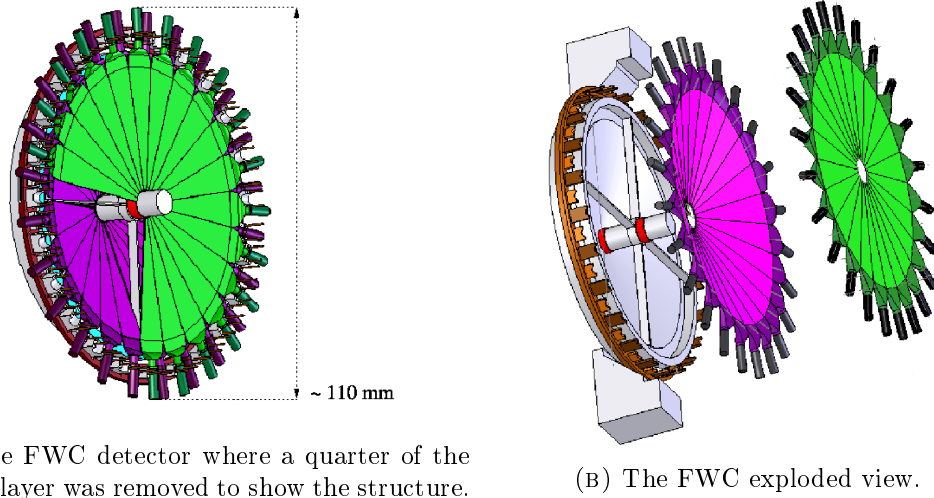
FIGURE 2.12: Angular coverage of the calorimeter layers with the number of constituting crystals indicated above.

The electromagnetic calorimeter provides information about the energy deposited along neutral or charged particle tracks and the angular parameters of those tracks (emission angles). It covers 96% of the 4π solid angle with gaps for PS light guides and for pellet injection. The energy resolution for photons is given by $\frac{\Delta E}{E} = \frac{5\%}{\sqrt{E/GeV}}$ while for charged stopped particles it is $\sim 3\%$.

The angular resolution is limited by the crystal size and thus we have $\sim 5^\circ$ resolution in polar angle and $\sim 7.5^\circ$ resolution in azimuthal angle.

2.2.3 Forward Detector

The Forward Detector (FD) is situated down-stream of the interaction region and consists of plastic scintillators (FWC, FTH, FRH and FVH) and a straw tube tracker (FPC). The FD provides information about the energy deposits and angular parameters of charged tracks, mostly scattered protons, deuterons and helium ions. The angular coverage (polar angle) of the FD detectors is $3^\circ - 18^\circ$ and the angular resolution is of about 0.2° .



(A) The FWC detector where a quarter of the second layer was removed to show the structure.

(B) The FWC exploded view.

FIGURE 2.13: The Forward Window Counter detector

2.2.3.1 Forward Window Counter

The FWC is closest to the interaction region, situated along the beam axis. It is formed by two layers of 24 pie-shaped elements (see figure 2.13). Each element is a 3 mm BC408 plastic scintillator. The first layer is inclined by 80° with respect to the beam axis (in order to be as close to the interaction region as possible). The second layer is perpendicular to the beam axis. The layers are shifted by half an element with respect to each other, resulting in an effective granularity of 48 elements.

This detector is an important part of the trigger system and for experiments with ^3He production it also provides information for particle identification.

2.2.3.2 Forward Proportional Chamber

The FPC, located right after the FWC, is a straw tube tracker made of four modules of four layers. Layers consist of 122 drift tubes each made of $26\ \mu\text{m}$ aluminized mylar and 8 mm of diameter and a stainless steel sensing wire of thickness $20\ \mu\text{m}$. The drift gas is the same as in the MDC (see section 2.2.2.1), a 80% – 20% mixture of argon and ethane.

In order to improve the efficiency of track reconstruction the orientation of the modules was shifted in the XY plane as seen on figure 2.14 at -45° (module 1), 0° (module 4), 45° (module 2) and 90° (module 3) with respect to the y -axis.

This detector provides the most precise angular information about the forward scattered particles.

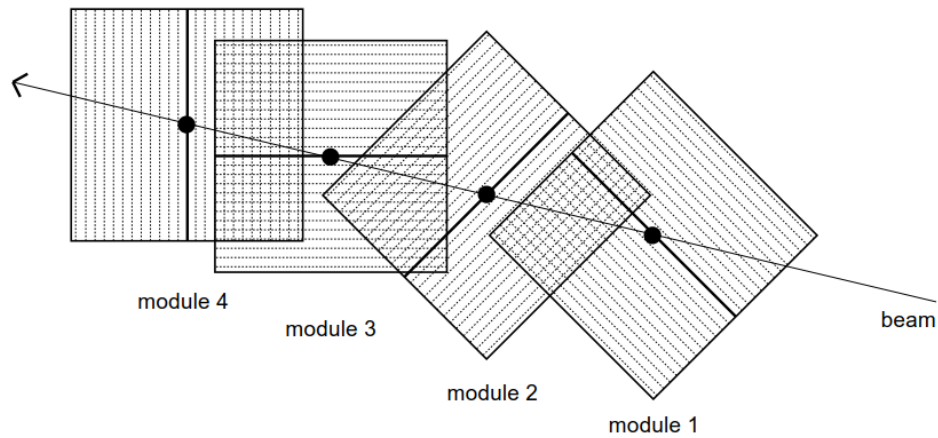


FIGURE 2.14: The Forward Proportional Chamber detector.

2.2.3.3 Forward Trigger Hodoscope

The next detector is called the Forward Trigger Hodoscope. It consists of three layers of 5 mm BC408 plastic scintillators. There are 48 pie-shaped elements in the first layer and 24 elements in the second and third layer. The shape of the last two layers is that of an Archimedian spiral - elements are oriented clockwise in the second layer and anti-clockwise in the third layer. This geometry is shown in figure 2.15. It creates a special pixel structure where each pixel correspond to a given combination of elements and layers. It allows for a fast extraction of angular information, polar and azimuthal angles, and hit multiplicities needed by the trigger system.

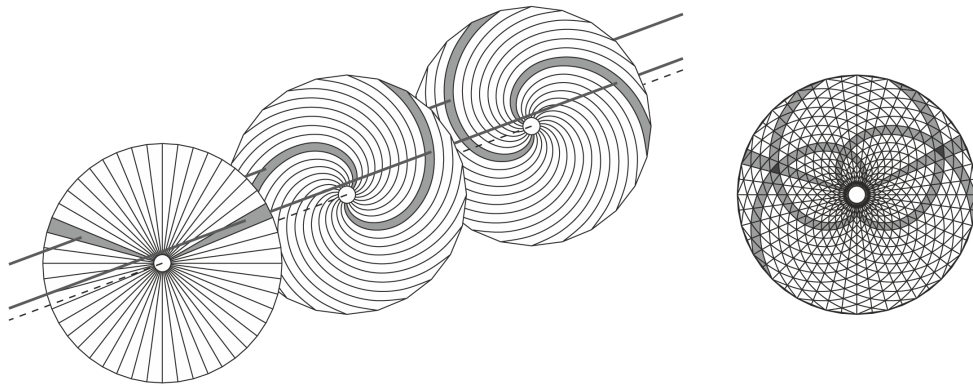


FIGURE 2.15: The Forward Trigger Hodoscope detector.

2.2.3.4 Forward Range Hodoscope

The FRH detector consists of five pie-shaped layers each made of 24 BC400 plastic scintillator elements (see figure 2.16). The first three layers have a thickness of 110 mm

TABLE 2.2: Stopping power of the FRH for different particles

Particle	Stopping power
π	200 MeV
p	360 MeV
d	450 MeV
${}^3\text{He}$	1000 MeV
${}^3\text{He}$	1100 MeV

and the last two are 150 thick. The energy resolution of stopped particles is of about 3%. The stopping power of the FRH for different particles is shown in table 2.2.

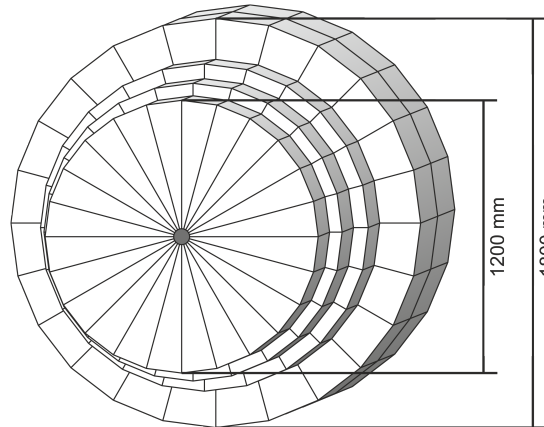


FIGURE 2.16: Schematic view of the Forward Range Hodoscope detector.

The main function of the FRH detector is the reconstruction of kinetic energies (from energy deposits) and track parameters of forward scattered particles. Using the $\Delta E - E$ method one can use the signals from different layers in order to identify those particles (f.e. disentangle between protons and deuterons). The coincidence of signals from matching azimuthal (ϕ) angle segments of FRH, FWC and FTH is used to identify the trajectories of particles.

2.3 The Data Acquisition and Trigger System

The data flow corresponding to signals from different detector elements is huge. At the designed luminosity³ of $10^{32} \text{ cm}^{-2}\text{s}^{-1}$ the event rate was estimated to be of the order of $5 \cdot 10^6$ per second (50 MHz). The size of one usual event is of the order of a few kilobytes. The data acquisition system represented on figure 2.17 is able to handle between 10 and 20 MHz. We cannot save all signals, therefore we need a trigger system that enables the disk writing for only those events that have a desired signature.

³This is an upper limit never reached in the actual experiment. Luminosity values a few times lower were achieved.

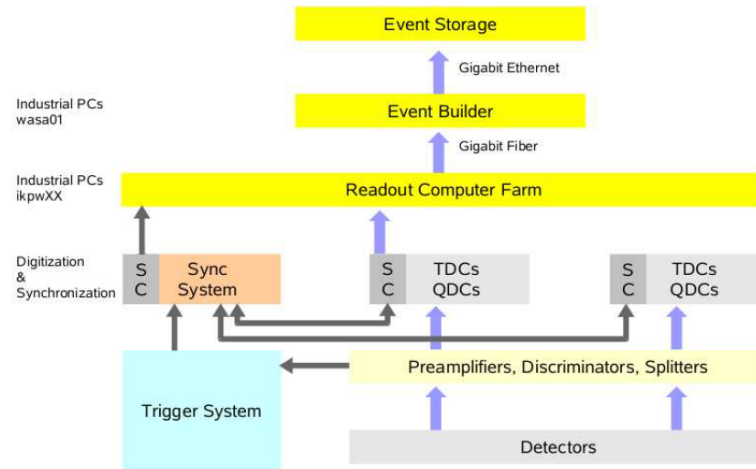


FIGURE 2.17: The data acquisition system.

The figure 2.18 illustrates the two-level organization of the trigger system. The first level⁴ consists of fast detectors such as plastic scintillators in FD and the PSB detector in CD. It is based on a set of multiplicity coincidence and track alignment conditions. It provides the time scale for the event. It is used, for example, to fix the integration gates for the QDCs. The second stage of the trigger system, slower⁵, takes into account the cluster multiplicity and the energy deposits in the electromagnetic calorimeter (SEC).

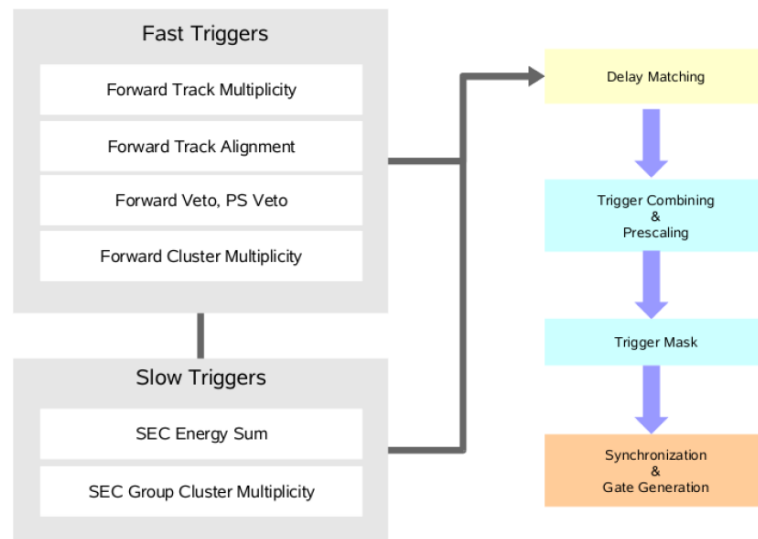


FIGURE 2.18: The trigger system.

After passing through the Delay Matching unit that corrects for the time differences between the first and second trigger level, the information from the primary triggers

⁴The first level processing time is around 200 ns

⁵The second level processing time is around 500 ns

(input triggers) is combined in order to form a more complex triggering pattern. A prescaling factor is applied to all high rate triggers in order to balance the whole setup.

2.4 Description of the trigger

The trigger (TR10) that was selecting the data set used in this work is defined as follows: fhdwr2 & frhb2 & seh2. Those acronyms stand for:

- fhdwr2 - two matching tracks in FD (geometrical overlapping and temporal coincidence between different detectors)
- frhb2 - two deposits above a defined threshold in the second layer of the FRH detector
- seh2 - two deposits above a defined (high) threshold (around 50 MeV) in the electromagnetic calorimeter

This trigger doesn't apply any condition on the charge of the tracks in the CD. Therefore, in principle, it should be sensitive for charged and neutral decays of the η meson such as $\eta \rightarrow e^+e^-\gamma$ or $\eta \rightarrow \gamma\gamma$. The analysis of trigger effects and efficiency is of the uttermost importance for we need to compare our data to Monte Carlo simulations. During the offline analysis of the data sample, we have access to all trigger flags and can therefore choose only a subset of events with an active TR10 flag. There is no such possibility for Monte Carlo simulations.

Chapter 3

Event reconstruction

3.1 Energy Calibration

3.1.1 Forward Range Hodoscope energy calibration

We will discuss here the energy calibration of the FRH detector since the energy deposited in this detector is used to determine the kinetic energy of the passing through particles (mostly protons). All of those detectors are made of plastic scintillator. When a particle interacts inside a detector element (by excitation, ionization, etc.) light is emitted and collected by photo-multipliers. Therefore, the output signal is an electric pulse and, by integration, we calculate the collected charge Q . This value is approximately proportional to the energy E deposited by the particle in this detector element. In order to get the precise relation between Q and E a calibration must be performed.

The calibration correspond to the determination of the translation parameters and setting them on *calibration cards*.

Non-uniformity and non-linearity are two important effects that we have to take into account in the calibration process. They are treated separately and the corresponding procedure is presented in the next two subsections.

3.1.1.1 Non-uniformity calibration.

The efficiency of the light collection depends on the distance between the interaction region and the photo-multiplier. This distance, for each FRH layer, is related to the θ angle of the particle track. Moreover, the total energy deposited in one detector element

depends on the track length inside this element which is proportional to the inverse of $\cos\theta$, that is why we plot $Q\cos\theta$ versus θ on figure 3.1.

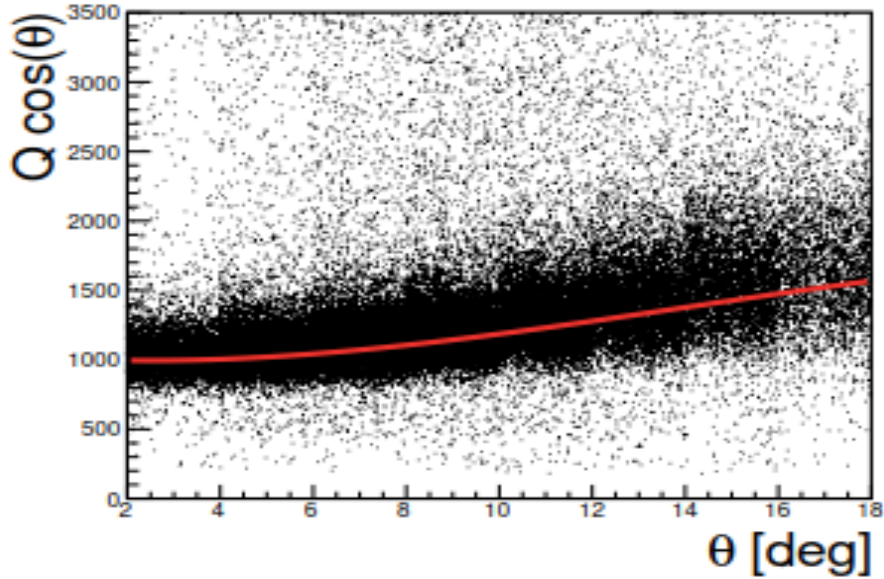


FIGURE 3.1: Illustration of non-uniformity in FRH

The non-uniformity effect is seen as a systematical shift of the average value as a function of scattering angle θ . By fitting a third-order polynomial we extract the corresponding four parameters.

This process is repeated for all layers and elements. For this purpose we use the following procedure:

- we process a few runs¹ with an special script to create a set of histograms such as in figure 3.1 - one histogram for each detector element
- the histograms are used as input for a fit to extract the non-uniformity correction parameters

3.1.1.2 Non-linearity calibration.

The relation between E and Q is not linear due to saturation and quenching effects. The plastic scintillators are not a perfectly homogenous medium neither the photomultipliers have an ideal linear response to the collected light.

¹We can, in principle, use any run but the most accurate is to take runs with an elastic trigger (TR2=frha1 or TR21=frha1&psc1) in order to select events with minimal ionizing particles (fast protons punching through all forward detectors). The reason is that the energy deposit of those particles is almost independent of their kinetic energy and is proportional to the length of their path inside the active detector material. This leads to a better separation of the non-uniformity and non-linearity effects.

We need to correct for those deviations. The fitting procedure consists on determining two parameters for non-linearity correction. We consider the following relation between E_{dep} and Q :

$$E_{dep} = Q \times C_0 \frac{1}{1 - Q \times \frac{C_1}{C_0}} \quad (3.1)$$

Those parameters need to be chosen such that the experimental data agrees with the Monte Carlo simulations after non-uniformity correction had been applied. We use two-dimensional histograms of energy deposits in two adjacent detector layers, for example ΔE_{FRH2} versus ΔE_{FRH1} (see figure 3.2).

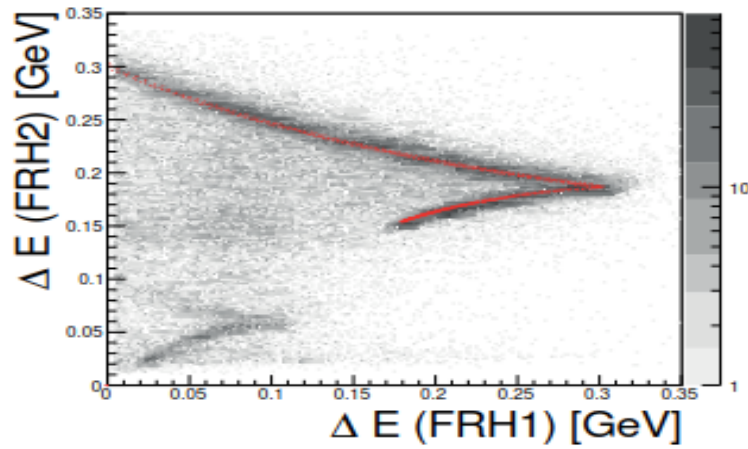


FIGURE 3.2: Energy deposits FRH2 vs FRH1

Setting the values of C_0 and C_1 for one detector layer (f.e. FRH2) influences two histograms ΔE_{FRH2} vs ΔE_{FRH1} and ΔE_{FRH3} vs ΔE_{FRH2} . We use a script that allows us to visualize simultaneously both plots along with three projections and we manually tune the parameters. A screenshot of the graphical interface of the script is shown in figure 3.3.

3.1.2 The energy calibration of the Central Detector.

We have seen in section 2.2.2 that The Central Detector is composed of three parts: the **Mini Drift Chamber** (MDC), the **Plastic Scintillator Barrel** (PSB) and the electromagnetic calorimeter (SE). The energy calibration of the CD is based on the photons originating from pion decays and on the reconstruction of those. The goal of the calibration procedure is that the invariant mass distribution of all cluster-cluster combinations will peak at the correct meson mass. The calibration is linear and it uses a pedestal run

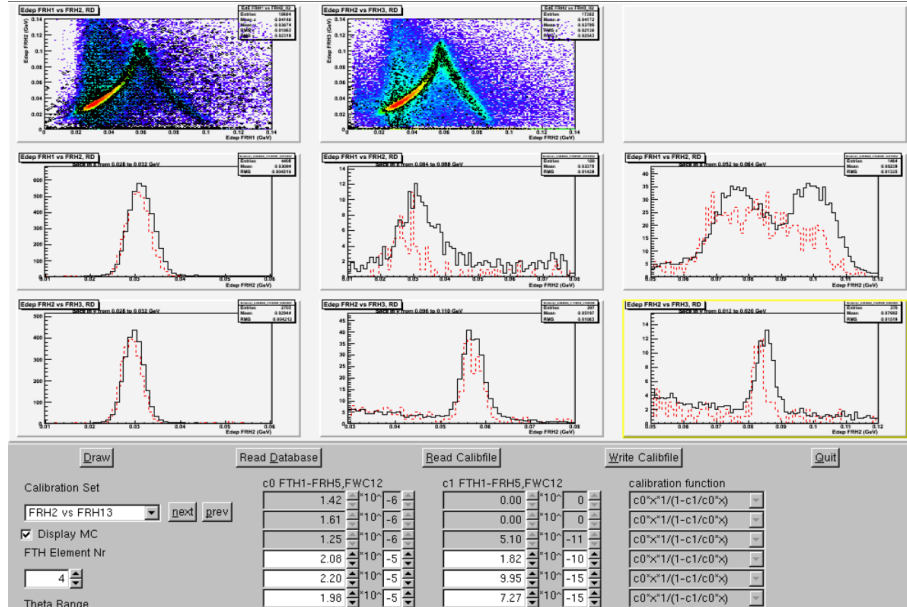


FIGURE 3.3: Non-linearity fitting graphical interface

(data is collected without any threshold on signals for different detector elements) and one constant for gain. A more detailed description is presented in [48].

Here, we focus on the verification of the calibration of the electromagnetic calorimeter. In order to check the calibration of the SE we look at the histogram of energy deposit in the SE versus the particle momentum multiplied by the sign of its charge. On such a plot, electrons and pions form characteristic bands due to the difference in their mass and stopping power. We expect those bands for data and Monte Carlo simulation to match.

First of all, we simulate two η decay channels, $\eta \rightarrow e^+e^-\gamma$ that contains only electrons in the final state and $\eta \rightarrow \pi^+\pi^-\gamma$ with pions in final state. Then, we fit the simulated electron and pion bands with a linear function (see figures 3.4a and 3.4b). Then we superimpose those lines on the corresponding histogram for data (see figure 3.5).

As we see on figure 3.5 while the matching between the electron bands and the fitted lines is rather satisfactory, for the pion bands it is not the case, as we observe some discrepancy. The reason of this offset will be investigated and corrected in further studies. A simple solution is to use a correction function but in case of our analysis, the pions are rejected anyway (see proper conditions in chapter 6).

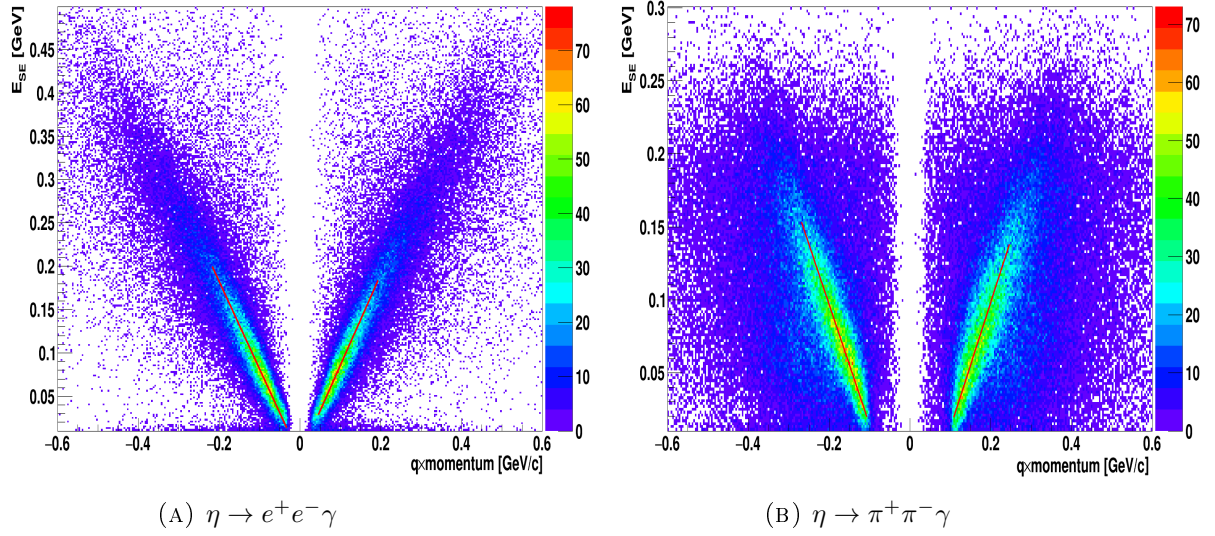
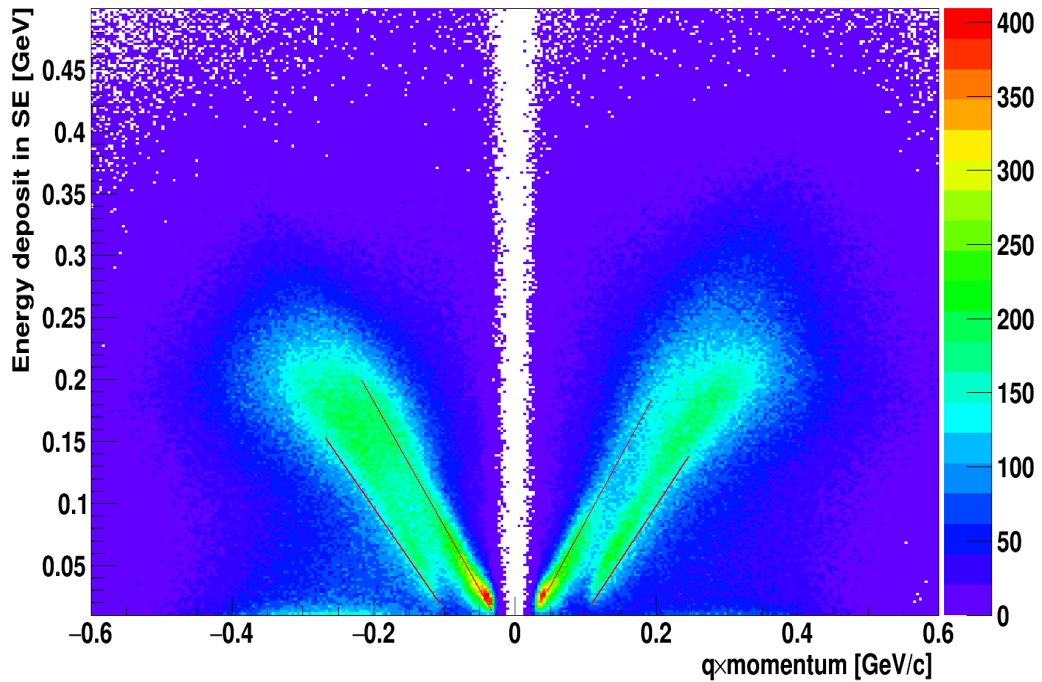
FIGURE 3.4: Energy deposit in calorimeter versus $q/e \times$ momentum.

FIGURE 3.5: Calorimeter calibration plot (lines are from fits to the simulated distributions).

3.2 Track reconstruction in MDC

The reconstruction of particle trajectories is crucial in the data analysis for it provides the four-momentum vectors that allow calculations of all other observables. As a general rule, hits from different detector elements are combined into clusters. The clusters are then merged into tracks. There are different algorithms depending on the considered detector part. The MDC track reconstruction provides the momenta and angles of charged tracks.

We group hits in MDC, using pattern recognition algorithms into tracklets and parametrize them as helices. At least 7 hits are needed to form a track. Then, we use a fitting routine that refine the parameters of each tracklet. We assume that the magnetic field is homogeneous in the whole MDC detector. This is not exactly true therefore a systematic uncertainty is introduced.

The helices are then extrapolated to the calorimeter and matched with its clusters.

Chapter 4

Monte Carlo simulations

4.1 Pluto simulation framework

Pluto is a simulation framework for heavy ions and hadronic physics based on ROOT environment (see reference [49]). It was initially developed by the HADES collaboration in GSI (see reference [50]). It adds a library of C++ classes providing an easy way to simulate different reactions in particle physics. The package includes models for resonance and Dalitz decays, resonance spectral functions with mass-dependent widths, and anisotropic angular distributions for selected channels. The generation of the homogeneous and isotropic phase space is based on the GENBOD routines (see reference [51]). For elementary reactions, PLUTO uses angular distribution models for selected channels based on the parametrization of existing data. The models used for simulations of reactions treated in this work will be mentioned in the next sections.

In addition to its large predefined set of classes and models, the PLUTO framework allows the user to include new angular distributions, redefine branching ratios, add new reactions or particles.

The output file of a PLUTO simulation has a ROOT format. It contains the four-vectors of all final state particles as well as vertices where the decays take place. The PLUTO simulation doesn't take into account any detector effects. Some of the simplest experimental limitations such as the geometrical acceptance can, in principle, be implemented by using the so-called filters. The output of a PLUTO simulation provides an input for the WASA Monte Carlo program that mimics the detector response (see section 4.2).

4.2 WASA Monte Carlo

The WASA Monte Carlo software is based on GEANT3 package developed in CERN (see references [52] and [53]). We use this program to determine our detector response to particles generated from PLUTO. Based on physical models, we obtain the signals from different detector elements.

4.3 Production of the η meson

In our experiment, the η meson is produced in p-p collisions at 1.4 GeV incident proton kinetic energy (corresponding to 2.14 GeV/c momentum). The threshold energy for η production in proton-proton collision is 1.256 GeV. Given the cross section for η production increases with energy it would seem natural to use the highest possible beam energy. However, we are limited by the forward detector geometry - forward scattered particles can only be detected if their θ angle is in $3^\circ - 18^\circ$ range¹. The other issue is that while the η production increases with energy so are the cross sections of most background reactions. We therefore set the beam kinetic energy to 1.4 GeV which is a compromise.

The η meson being, just next to the pion, the lightest non-strange particle. Its production mechanism was investigated and described by many authors, for $\pi^-p \rightarrow \eta p$ production channel see, for example, references [54], [55] or [56], for $pp \rightarrow pp\eta$ reaction refer to [57], [58] or [59]. The production mechanism of η in p-p collisions is dominated by the S_{11} or N^* resonance at 1535 MeV/c². This structure sits very close to the $\eta - N$ threshold, which means that the s-wave $\eta - N$ interaction is extremely strong and its effects manifest themselves in the final state interactions (FSI). This strong and attractive interaction might even lead to the formation of quasi-bound states of the η meson with a nucleus. This interesting possibility, beyond the scope of this work, is explored in the WASA-at-COSY experiment, see reference [60] for further details.

In figure 4.1 we show the $pp \rightarrow pp\eta$ and $pp \rightarrow pp\eta'$ production cross sections as a function of the excess energy $Q = \sqrt{s} - 2m_p - m_\eta$ where \sqrt{s} is the total center-of-mass energy. The increase of the total cross section with energy that is apparent in figure 4.1 is mostly related to the Q^2 dependence of the non-relativistic three-body space. However, if one modifies this with the one-pole approximation to the S-wave proton-proton final state interaction, the near-threshold energy dependence becomes:

¹We need protons in order to tag the η meson through the missing mass peak.

$$\sigma_T(pp \rightarrow pp\eta) = C \left(\frac{Q}{\varepsilon} \right)^2 / \left(1 + \sqrt{1 + Q/\varepsilon} \right)^2 \quad (4.1)$$

where C is constant and ε is the pole position (see Krusche and Wilkin [61]).

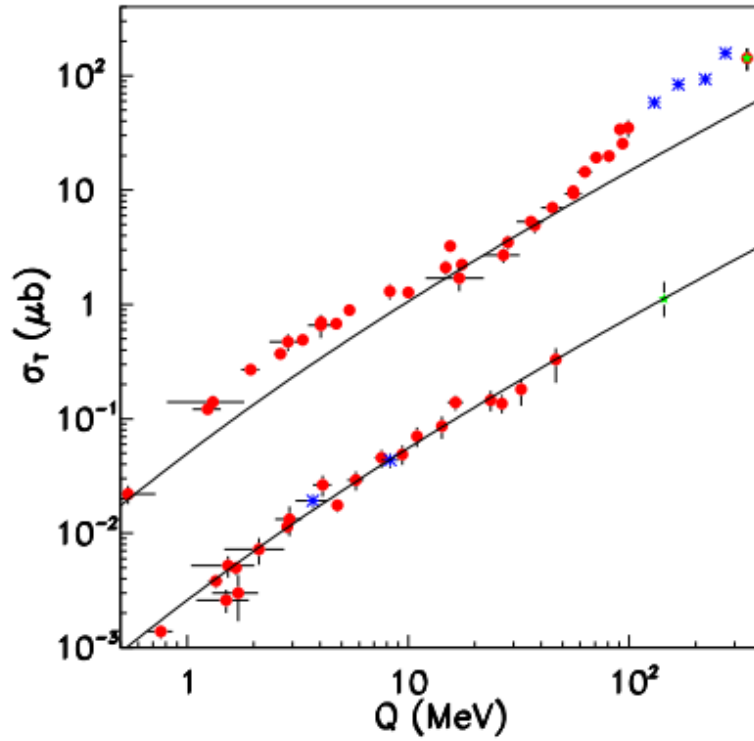
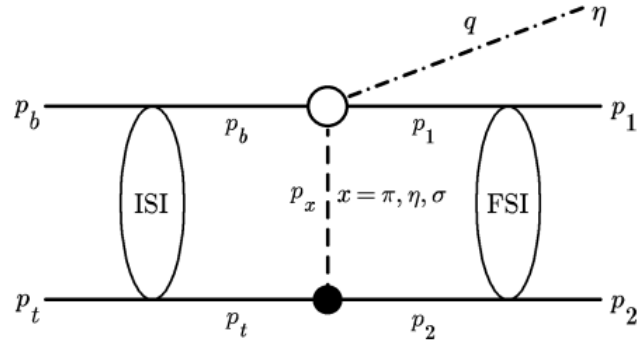
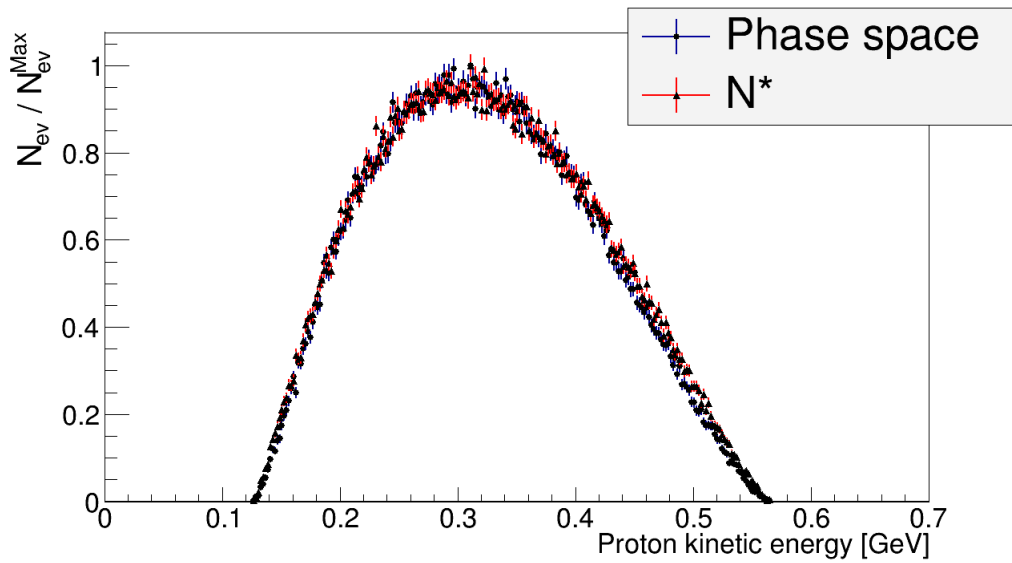


FIGURE 4.1: The cross section for $pp \rightarrow pp\eta$ (upper points) and $pp \rightarrow pp\eta'$ (lower points) production as a function of the excess energy Q . The solid curves are arbitrarily scaled pp FSI predictions of equation 4.1. Taken from Krusche and Wilkin [61]

The η production mechanism is represented by the Feynman diagram of figure 4.2. This picture assumes that this interaction proceeds through the emission of a meson $x(\pi, \eta, \rho, \dots)$ from one of the nucleons followed by a $xN \rightarrow \eta N$ transition. For a more detailed description of this process see reference [57].

Since the η meson production mechanism that we adopted in this work is based on pure phase space generation, we need to check if this choice could have an impact on further selection criteria. The figures 4.3, 4.4, 4.5 and 4.6 represent respectively the distributions of proton kinetic energy, proton θ angle, η meson θ angle and the angle between dilepton and photon (in laboratory frame of reference).

The differences between those distributions are sufficiently small to neglect their effect in our analysis.

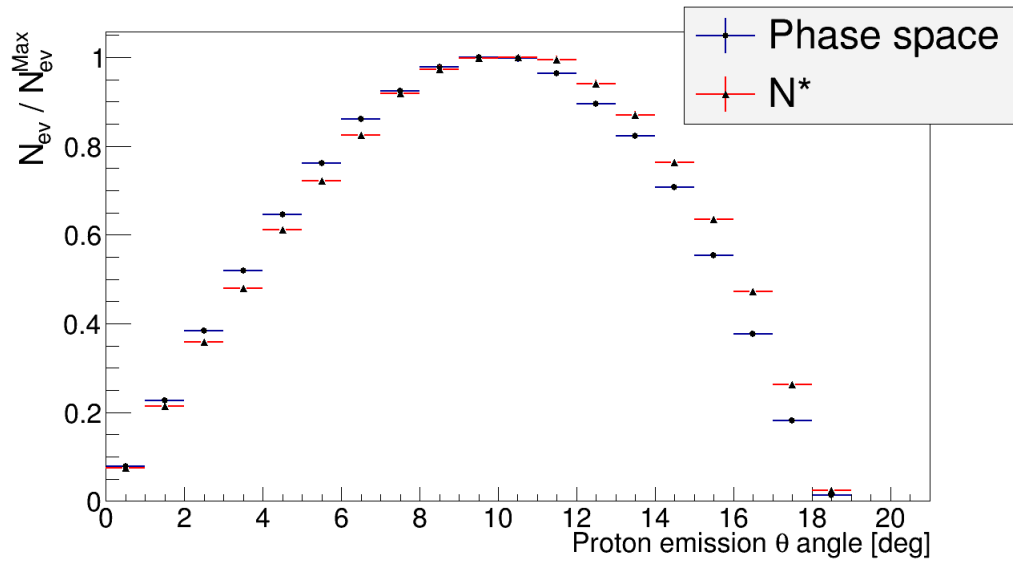
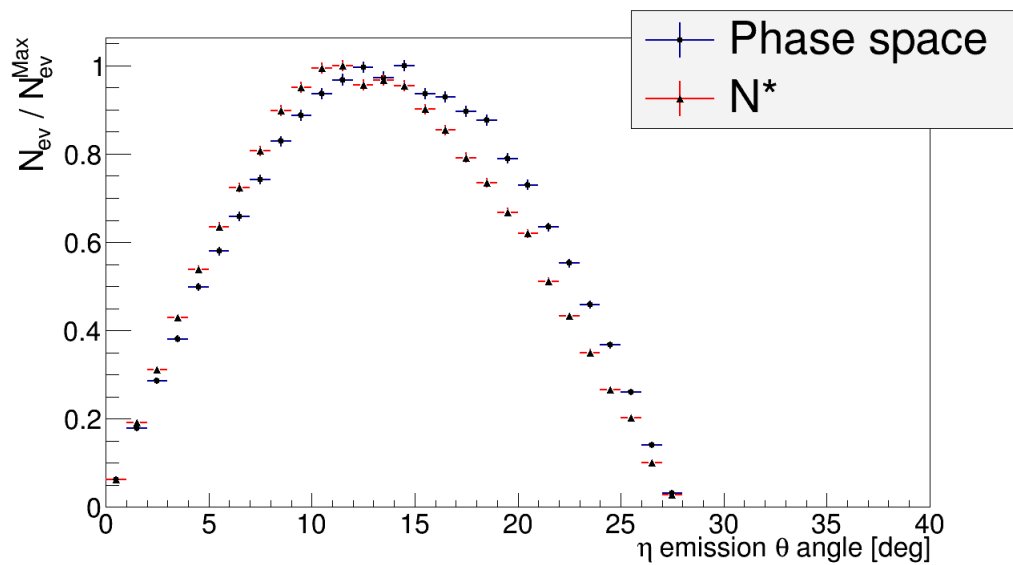
FIGURE 4.2: The mechanism of $pp \rightarrow pp\eta$ production (taken from [57]).FIGURE 4.3: Monte Carlo simulation (Pluto) for 10^6 events: proton kinetic energy.

4.4 The decays of η meson

4.4.1 The $\eta \rightarrow \gamma\gamma$ decay channel

This channel is important as a possible background since its branching ratio is 39.41%. There is a possibility that one of the photons interacts with the detector material (e.g. the beam pipe) creating an e^+e^- pair. The final state is the same as in Dalitz decay and the invariant mass of the three particles combines to the η meson mass thus it cannot be rejected easily. Nevertheless, we can use the fact that the leptonic pair is produced outside the interaction point, often at the beam pipe. This suppression of the external conversion is discussed in section 6.4.

The PLUTO model of this decay is an isotropic two body decay of a spin-less particle.

FIGURE 4.4: Monte Carlo simulation (Pluto) for 10^6 events: proton θ angle.FIGURE 4.5: Monte Carlo simulation (Pluto) for 10^6 events: θ angle of the η meson.

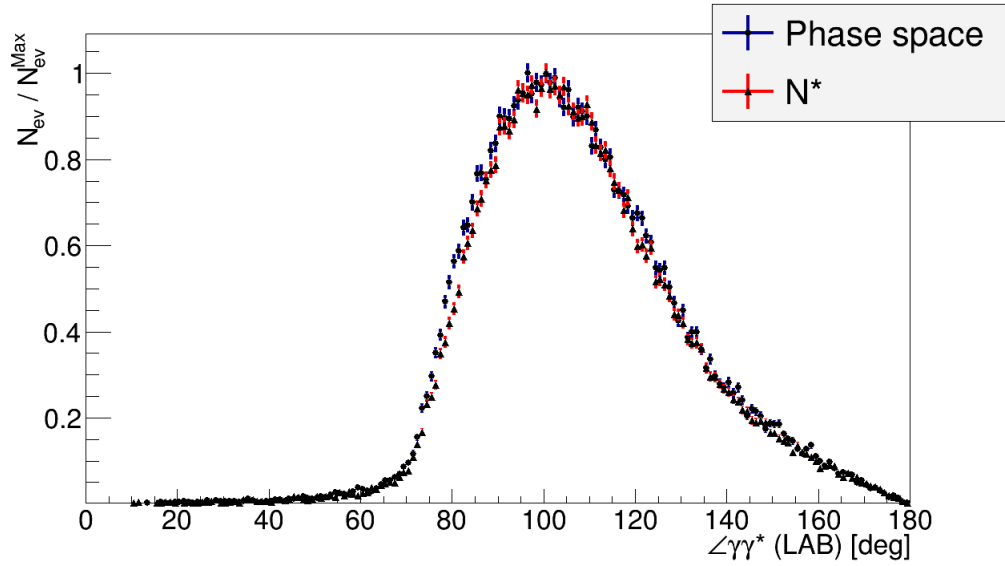


FIGURE 4.6: Monte Carlo simulation (Pluto) for 10^6 events: angle between dilepton and photon in the laboratory frame.

4.4.2 The $\eta \rightarrow e^+e^-\gamma$ decay channel

This reaction is our main channel in this analysis. We would like to extract $\eta \rightarrow e^+e^-\gamma$ event candidates from our data sample. On the one hand, it constitutes the principal background for the search of a light dark boson that decays into e^+e^- pair, on the other hand, a large sample of η meson Dalitz decay events allows the extraction of the transition form factor of the η meson (dividing the invariant mass of e^+e^- spectra from data by the spectra from pure QED simulation).

In order to select the η Dalitz decay channel and reduce other background contributions, we need to apply well chosen cuts on different variables such as angles, energies, invariant masses but also multiplicities of tracks etc. Therefore, we need to generate Monte Carlo simulations of those different channels and observe which distributions of variables allow us best to separate those contributions from $\eta \rightarrow e^+e^-\gamma$ decay.

The figure 4.7 shows the parameters used in PLUTO generation of the Dalitz processes. In addition to the virtual photon invariant mass $m_{\gamma^*} = m_{e^+e^-}$, its momentum $p_{\gamma^*}^{X_{RF}}$, the polar $\theta_{\gamma^*}^{X_{RF}}$ and the azimuthal $\phi_{\gamma^*}^{X_{RF}}$ emitting angles in the rest frame of the decaying particle (in our case η meson) there are two angles related to the photon decay into e^+e^- pair: the θ_e helicity angle and ϕ_e so called Treiman-Yang angle (see [49]).

Since the pseudoscalar mesons are spin-less, no alignment information is carried from the production mechanism to the decay, so $\theta_{\gamma^*}^{X_{RF}}$, $\phi_{\gamma^*}^{X_{RF}}$ and ϕ_e are isotropic. The helicity

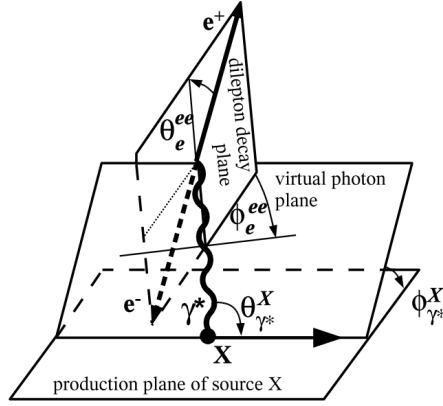


FIGURE 4.7: Geometrical variables involved in the description of a Dalitz process in PLUTO (taken from [49]).

angle distribution for pseudoscalar mesons is given by $(1 + \cos^2(\theta_e))$ (see reference [62]), which is included in PLUTO by default.

In order to describe the invariant mass distribution, PLUTO generates the Dalitz decays with a proper form factor. The latter can be set equal to unity in order to get a pure QED distribution. Both spectra are presented in figure 4.8.

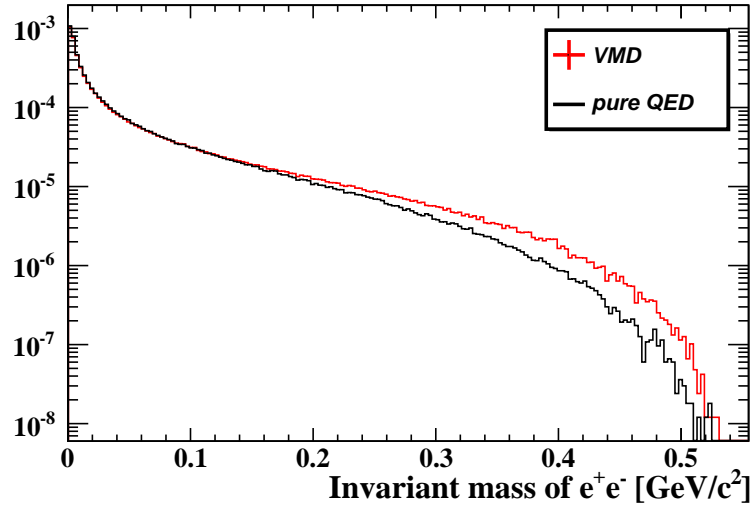


FIGURE 4.8: Effect of the transition form factor on the invariant mass of e^+e^- spectra.

Figure 4.8 represents the simulated invariant mass of e^+e^- for a pure QED (transition form factor equals unity) and a more realistic simulation where the form factor is computed assuming the VMD (**V**ector **M**eson **D**ominance) model.

4.4.3 The $\eta \rightarrow \pi^+\pi^-\pi^0$ decay channel

The branching ratio of this η decay channel is 22.92%. The probability for this channel to mimic the Dalitz decay is rather low due to the fact that it would need the simultaneous misidentification of two pions and the loss of one of the photons from $\pi^0 \rightarrow \gamma\gamma$ decay.

PLUTO simulation of this channel is based on the fact that the plane of the η decay shows a strong non-phase space behavior, which is caused by the difference of the light quark masses (see reference [63] for details). The parameterization of the matrix element (i.e. the deviation from the constant value of the Dalitz plot) used in PLUTO is based on the measurement performed by the Crystal Barrel collaboration (see reference [64]).

4.4.4 The $\eta \rightarrow \pi^0\pi^0\pi^0$ decay channel

Although this is a very common decay of the η meson with branching ratio equal to 32.7% its final state contains mostly photons from $\pi^0 \rightarrow \gamma\gamma$ decays and therefore it can be efficiently rejected during the selection process.

4.4.5 The $\eta \rightarrow \pi^+\pi^-\gamma$ decay channel

This decay has a branching ratio of 4.2%. The final state contains two charged tracks and one neutral particle, same as in the Dalitz decay.

For this decay, PLUTO uses the simplest gauge invariant matrix element including p-wave interactions of the pions according to $|M^2| = k^2q^2\sin^2\theta$, where k is the photon momentum in the rest frame of the η meson, q and θ are defined as the momentum of either pion and the angle between π^+ and γ , both in the rest frame of the two pions.

4.5 Direct production of π mesons

4.5.1 The $pp \rightarrow pp\pi^+\pi^-$ reaction channel

In this reaction no photons are produced. Nevertheless, this channel can be an issue because it has a high cross section and if a neutral track is mistakenly added to the event the final state would have the same topology as the η Dalitz decay. An additional neutral track photon could originate from another event (pile-up effect) or from a misinterpretation of an electromagnetic cascade split-off.

4.5.2 The $pp \rightarrow pp\pi^0\pi^0$ reaction channel

This is an important channel for its cross section is high with respect to the η meson production. We have to consider the case where one pion decays into two photons and the other one through Dalitz decay. The process of direct two pion production mostly occurs via a two-Delta resonance state, therefore we will use this mode of production in our simulations.

4.5.3 The $pp \rightarrow pp\pi^+\pi^-\pi^0$ reaction channel

If one of the photons from the decay of the neutral pion is lost, we have the same problem as in the previous section. We use the contribution from this reaction to the missing mass of two protons in our fitting procedure (see section 6.9) to reject the non- η background (see figure 4.9).

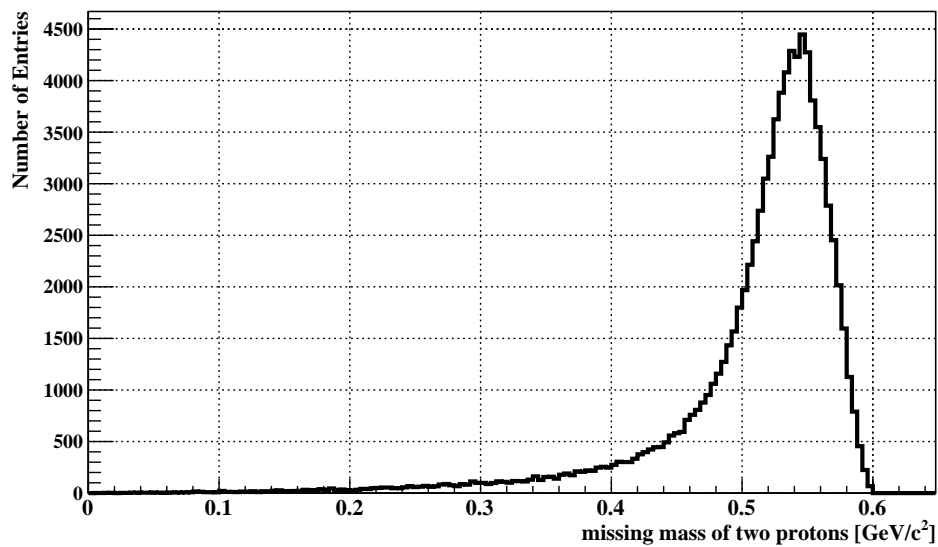


FIGURE 4.9: Missing mass of two protons for $pp \rightarrow pp\pi^+\pi^-\pi^0$.

Chapter 5

Data set

5.1 Initial data sample reduction.

Our analysis is based on data taken during the beam-time period that lasted from February 2012 until April 2012 (effectively around 6-7 weeks). In the experiment, collisions between a proton beam with kinetic energy of 1.4 GeV and frozen hydrogen pellets were used. At this energy the η meson production channel $pp \rightarrow pp\eta$ is open.

The total amount of data collected during this period is around 115 TB. Even after an initial rejection of non relevant data, for example due to other triggers or detector adjustment periods, we have to deal with 70 TB of stored data files.

Therefore, we need to further reduce this amount of data keeping only events that fulfill some basic criteria. A RootSorter-based program called PPSEL was written that selects a certain class of events and saves them for further processing.

Our analysis focuses on charged decays of the η meson such as $\eta \rightarrow e^+e^-\gamma$ or $\eta \rightarrow e^+e^-$ therefore we look for events with at least two charged tracks in the central detector. Additionally, we also wanted to have access to the dominant neutral modes of decays of η such as $\eta \rightarrow \gamma\gamma$ and $\eta \rightarrow \pi^+\pi^-\pi^0$ for normalization and background studies. This two classes of events were stored separately.

A common condition for both classes is that each event contains at least two proton-like tracks in the forward detector. This criterion allows us to calculate the missing mass for those two particles (see figure 5.1). For the reaction $pp \rightarrow pp\eta$ we should be able to observe a peak at the η meson mass. The Forward Detector is thus used like a trigger to tag the events with η meson production.

The table 5.1 shows the effect of selection criteria applied to the data sample for a typical data file. All those cuts are applied for both charged and neutral η decay classes. The common selection steps are the following:

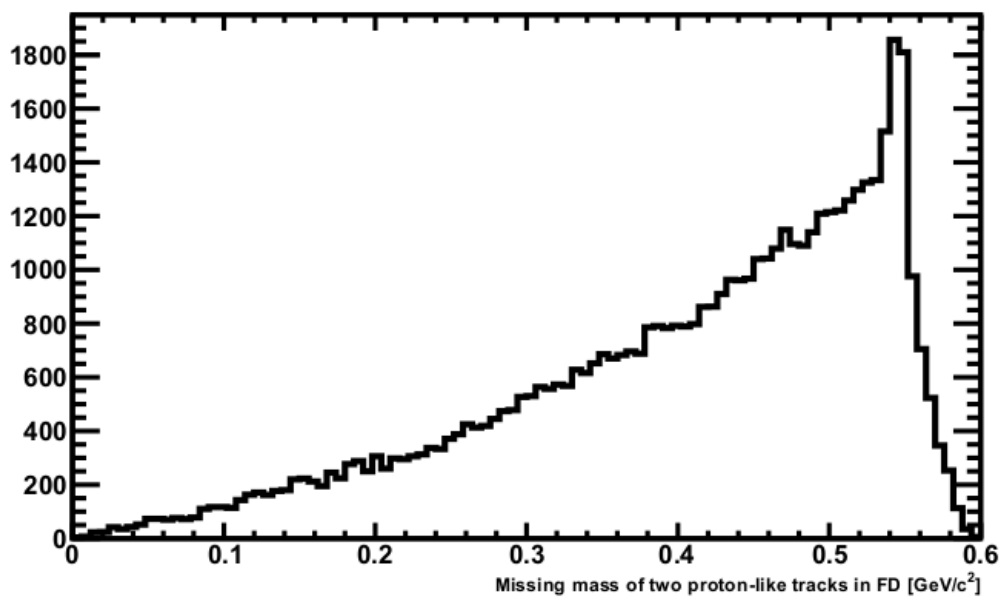


FIGURE 5.1: Missing mass of two proton-like tracks in the Forward Detector.

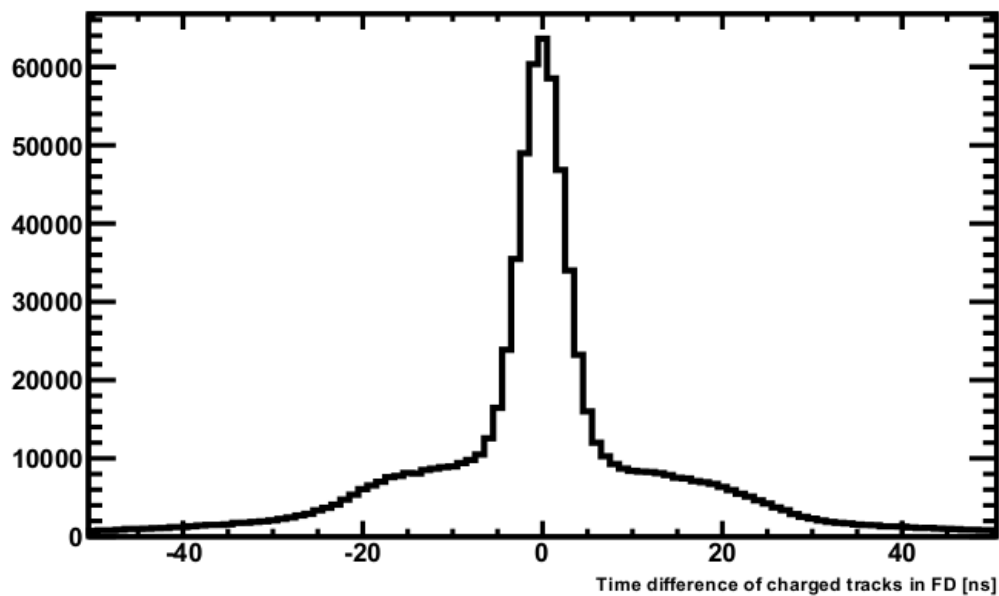


FIGURE 5.2: Time difference in ns between charged tracks in the Forward Detector.

TABLE 5.1: Effect of the selection conditions

Condition	Number of events
All events	$4 \cdot 10^6$
Trigger	$5.57 \cdot 10^5$ (13.9%)
≥ 2 FD ch.tr. ≥ 10 MeV	$4.94 \cdot 10^5$ (12.35%)
≥ 1 pair FD ch.tr. inside 10 ns time window	$4 \cdot 10^5$ (10%)
proton identification	$2.76 \cdot 10^5$ (6.9%)

- the trigger system must have been activated, which happens when there are at least two tracks of matching clusters in the Forward Detector and at least two clusters in the Central Detector above threshold
- at least two charged tracks in the Forward Detector with energy deposit above 10 MeV
- at least two charged tracks in the Forward Detector inside 10 ns time window (see figure 5.2)
- two proton-like tracks in the Forward Detector (particle identification in FD)

After this primary selection process, the data sample is divided into two streams that are saved for further analysis. The stream with charged decays of η meson is selected by the following set of conditions:

- at least 14 hits in the Mini Drift Chamber - the event reconstruction program needs at least 7 hits in MDC in order to build a charged track and we want two reconstructed charged tracks
- at least two hits in the Plastic Scintillator - only charged particles should provide a signal in the PS detector

The events with neutral decays are chosen by requiring:

- no hits in the Plastic Scintillator
- at least two neutral tracks reconstructed in the Central Detector with energy deposit above 10 MeV

The table 5.2 shows the number (absolute and relative) of events that remain after all selection conditions for both classes.

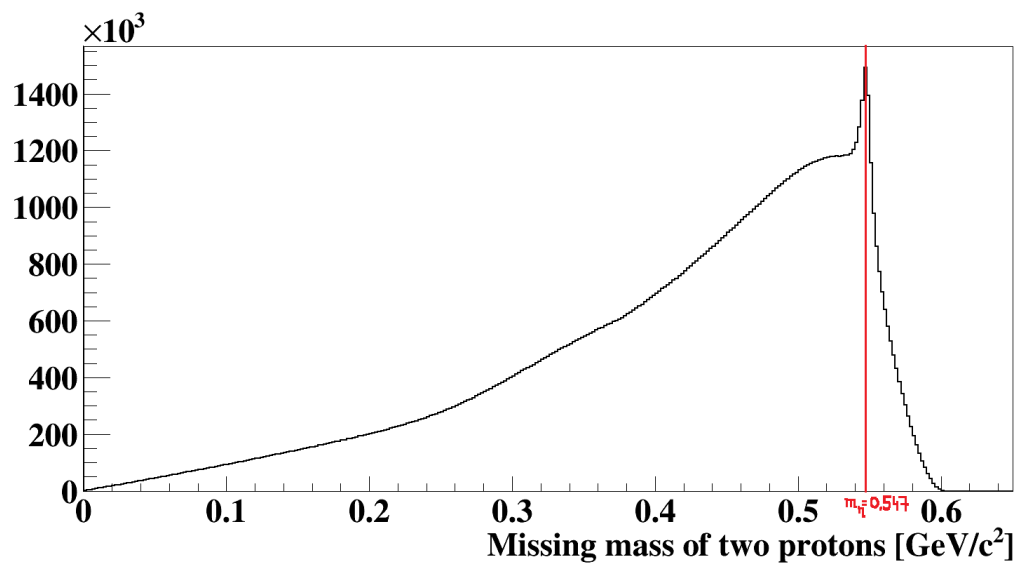
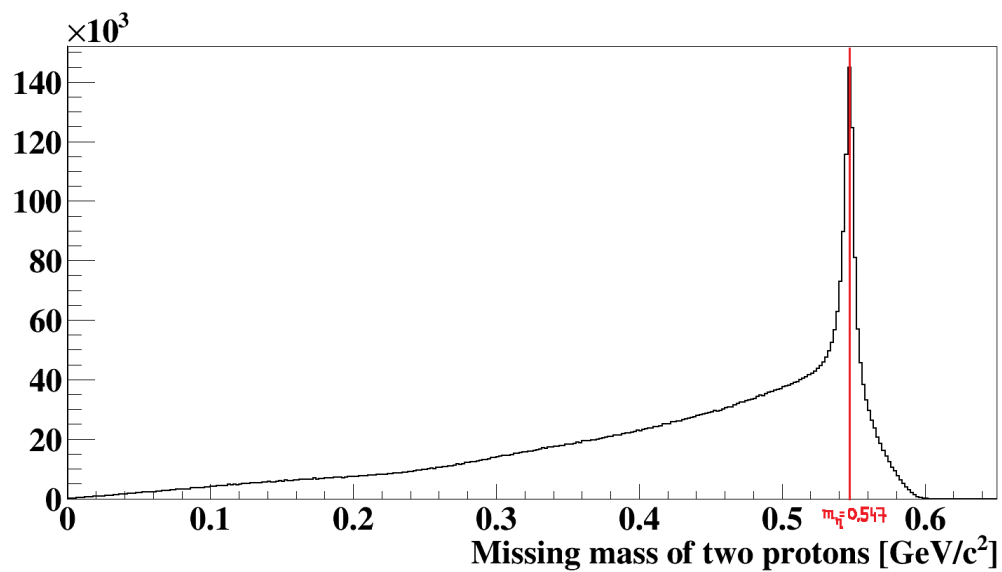
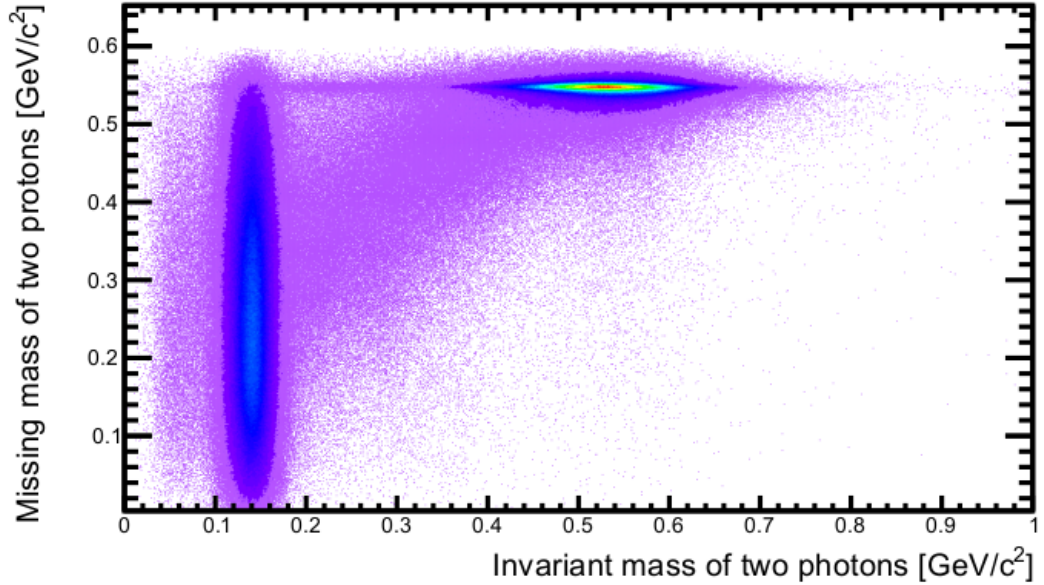
FIGURE 5.3: The missing mass of two protons for the selection of charged decays of η .FIGURE 5.4: The missing mass of two protons for the selection of neutral decays of η .

TABLE 5.2: Events in the final sample

Condition	Number of events
All events	$4 \cdot 10^6$
Events from charged decays	$1.4 \cdot 10^5$ (3.6%)
Events from neutral decays	$6.9 \cdot 10^4$ (1.7%)

FIGURE 5.5: The missing mass of two protons versus the invariant mass of two photons for the selection of neutral decays of η .

The selection performed by the PPSEL program reduced the size of the data sample suitable for our analysis to around 2.7 TB thus a reduction factor of 26 was achieved.

Figures 5.3 and 5.4 show the missing mass of two protons respectively for the events from the charged and the neutral stream. Figure 5.5 shows the missing mass of two protons versus the invariant mass of two photons for the neutral selection.

5.2 Normalization with $\eta \rightarrow \gamma\gamma$ channel

The $\eta \rightarrow \gamma\gamma$ channel can be extracted from the neutral decays selection in order to estimate the number of η meson produced. The selection process starts with the condition used in the initial selection of the neutral decays - the requirement of at least two reconstructed neutral tracks in CD with deposited energy above 10 MeV and a veto on PS

signal. This is redundant for preselected data events but necessary for comparison with Monte Carlo simulations. The selection of the $\eta \rightarrow \gamma\gamma$ channel constrains the processed events with the following conditions:

- at least two neutral tracks such as $-25 \text{ ns} < |t_N - \bar{t}_P| < 5 \text{ ns}$, where t_N is the time of the neutral signal (CD) and \bar{t}_P is the mean proton time (FD)
- in case there are more than two neutral tracks, we choose the pair with the largest mutual angle calculated in η rest frame¹ $\Omega_{\eta RF}^{\gamma_1 \gamma_2}$
- we require $\Omega_{\eta RF}^{\gamma_1 \gamma_2} > 140^\circ$
- time difference between neutrals $< 10 \text{ ns}$
- the energy deposit of each neutral track must be above 100 MeV
- the missing mass of two protons is in the range 530 – 570 MeV/c²

The invariant mass of $\gamma\gamma$ for data events that pass through this selection process is represented on figure 5.6 (black squares).

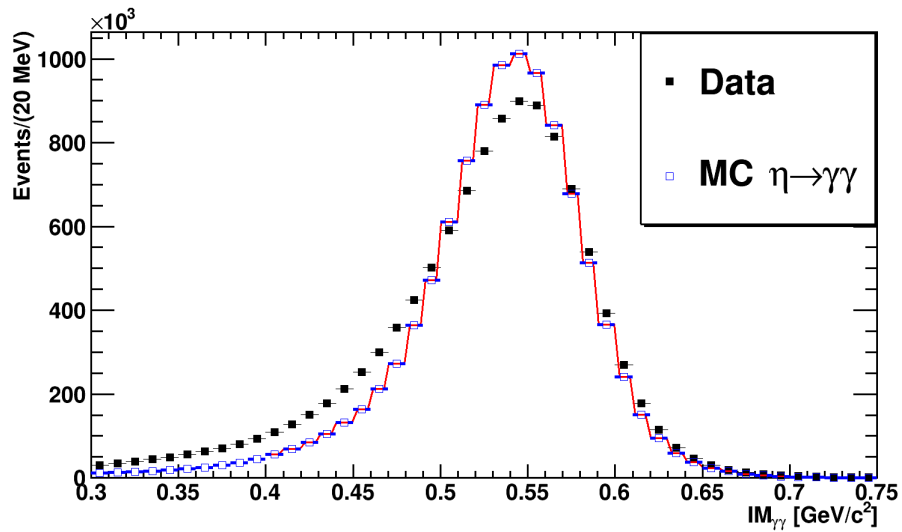


FIGURE 5.6: The invariant mass of $\gamma\gamma$: data and $\eta \rightarrow \gamma\gamma$ Monte Carlo simulation (WMC).

The number of η mesons can be estimated using the $\eta \rightarrow \gamma\gamma$ channel with the formula:

¹The η four vector is obtained by subtracting two protons four vectors from the initial beam and target four vector.

$$N_\eta = \frac{N_{\gamma\gamma}}{BR_{\gamma\gamma} \cdot A_{\gamma\gamma}} \quad (5.1)$$

where $N_{\gamma\gamma}$ is the number of $\eta \rightarrow \gamma\gamma$ events, $BR_{\gamma\gamma}$ is the branching ratio for this channel and $A_{\gamma\gamma}$ its acceptance that takes into account the effect of the detector geometry, losses from the reconstruction procedure and the reduction due to the selection criteria.

If we assume that only $\eta \rightarrow \gamma\gamma$ channel remains in data after our selection, we can estimate the number of η mesons from formula 5.1 by fitting the data with a Monte Carlo simulation of $\eta \rightarrow \gamma\gamma$ (after simulating also the WASA detector response with WMC). This is shown on figure 5.6. The number of $\eta \rightarrow \gamma\gamma$ events extracted is $\sim 10.5 \cdot 10^6$. The branching ratio for $\eta \rightarrow \gamma\gamma$ is 39.41% and the mass integrated acceptance (for our selection process) is $14.5 \pm 1.3\%$ thus the number of η meson equals $\sim 183.8 \cdot 10^6$. This value is overestimated - the fit quality is very poor for we have neglected all possible background sources.

In order to correct the number of $\eta \rightarrow \gamma\gamma$ event candidates and consequently the number of produced η mesons we fit the selected data with the sum of Monte Carlo simulations that passed through the same selection process $\eta \rightarrow \gamma\gamma$, $pp \rightarrow pp\pi^0(\rightarrow\gamma\gamma)\pi^0(\rightarrow\gamma\gamma)^2$ and a polynomial of degree N . The double pion production cross section in proton-proton collisions is $324 \pm 21_{systematic} \pm 58_{normalization} \mu b$ (see reference [65]) compared to η meson production cross section $10 \mu b$. The acceptance for $pp \rightarrow pp\pi^0(\rightarrow\gamma\gamma)\pi^0(\rightarrow\gamma\gamma)$ channel is $0.025 \pm 0.0016\%$. The fit is based on the following bin per bin decomposition of the data histogram:

$$\begin{aligned} N_{data}(x) &= N_\eta \left(BR_{\eta \rightarrow \gamma\gamma} \cdot A_{\eta \rightarrow \gamma\gamma}(x) + \frac{\sigma(pp \rightarrow pp\pi^0\pi^0)}{\sigma(pp \rightarrow pp\eta)} \cdot A_{2\pi^0}(x) \right) + PolyN \\ &= p_0 (X_{\eta \rightarrow \gamma\gamma}(x) + X_{2\pi^0}(x)) + \sum_{i=0}^N p_i x^i \end{aligned} \quad (5.2)$$

where x represents bins in the invariant mass of $\gamma\gamma$ and the acceptances $A_*(x) = \frac{N_{fin}(x)}{N_{ini}(x)}$ are the ratio (for each bin) between the invariant mass histogram after and before selection cuts. For this decomposition, the parameter p_0 represents the number of η mesons N_η .

In order to approximate the real value for the number of η mesons, we repeat the fitting procedure while varying three external parameters: the binning of the fitted histogram,

²BR($\pi^0 \rightarrow \gamma\gamma$) ~ 0.98 .

the fit range and the degree of the added polynomial. Figure 5.7 represents the resulting fits for 20 MeV/c² bin width, 350 – 700 MeV/c² fit range and a third order polynomial.

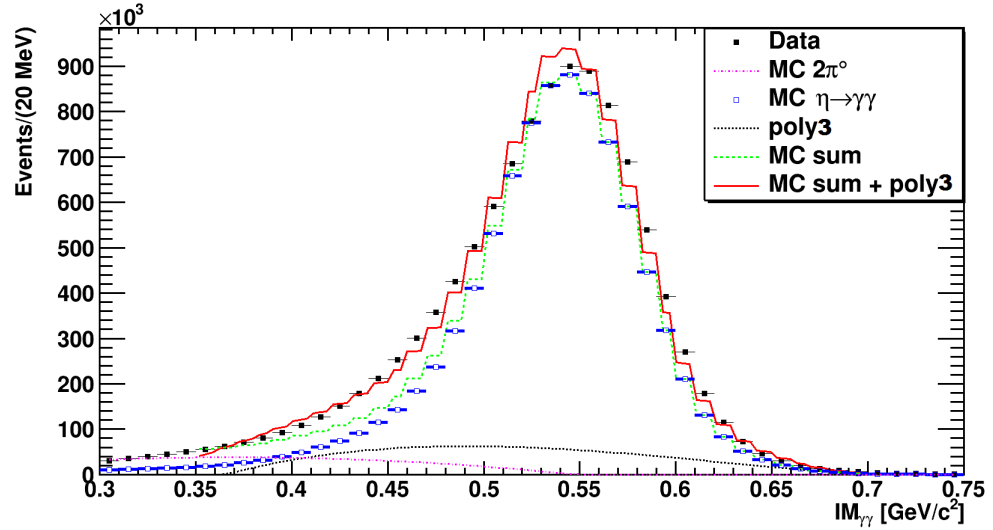


FIGURE 5.7: The invariant mass of $\gamma\gamma$: data and simulations.

The figures 5.8 illustrate fits when the bin width is changed while the range is set to 400 – 700 MeV/c² and we add a third order polynomial to the simulations.

The figures 5.9 illustrate fits when the fit range is varied while the bin width is set to 20 MeV/c² and we add a third order polynomial to the simulations.

The tables 5.3, 5.4 and 5.5 contain the number of η meson ($/10^6$) extracted from fits performed with the addition of respectively second order, third order polynomial, and no polynomial at all.

TABLE 5.3: Number of η mesons ($/10^6$) extracted from fits with second order polynomial

Bin width \ Range	10 MeV/c ²	20 MeV/c ²	40 MeV/c ²
300 – 700 MeV/c ²	148.68	149.24	148.60
350 – 700 MeV/c ²	147.05	147.31	146.36
400 – 700 MeV/c ²	147.54	147.80	146.85

TABLE 5.4: Number of η mesons ($/10^6$) extracted from fits with third order polynomial

Bin width \ Range	10 MeV/c ²	20 MeV/c ²	40 MeV/c ²
300 – 700 MeV/c ²	149.08	149.49	148.67
350 – 700 MeV/c ²	145.04	145.44	145.87
400 – 700 MeV/c ²	137.66	138.00	137.58

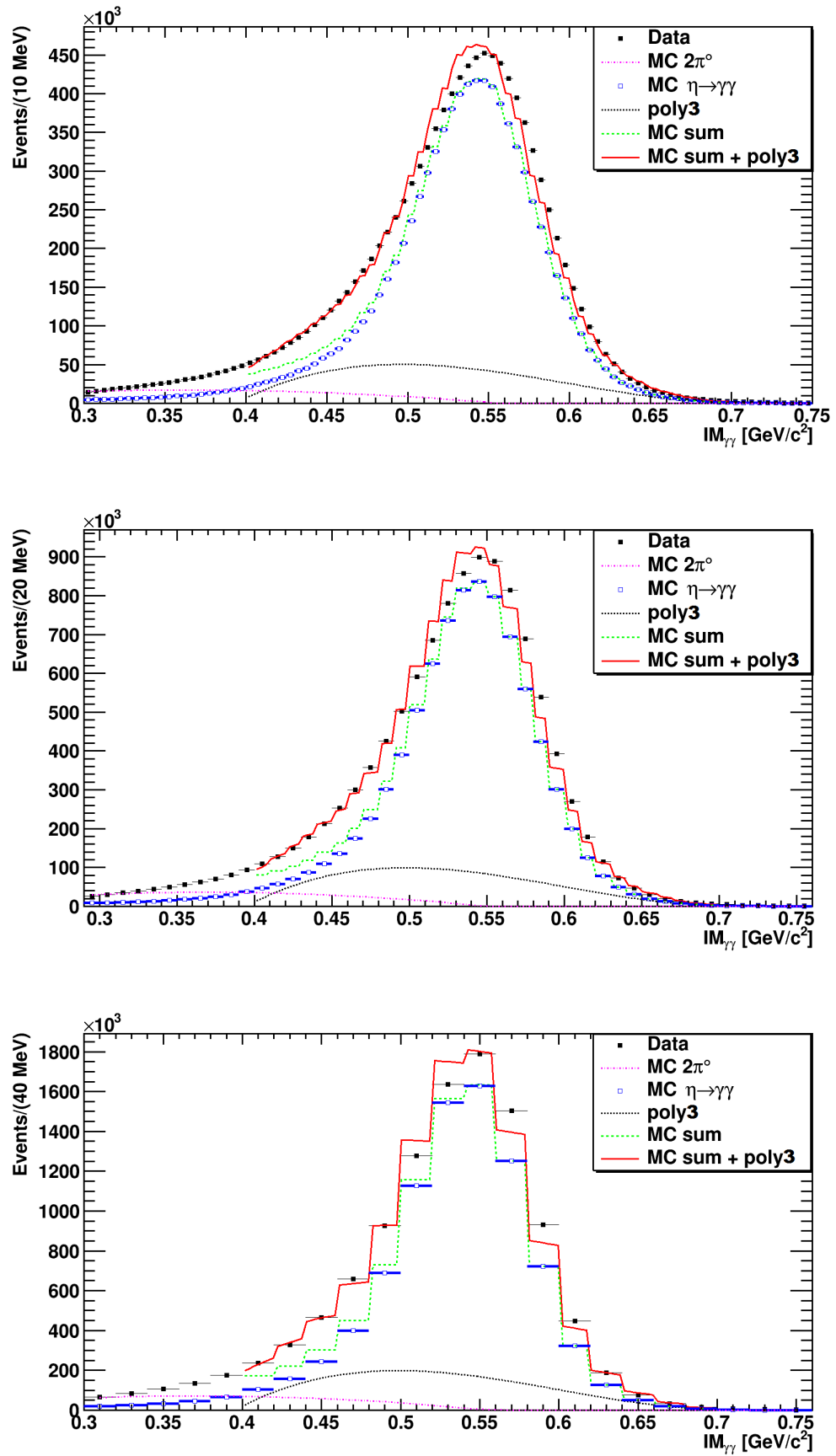


FIGURE 5.8: The invariant mass of $\gamma\gamma$: fit with different binning $10 \text{ MeV}/c^2$, $20 \text{ MeV}/c^2$ and $40 \text{ MeV}/c^2$.

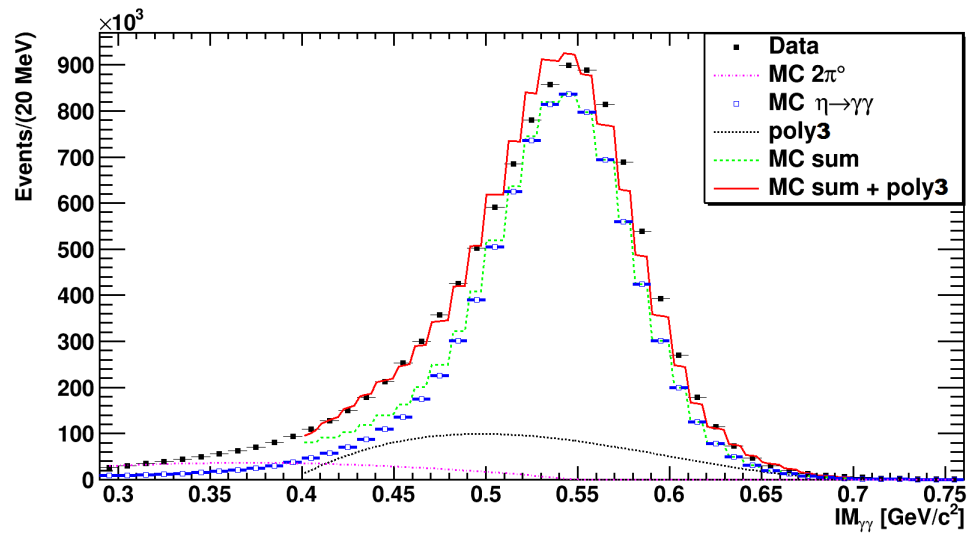
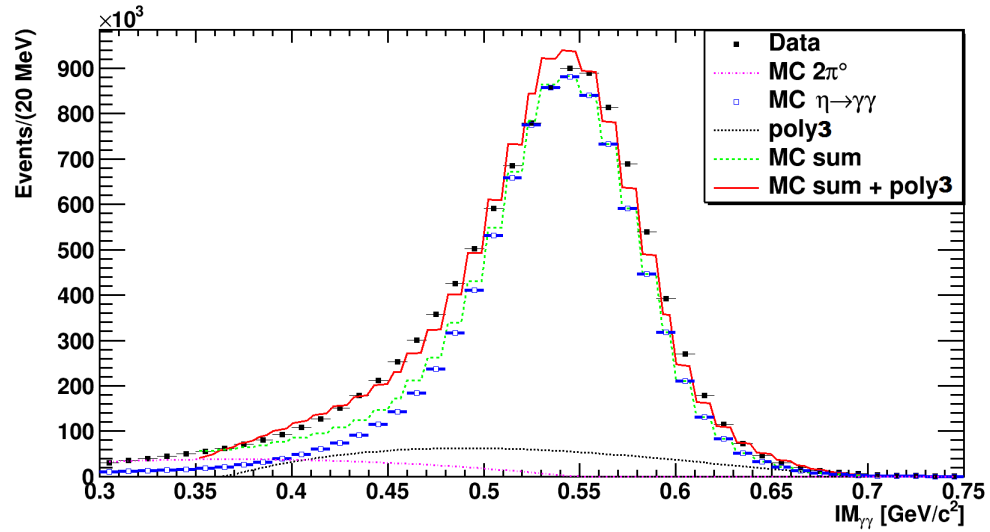
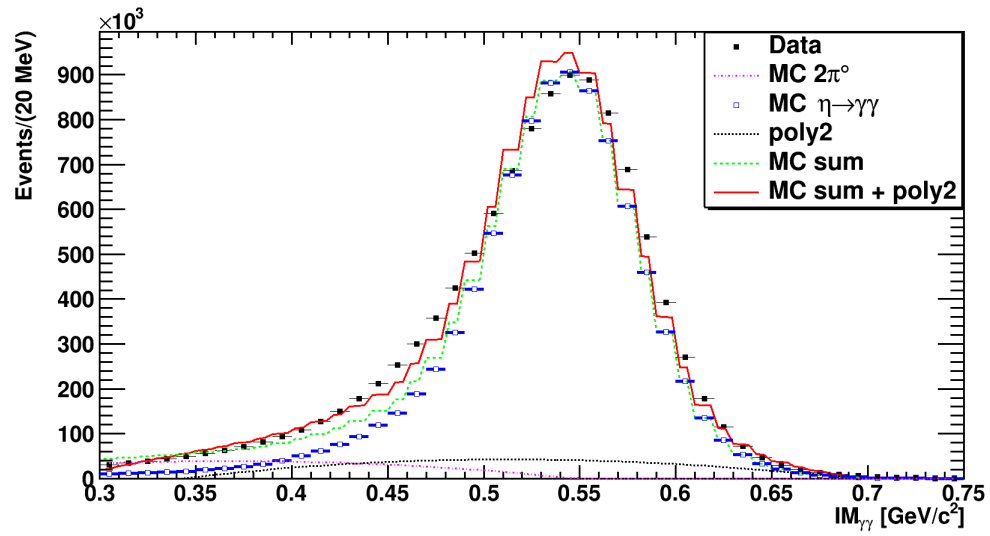


FIGURE 5.9: The invariant mass of $\gamma\gamma$: fit with different fit range 300 – 700 MeV/c², 350 – 700 MeV/c² and 400 – 700 MeV/c².

TABLE 5.5: Number of η mesons ($/10^6$) extracted from fits without additional polynomial

Bin width Range	10 MeV/c ²	20 MeV/c ²	40 MeV/c ²
300 – 700 MeV/c ²	162.20	161.86	161.80
350 – 700 MeV/c ²	163.57	163.40	163.01
400 – 700 MeV/c ²	163.47	163.49	163.22

Given the table 5.5 neglects any source of accidental background we use only tables 5.3 and 5.4 to extract a mean value and the standard deviation (as a systematic effect):

$$\overline{N}_\eta = (145.90 \pm 0.08_{stat} \pm 3.97_{sys}) \cdot 10^6$$

Another source of systematic uncertainties on the number of η mesons are the selection criteria used in our analysis of the $\eta \rightarrow \gamma\gamma$ channel. To take those into account we repeated the analysis with slight modifications of temporal (time between the two photons), angular (angle between the two photons in η meson rest frame) and missing mass (of two protons) conditions. The fit was done with a fixed bin width of 20 MeV/c², in a fixed 350 – 700 MeV/c² range and with the addition of a third order polynomial. The results are shown in table 5.6

TABLE 5.6: Number of η mesons ($/10^6$) extracted from fits without additional polynomial

Condition	$N_\eta/10^6$	$\eta \rightarrow \gamma\gamma$ % in data
$ t_{\gamma_1} - t_{\gamma_2} < 12 \text{ ns}$	142.14	82.84%
$ t_{\gamma_1} - t_{\gamma_2} < 8 \text{ ns}$	151.71	83.17%
$\angle_{\eta_{RF}}^{\gamma_1\gamma_2} > 130^\circ$	142.81	85.60%
$\angle_{\eta_{RF}}^{\gamma_1\gamma_2} > 150^\circ$	148.90	78.78%
$525 \text{ MeV}/c^2 < MM2P < 575 \text{ MeV}/c^2$	141.66	81.77%
$535 \text{ MeV}/c^2 < MM2P < 565 \text{ MeV}/c^2$	147.83	83.66%

We observe that for stricter conditions, rather unexpectedly, we extract more η mesons using the described fitting procedure. This is due to the fact that the acceptance for $\eta \rightarrow \gamma\gamma$ channel is reduced while the relative content of this decay increases.

Again, we extract the mean value and the uncertainties of those fits:

$$\overline{N}_\eta = (145.84 \pm 0.07_{stat} \pm 4.20_{sys}) \cdot 10^6$$

We see that the two mean values are consistent with each other. We therefore merge all fit results and got the final number of η mesons:

$$\overline{N}_\eta = (145.89 \pm 0.08_{stat} \pm 3.93_{sys}) \cdot 10^6$$

5.3 Analysis of the main trigger.

In section 5.1 we have mentioned that in order to reduce the size of the data we use some preliminary criteria. Already during the stage of data acquisition we use a set of hardware triggers. For an event to be saved it has to activate at least one such trigger. During the offline analysis, we have access to the list of all triggers and we can see which triggers were activated by this event. An example of such a list, showing the set-up for a series of runs, is presented in figure 5.10.

```

0          fhdwr2 [ ] PS(1, 0) 1000000 |1,0) -> 21,
1          fhdwr2|Vps1 [ ] PS(1, 1) 1000000 |1,1) -> 21,28,
2          frha1 [x] PS(1, 2) 9000 |1,2) -> 24,
3          fhdwr2|frhb2|seln2|Vps1 [ ] PS(1, 3) 1000000 |1,3) -> 19,21,28,41,
4          fhdwr2|frhb2 [ ] PS(1, 4) 1000000 |1,4) -> 19,21,
5          fhdwr2|seln2 [x] PS(1, 5) 100 |1,5) -> 21,41,
6          fhdwr2|seln3 [ ] PS(1, 6) 1000000 |1,6) -> 21,29,
7          fhdwr2|frhb2 [ ] PS(1, 7) 1000000 |1,7) -> 19,21,
8          fhdwr2|frhb2|Vps1 [ ] PS(1, 8) 1000000 |2,0) -> 19,21,28,
9          frha2 [x] PS(1, 9) 1600 |2,1) -> 25,
10         fhdwr2|frhb2|seh2 [x] PS(1,10) 1 |2,2) -> 14,19,21,
11         fhdwr2|frhb2|ps2 [ ] PS(1,11) 1000000 |2,3) -> 19,21,33,
12         fhdwr1 [ ] PS(2, 0) 1000000 |2,4) -> 20,
13         fhdwr2|frhb2|ps2|sel2 [ ] PS(2, 1) 1000000 |2,5) -> 16,19,21,33,
14         lpp [x] PS(2, 2) 1 |2,6) -> 30,
15         lpc [x] PS(2, 3) 1 |2,7) -> 27,
16         fhdwr2|frhb2|seln2 [ ] PS(2, 4) 1000000 |3,0) -> 19,21,41,
17         psf1|pscl [x] PS(2, 5) 3000 |3,1) -> 4,6,
18         fhdwr2|seln2|Vps1 [ ] PS(2, 6) 1000000 |3,2) -> 21,28,41,
19         fhdwr2|seln3|Vps1 [ ] PS(2, 7) 1000000 |3,3) -> 21,28,29,
20         fhdwr2|frhb2|ps2|selc1 [ ] PS(2, 8) 1000000 |3,4) -> 19,21,33,42,
21         frha1|pscl [x] PS(2, 9) 5000 |3,5) -> 6,24,
22         fhdwr2|seln2|Vps1 [ ] PS(2,10) 1000000 |3,6) -> 21,28,41,
23         fhdwr2|seln3|Vps1 [ ] PS(2,11) 1000000 |3,7) -> 21,28,29,
24         fhdwr2|frhb2|sehn2 [ ] PS(3, 0) 1000000 |4,0) -> 19,21,45,
25         fhdwr2|frhb2|seln3 [ ] PS(3, 1) 1000000 |4,1) -> 19,21,29,
26         fhdwr2|frhb2|seln2|Vps1 [T] PS(3, 2) 1 |4,2) -> 19,21,28,41,
27         fhdwr2|frhb2|seln2|Vps1 [x] PS(3, 3) 10 |4,3) -> 19,21,28,41,
28         nu [ ] PS(3, 4) 1000000 |4,4) ->
29         fhdwr2|frhb2|ps2|sel1 [x] PS(3, 5) 4 |4,5) -> 19,21,31,33,
30         fhdwr2|frhb2|ps2|sel1 [T] PS(3, 6) 1 |4,6) -> 19,21,31,33,
31         trb [ ] PS(3, 7) 1000000 |4,7) -> 35,

```

FIGURE 5.10: List of triggers.

The trigger we use in this work (number 10 in the trigger list) is set to activate for a coincidence of the following conditions **fhdwr2**, **frhb2** and **seh2**. The first two conditions concern the Forward Detector and the particles passing through it - **fhdwr2** means that there were at least two matching tracks in the Forward Trigger Hodoscope Forward Window Counter and Forward Range Hodoscope. This means that a signal (energy deposit above threshold) was detected in corresponding ϕ angle modules for each of those detectors. The second condition, **frhb2** triggers when there are at least two signals in the second layer of the Forward Range Hodoscope.

The last condition, **seh2** is related to the Central Detector, it activates when there are at least two clusters with energy deposits above a high threshold (around 100 MeV).

With those criteria, the trigger should accept charged and neutral η meson decays such as $\eta \rightarrow e^+e^-\gamma$ or $\eta \rightarrow \gamma\gamma$.

5.3.1 Trigger efficiency

In order to estimate of the efficiency of a trigger i , we will compare it to another trigger j . Both triggers should be sensitive to the same channel. Let N be the total number of events of a selected channel and N_i (respectively N_j) the number of those events that activate trigger i (respectively j).

We then calculate the efficiency in the following way:

$$N_i = N \cdot P_i \quad N_j = N \cdot P_j \quad N_{ij} = N \cdot P_{ij} \quad (5.3)$$

In this equation, N_{ij} is the number of events that activate both triggers i and j . P_i is the probability that trigger i accepts the signal event, we therefore use this value as an estimation of the trigger i efficiency. The probability that both triggers will fire is $P_{ij} = P(i \cap j)$. Making the assumption that trigger i and j are independent this probability becomes simply $P_{ij} = P_i \cdot P_j$ and the efficiency is:

$$P_i = \frac{N_{ij}}{N_j} \quad (5.4)$$

In reality the triggers are rarely independent, thus we must consider the nature of their dependency. In this case $P_{ij} = P(i \cap j) = P(i|j) \cdot P(j)$ and we should compare $P(i|j)$ and $P(i)$. As stated in the beginning of this section, both triggers are sensitive to the same channel therefore $P(i|j) > P(i)$. This means that our estimation of efficiency provides a lower limit.

5.3.1.1 Trigger efficiency: $\eta \rightarrow \gamma\gamma$ channel.

Here we compare TR10 and TR26 with respect to the neutral decay $\eta \rightarrow \gamma\gamma$. The only difference between those triggers is that TR26 accepts only neutral tracks but under a lower energy threshold and add a veto on the PS detector. Trigger T26 is less strict with respect to $\eta \rightarrow \gamma\gamma$ channel since this decay does not have any charged track that could be rejected by the veto on PS while the SEC energy threshold is higher for T10.

We have selected the $\eta \rightarrow \gamma\gamma$ decay by applying the selection criteria described in section 5.2.

TABLE 5.7: Neutral selection trigger combinations

Triggers	Number of events
TR10(\neg TR26)	8248
(\neg TR10)TR26	81040
TR10TR26	169741

The number of events for different combinations of those triggers is shown in figure 5.7. Using the formula 5.4 on those values we get a relative efficiency of $(67.7 \pm 0.2)\%$.

5.3.1.2 Trigger efficiency: $\eta \rightarrow e^+e^-\gamma$ channel.

The same method was applied to the $\eta \rightarrow e^+e^-\gamma$ channel. The two compared triggers TR10 and TR29 differ only with respect to the following conditions:

- TR10 - requirement of two clusters in SEC above a high threshold
- TR29 - requirement of one cluster in SEC above a low threshold and two hits in PS

The requirement of two hits in PS is irrelevant since the initial data selection contains this condition. Therefore, all signal events that trigger TR10 should, a fortiori, activate TR29.

TABLE 5.8: Charged selection trigger combinations

Triggers	Number of events
TR10(\neg TR29)	139
(\neg TR10)TR29	308
TR10TR29	204

The number of events for different combinations of those triggers is shown in table 5.8³. Using the formula 5.4 on those values we get a relative efficiency of $(39.8 \pm 3.3)\%$.

5.3.2 Trigger stability

We use the term of stability to characterize the fluctuation, over the time of the experimental data taking, of the ratio between the number of events selected by two different

³NB: The selection was based on the analysis described in chapter 6.

triggers, one of them being TR10 that we use in the data selection. This parameter, measured as a relation between TR10 to TR17, is shown in figure 5.11. Trigger 17 is selecting events with at least one signal coming from the forward part of the PS (thin plastic scintillator in the CD - sensitive on charged particles) and one signal in the center part of PS.

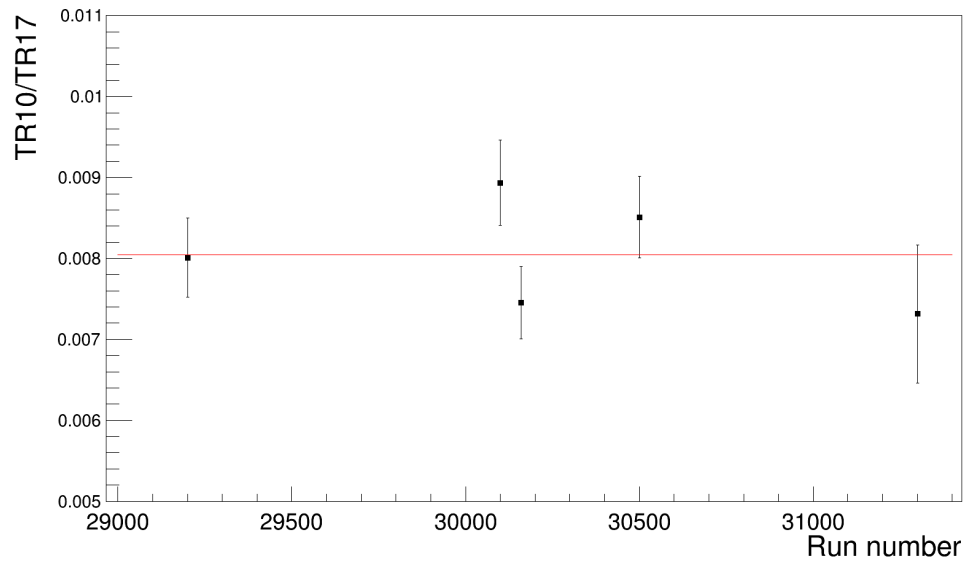


FIGURE 5.11: The trigger stability.

We can observe that this value presents some variation through the duration of the experiment but within reasonable limits.

Chapter 6

Analysis of $\eta \rightarrow e^+e^-\gamma$ channel

The main goal of this work is either to find evidence of the decay of a dark massive boson $U \rightarrow e^+e^-$ or to exclude the hypothesis that such a signal is present in our data sample. The latter is equivalent to the determination of an upper limit on the coupling parameter between the dark boson and leptons. The significance of both possible statements is directly related to the available statistics. Such a decay could be observed as a superimposed bump in the spectrum of invariant masses of e^+e^- pairs that could not be explained by any known reaction. We decided to look for such a signature in the relevant spectrum of the $\eta \rightarrow e^+e^-\gamma$ channel. Additionally in this decay we can extract, from a large set of η Dalitz candidates, the transition form factor of the η meson (see 1.4.1). Therefore, the first step consists in collecting the largest possible sample of $\eta \rightarrow e^+e^-\gamma$ events candidates.

In order to do this, we have to implement a set of analysis conditions that selects signal enhanced data sample. The relative content of the $\eta \rightarrow e^+e^-\gamma$ channel is supposed to increase at each step of this process.

The rate at which the proton proton collisions occur is about $10^6 s^{-1}$. On the one hand, this gives an idea about the difficulty of the task for the data acquisition system to efficiently store most of the relevant information. On the other hand, events saved by the DAQ often contain information generated from multiple overlapping collisions. In order to select a particular reaction, we need to get rid of background channels by implementing suitable conditions in the analysis program.

6.1 Multiplicity conditions.

The multiplicity conditions consist of selecting events based on the number of charged and/or neutral tracks (after reconstruction) that this event contains. In principle, our

search should only focus on events with one neutral track, the photon, and two oppositely charged tracks, the e^+e^- pair. In reality, we must proceed more carefully. It would be wrong to set up the selection criteria on the number of tracks directly requiring $C = 2$ and $N = 1$. For charged tracks, we must take into consideration only electrons, therefore the identification and pion rejection must come first. Also, we should only deal with particles that give rise to a reasonably high signal, thus setting a threshold on the energy deposit of each track (in our case 20 MeV). Last but not least, in order to reject random background (pile-ups), we must consider only those tracks that are within a given time window - this will be discussed in section 6.2.

Nevertheless, for an illustrative purpose only, we present the histograms of the invariant mass of the two charged particles system (assuming electron mass) for different channels simulation (PLUTO and WMC). Figures 6.1, 6.2 and 6.3 represent the η decays while figures 6.4, 6.5 and 6.6 show the simulation of the direct pion production channels. The figure 6.7 shows the simulation of $10^6 pp \rightarrow p\Delta^+ \rightarrow ppe^+e^-$ events.

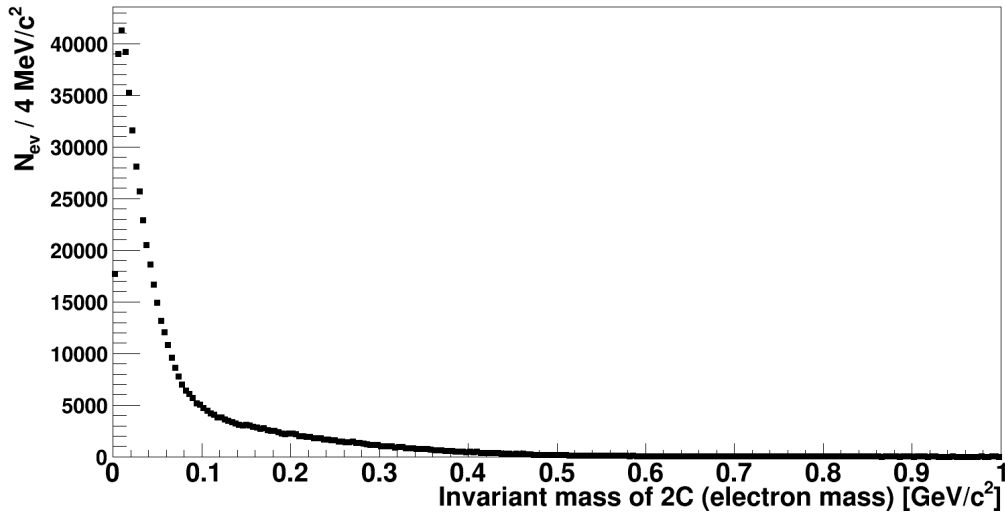


FIGURE 6.1: Invariant mass of two charged particles system (with the assumption of electron masses): $5 \cdot 10^6 \eta \rightarrow e^+e^-\gamma$ events.

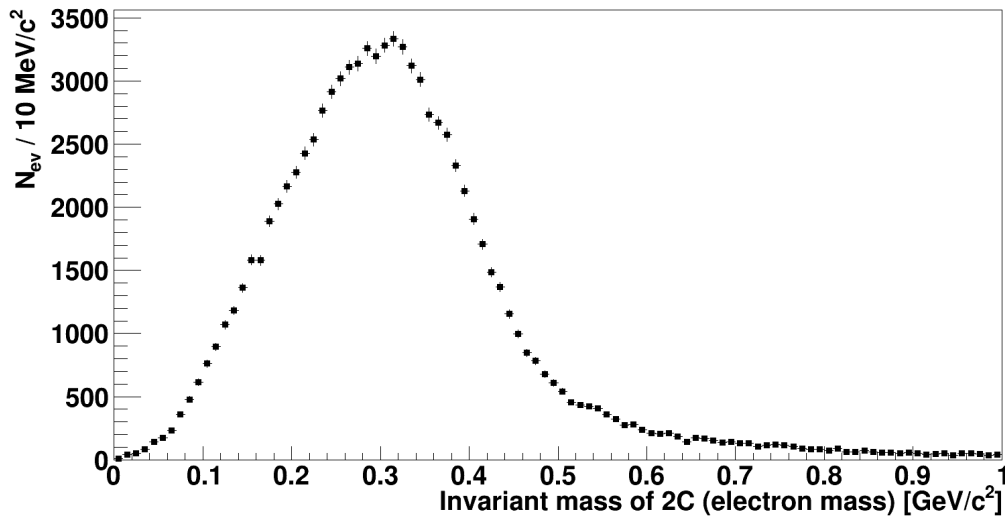


FIGURE 6.2: Invariant mass of two charged particles system (with the assumption of electron masses): $8 \cdot 10^5$ $\eta \rightarrow \pi^+\pi^-\gamma$ events.

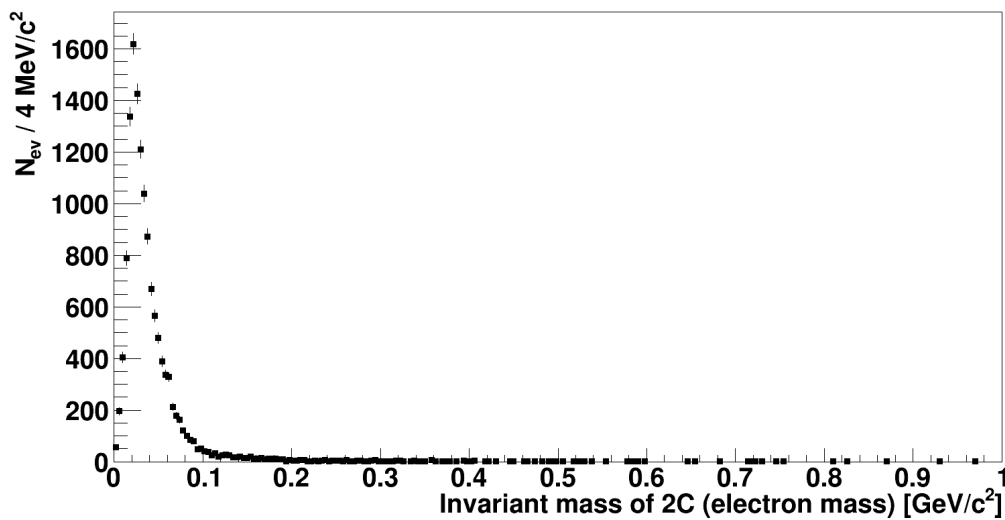


FIGURE 6.3: Invariant mass of two charged particles system (with the assumption of electron masses): $1 \cdot 10^7$ $\eta \rightarrow \gamma\gamma$ events.

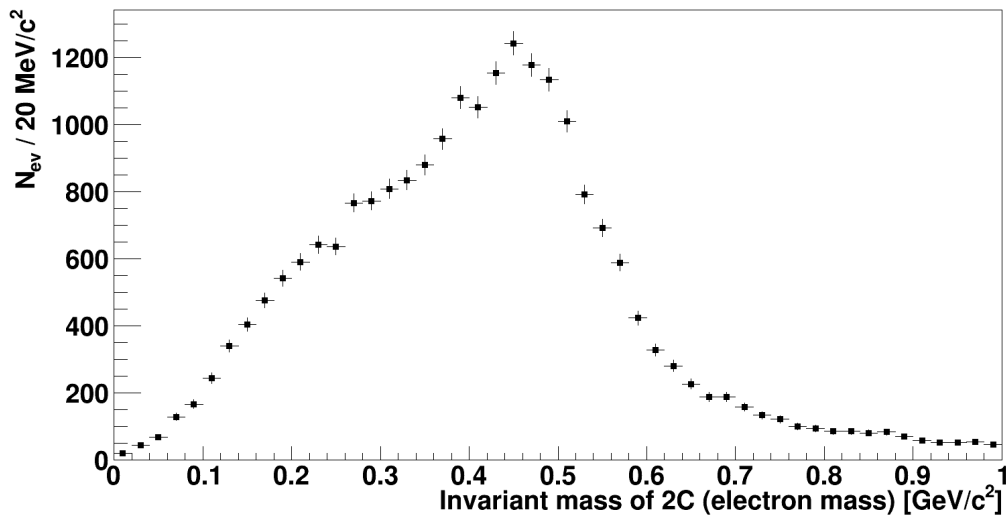


FIGURE 6.4: Invariant mass of two charged particles system (with the assumption of electron masses): $14 \cdot 10^6$ $pp \rightarrow pp\pi^+\pi^-$ events.

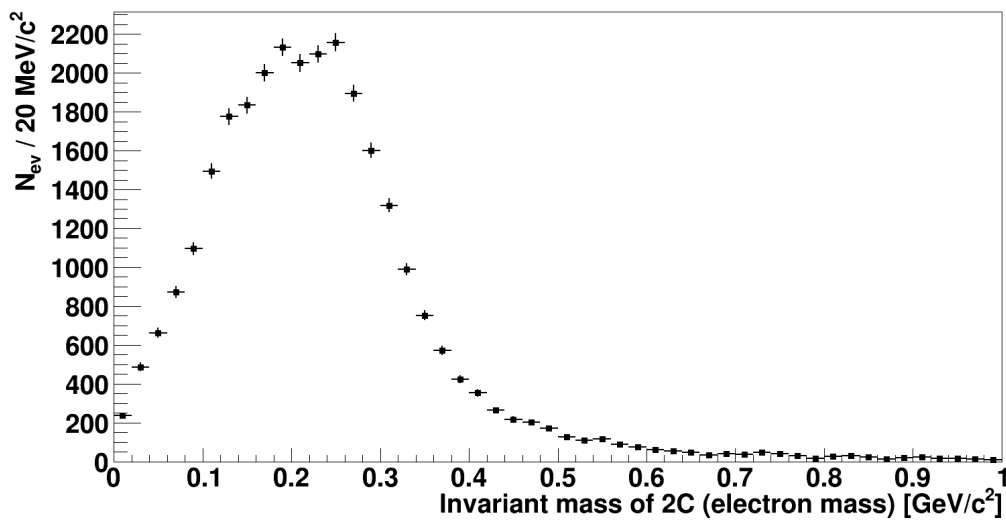


FIGURE 6.5: Invariant mass of two charged particles system (with the assumption of electron masses): $1 \cdot 10^6$ $pp \rightarrow pp\pi^+\pi^-\pi^0$ events.

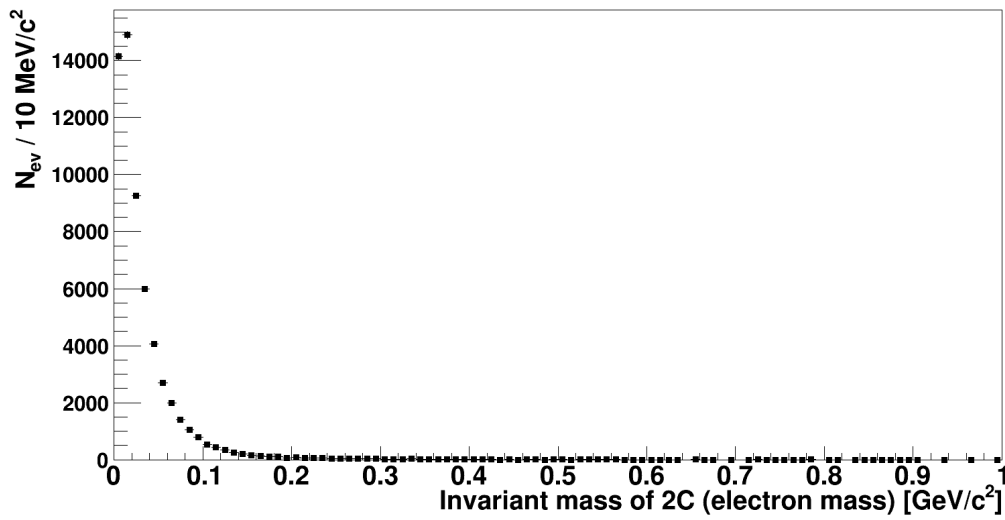


FIGURE 6.6: Invariant mass of two charged particles system (with the assumption of electron masses): $1 \cdot 10^7$ $pp \rightarrow pp\pi^0 (\rightarrow \gamma\gamma) \pi^0 (\rightarrow e^+e^-\gamma)$ events.

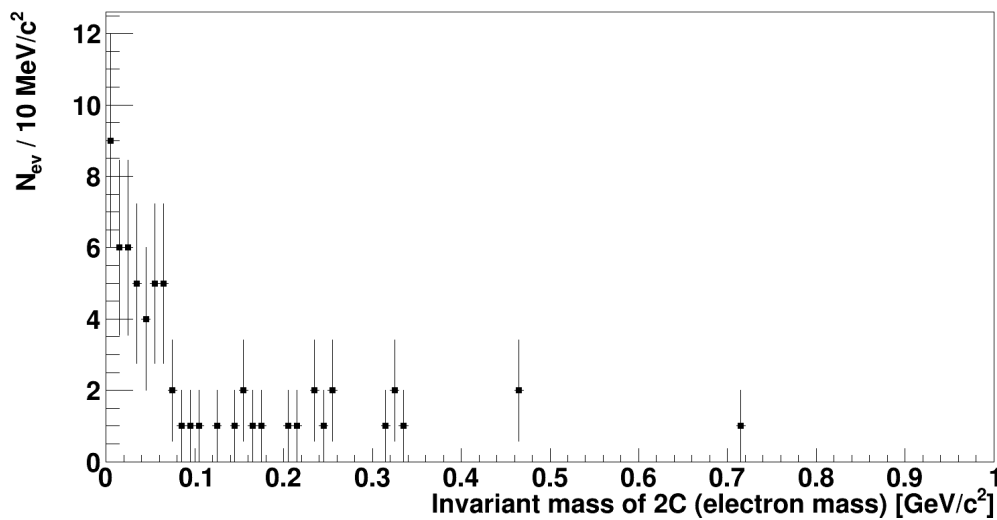


FIGURE 6.7: Invariant mass of two charged particles system (with the assumption of electron masses): 10^6 $pp \rightarrow p\Delta^+ \rightarrow ppe^+e^-$ events.

6.2 Time conditions.

The signals produced by particles that originate from the same event, for example a meson decay, should occur within some reasonable time window. The width of this window is determined by several factors. On the one hand, the physical characteristics of the particle such as its velocity or momentum, charge, mass and its interaction properties all have an influence the particle path inside the detector, thus on the time of the signal. On the other hand, the detector itself plays an important role - the physical properties of the active materials, cable lengths etc. The time of a track is determined by the TDC response of a given detector element. For charged particles in the central detector - mostly electrons, pions and protons - it corresponds to the signal from either the plastic scintillator barrel (PSB) or the electromagnetic calorimeter (SE). The times of all neutral particles are taken from SE and the time of particles in FD (mostly charged protons or pions) is set by the response of the forward trigger hodoscope detector (FTH). In figures 6.8a and 6.8b we show time differences between particles in the central detector (CD), neutral (N) or charged (C), and protons in the forward part of the WASA detector (FD). Based on those spectra, we apply the following selection criteria in order to reduce most of the the overlapping background:

- $-21 \text{ ns} < \text{time}_{\text{CDN}} - \text{time}_{\text{FD}} < 5 \text{ ns}$
- $-16 \text{ ns} < \text{time}_{\text{CDC}} - \text{time}_{\text{FD}} < -6 \text{ ns}$

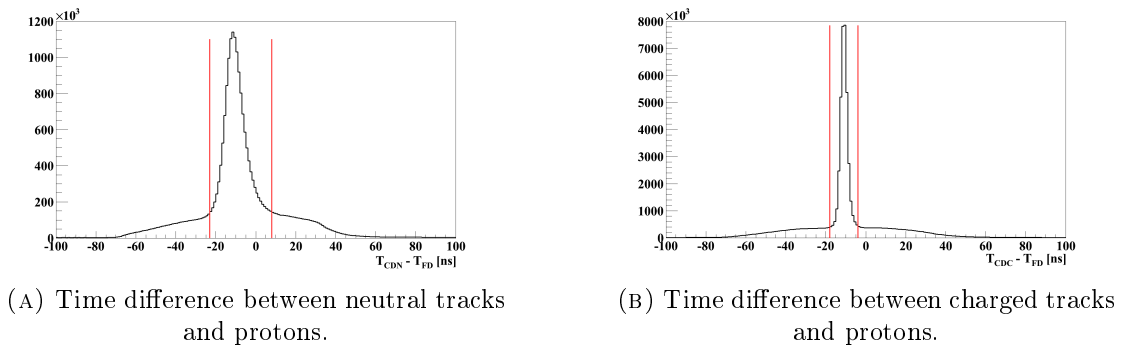
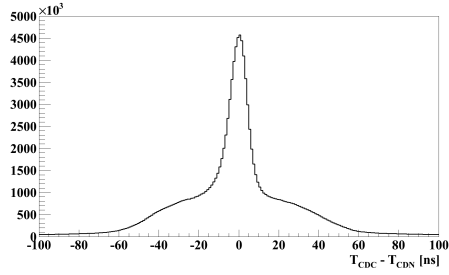


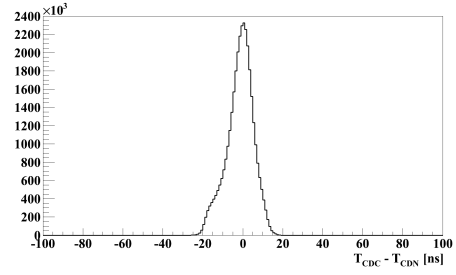
FIGURE 6.8: Cuts applied on the time differences of particles in CD and FD.

On figures 6.9a and 6.9b we observe the indirect effect of those cuts on the spectra of time differences between charged and neutral tracks in CD.

Further in the analysis, after the selection of an electron pair and a photon that, we assume, originate from the same Dalitz decay event, we apply one more condition on the time difference between the electrons and the photon:



(A) Time difference between charged and neutral tracks in CD before time cuts relative to protons in FD.



(B) Time difference between charged and neutral tracks in CD after temporal cuts relative to protons in FD.

FIGURE 6.9: Effect of temporal cuts relative to protons in FD on the time difference between particles in CD.

- $-20 \text{ ns} < \text{time}_{\text{CDC}} - \text{time}_{\text{CDN}} < 20 \text{ ns}$

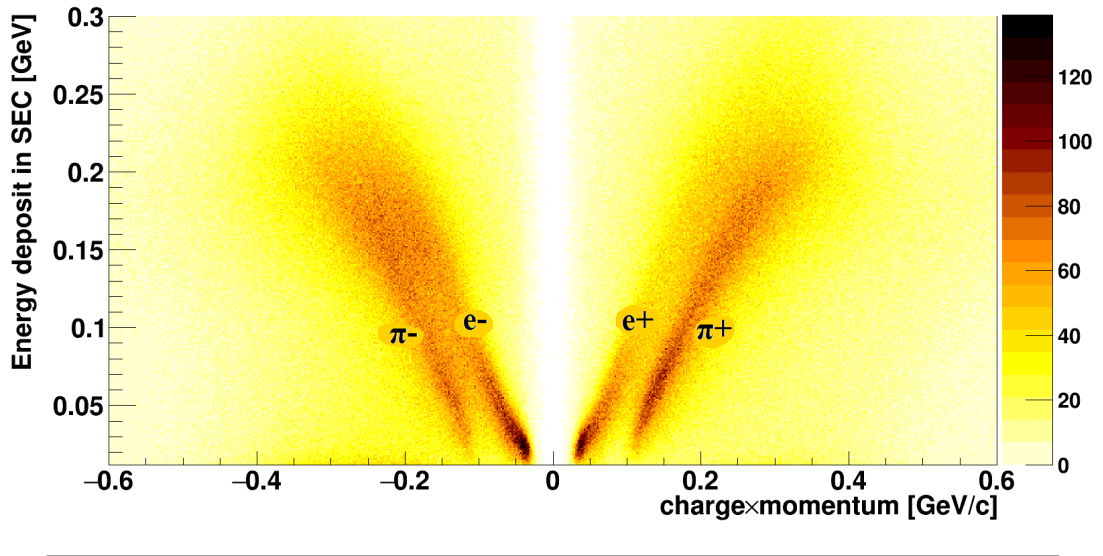
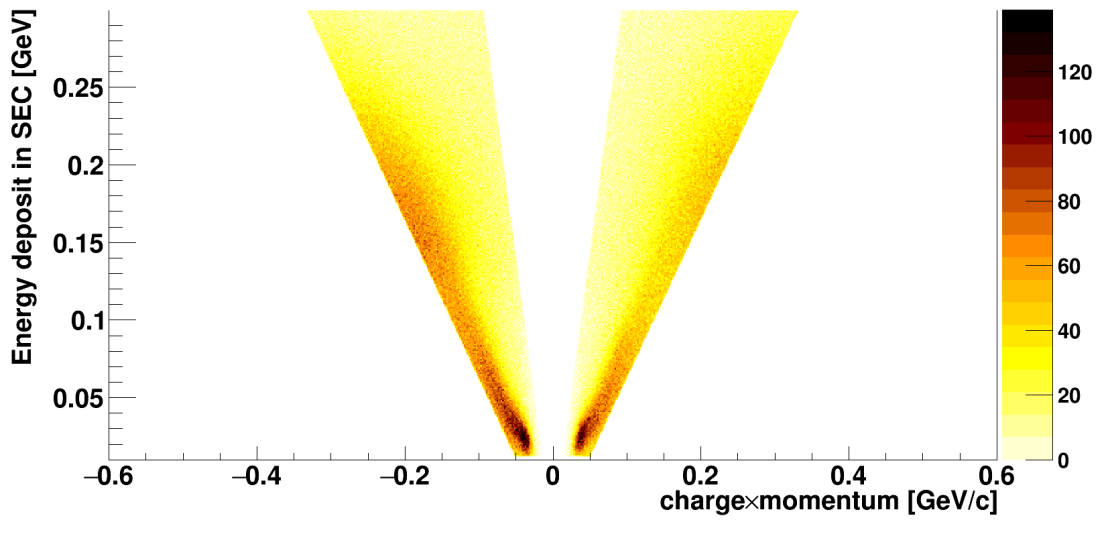
6.3 Particle identification method.

6.3.1 ΔE -p method - basics.

The pions are produced copiously in η meson decays as well as directly in proton inelastic collisions. The cross section for η meson production is around $12 \mu\text{b}$ while the direct pion production is of the order of $30 - 40 \text{ mb}$, thus three orders of magnitude higher. Our ability to distinguish between electrons and pions is therefore one of the most important aspects of the analysis. The method we use to identify those particles is based on the difference in their pattern observed on the histogram that relates the energy loss of a track in the central detector versus the momentum of this track multiplied by its charge (*signed momentum*). In figure 6.10 which is generated from a data sample, we can see four partially overlapping bands, a pair for each charge state. The pions are on the lower band and the electrons (positrons) are located on the higher band. We can proceed in two ways:

- we apply an arbitrary graphical cut
- we apply a graphical cut using a well-defined procedure

Given the two bands are well visible on the histogram (even if they are overlapping for large momenta), we can use the first method to disentangle pions and electrons. This is presented in the figure 6.11 .

FIGURE 6.10: Energy deposit in SEC versus charge \times momentum plot - data.FIGURE 6.11: Energy deposit in CD versus charge \times momentum plot - graphical cut.

6.3.2 ΔE -p method - developed procedure.

Now, let's discuss the other method that was developed as an attempt to optimize the electron selection. We have seen that the identification of the charged particles is one of the most important and most difficult issues in this analysis. One of the main objections that one can make with respect to the presented graphical method is that it is based on subjective appreciation. At higher momenta (energies), electron and pion bands are overlapping and the applied graphical cut adds uncertainties that are difficult to estimate. Here, we propose a well defined procedure, based on the very same histograms, to

separate electrons and pions.

First, we need to generate Monte Carlo simulations (WMC) of η meson decays: one sample of events with electrons in the final state and one sample with pions in the final state. Therefore, we simulate one million events for both $\eta \rightarrow e^+e^-\gamma$ and $\eta \rightarrow \pi^+\pi^-\gamma$ channels. We plot the same histograms used in the last section 6.3.1 i.e. the energy deposited in the central detector versus the particle momentum multiplied by the particle charge. We then fit a line to those electronic and pionic bands (e.g. by using a least-squares fit algorithm on an area of the histogram limited to those bands). Given the problem with the energy calibration mentioned in section 3.1.2, the pion band fit is based on data rather than on simulation. The result of such procedure is shown in figure 6.12. Then, we use the data sample to compute and plot the distances between each data point on those histograms and the fitted line that corresponds to one of the fitted bands (electrons or pions). Finally, we can draw such plots for different energies (horizontal slices): 60 MeV, 100 MeV, 300 MeV and 500 MeV.

We identify as electrons (respectively pions) those events that are represented by a distribution of distances with respect to the electronic (respectively pionic) line that is centered around zero. In figure 6.13 we can observe two peaks: one centered at zero, identified as electrons, and a second broader peak, pions, centered at some distance from zero (energy dependence).

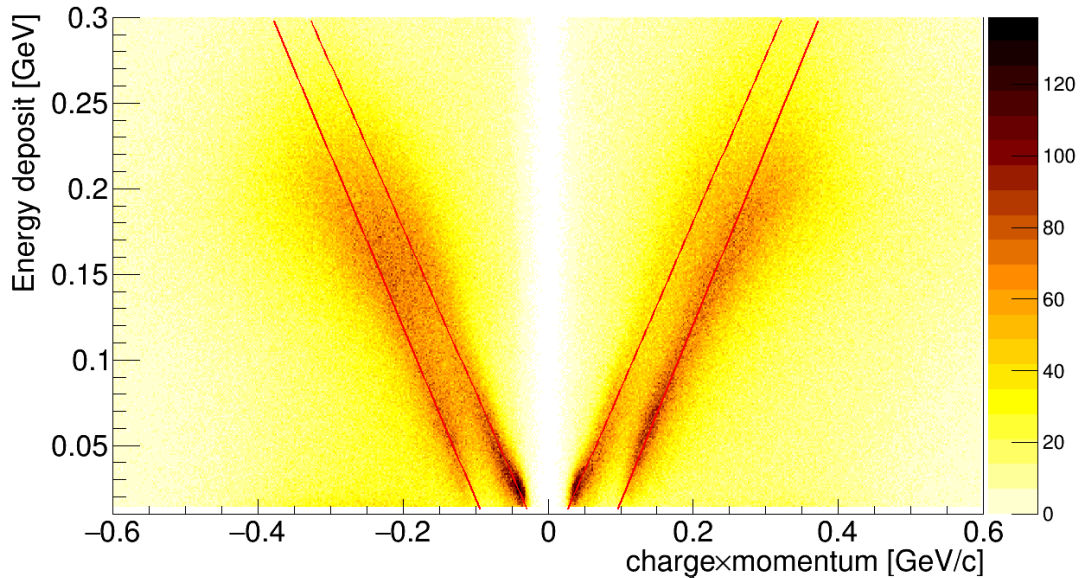


FIGURE 6.12: Particle identification fit.

In figure 6.13 we can draw a line (corresponding to one point in figure 6.12) that maximizes a figure of merit. The latter depends on the considered reaction. If the electrons represent our signal with N_e being their number on one side of the line and pions are

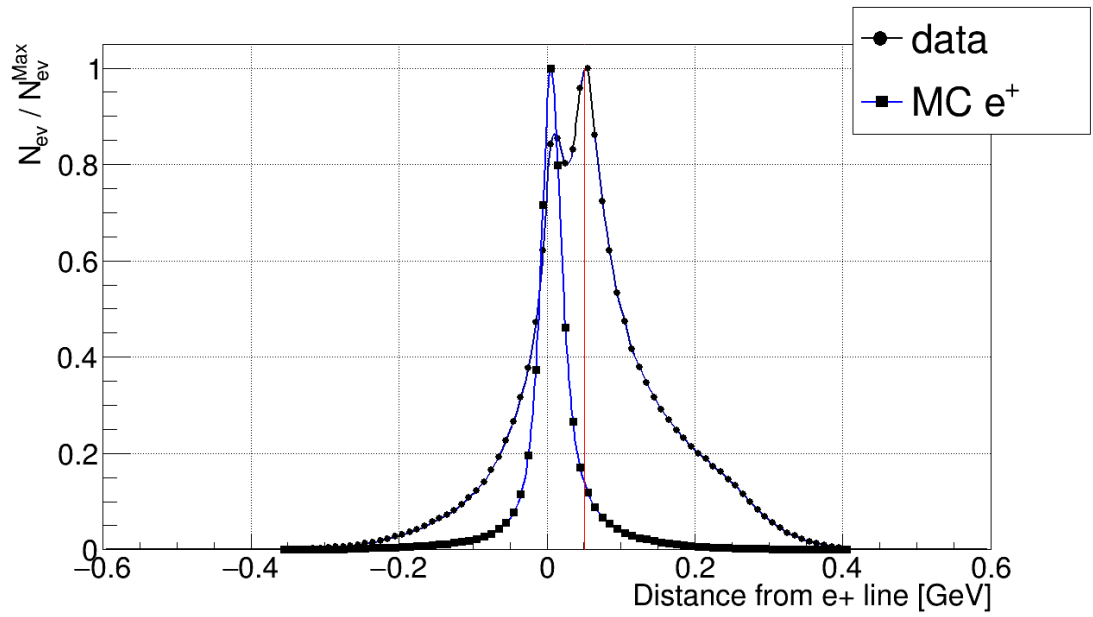


FIGURE 6.13: Normalized distances from the e^+ fitted line. The vertical red line represents the position of the π^+ line.

the background (with N_π being the number of pions on the same side of the line) we can maximize the ratio $\frac{N_e}{\sqrt{N_e+N_\pi}}$. When our signal is very weak (compared to background) this reduces to $\frac{N_e}{\sqrt{N_\pi}}$. Finally, if our reaction is abundant it could make sense to use $\frac{N_e}{N_\pi}$ ratio. We could also take into account the effects on the acceptance. If we repeat this process for a few projections (energy slices) and for each charge, we can construct two oblique separation lines in figure 6.12 and use them as an identification condition for our analysis.

This alternative identification method was developed and is available for future analysis. In this work we will not use it for two reasons. First of all, for consistency we should perform a precise energy calibration for pions (see section 3.1.2). Secondly, we will show that the simple graphical cut identification described in section 6.3.1 is sufficient to reduce and control the pion content of our data.

6.4 Rejection of the background from external pair production

Photons passing through the detector material can interact with nuclei and produce e^+e^- pairs. This mechanism is called pair production or external photon conversion. Although the WASA experiment is designed to limit as much as possible this effect, it still represents a large contribution to the e^+e^- spectra we look at. The main source of this background is the beam pipe. When electrons are produced off vertex, on the beam pipe, their tracks are wrongly reconstructed. The reconstruction algorithm in the MDC assumes that those tracks originate from the interaction point $(0,0,0)$ rather from their true origin located on the beam pipe (see figure 6.14).

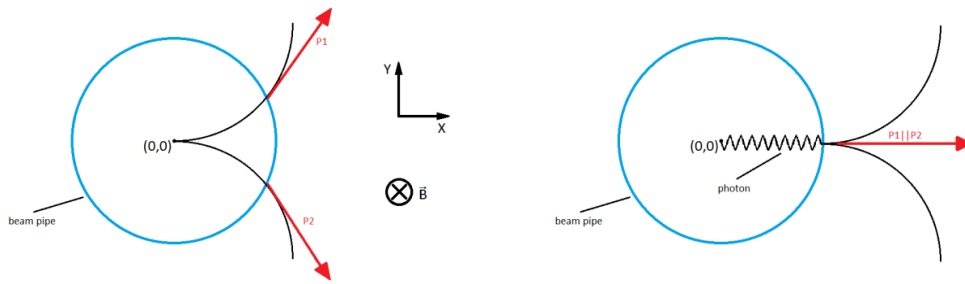


FIGURE 6.14: Momenta vectors at the beam pipe for electrons from $\eta \rightarrow e^+e^-\gamma$ (left) and from photon conversion in the beam pipe material (right).

If we perform calculations assuming that the interaction point is somewhere on the beam pipe, the invariant mass (IM_{e⁺e⁻}) of e^+e^- pairs that were created there should be zero - their momenta vectors should be parallel to each other. The leptonic pairs coming from η meson Dalitz decays are generated in the $(0,0,0)$ interaction point and are drawn apart by the magnetic field so their tracks are not longer parallel when they reach the beam pipe and thus their invariant mass on the beam pipe is non zero. The second feature that allows us to separate those two contributions is the radius of the closest approach (CA) of the two e^+ and e^- tracks in the XY plane. The projection of the beam pipe can be schematically described as a torus with inner radius of 30 mm. Therefore, we can expect that the positions of the closest approach of leptonic pairs from external photon conversion are located around 30 mm while those originating from η Dalitz decay are closer to 0. Finally, we plot CA versus IM_{e⁺e⁻} and perform a graphical cut to separate the signal from the external conversion background. Figures 6.15a and 6.15b show this histogram for the simulated signal $\eta \rightarrow e^+e^-\gamma$, background $\eta \rightarrow \gamma\gamma$ while the figure 6.16 represents the data and the cut we apply.

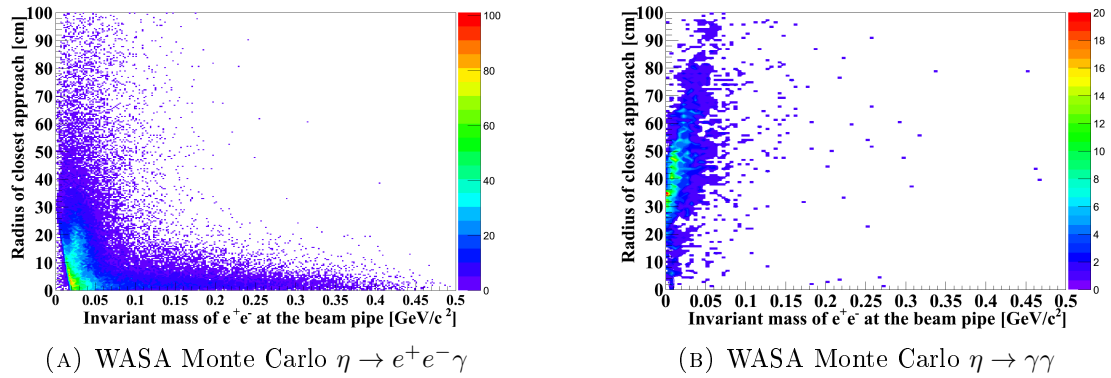


FIGURE 6.15: Radius of closest approach versus the invariant mass of e^+e^- at the beam pipe.

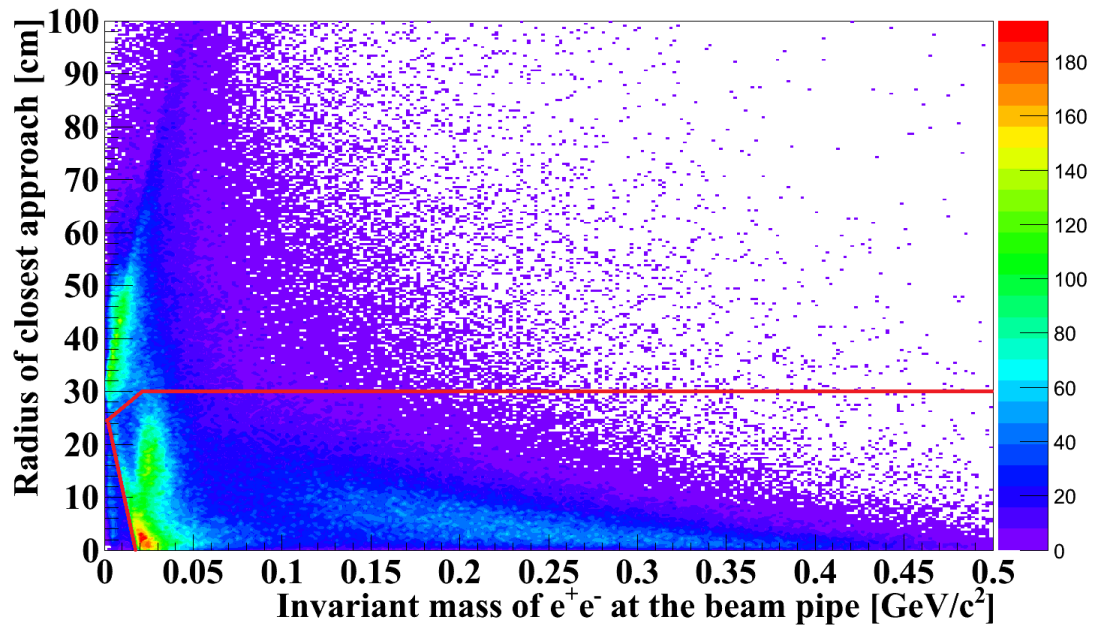


FIGURE 6.16: Radius of closest approach versus the invariant mass of e^+e^- at the beam pipe - data with graphical conversion cut.

6.5 Selection based on total missing energy versus total missing mass plot.

We use the mass difference between pions and electrons ($139 \text{ MeV}/c^2$ versus $0.5 \text{ MeV}/c^2$) to select electrons and reject pions by graphically cutting on the histogram of total missing energy versus total missing mass.

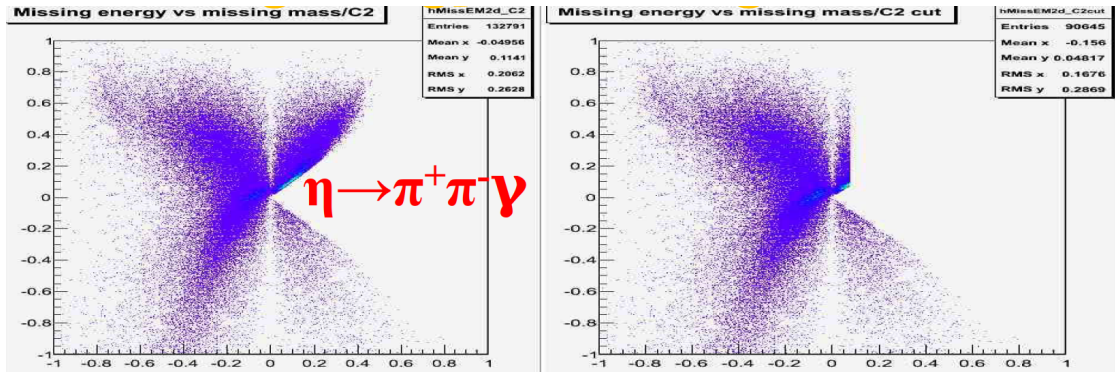


FIGURE 6.17: Total missing energy versus total missing mass for $\eta \rightarrow \pi^+\pi^-\gamma$ simulation.

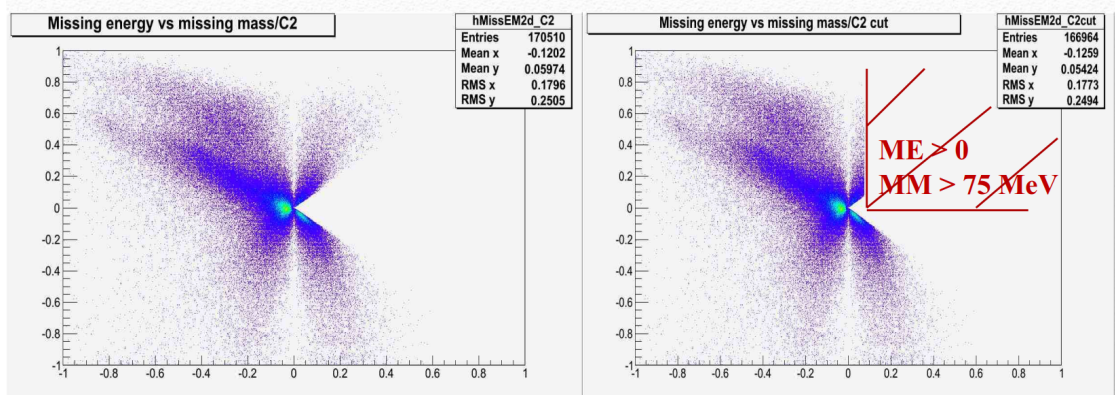


FIGURE 6.18: Total missing energy versus total missing mass for $\eta \rightarrow e^+e^-\gamma$ simulation.

In figure 6.17, we see the histogram of the total missing energy versus the total missing mass for $\eta \rightarrow \pi^+\pi^-\gamma$ decay channel. By comparison with the same histogram for the $\eta \rightarrow e^+e^-\gamma$ channel (6.18), we see that excluding the region with negative missing energy and missing mass above $75 \text{ MeV}/c^2$ rejects only a small fraction of signal but strongly reduces the contribution from $\eta \rightarrow \pi^+\pi^-\gamma$ channel (and other pionic channels - see next sections).

Figure 6.19 shows the total missing energy versus the total missing mass for $pp \rightarrow pp\pi^+\pi^-$ decay channel and the effect of the cut on this reaction.

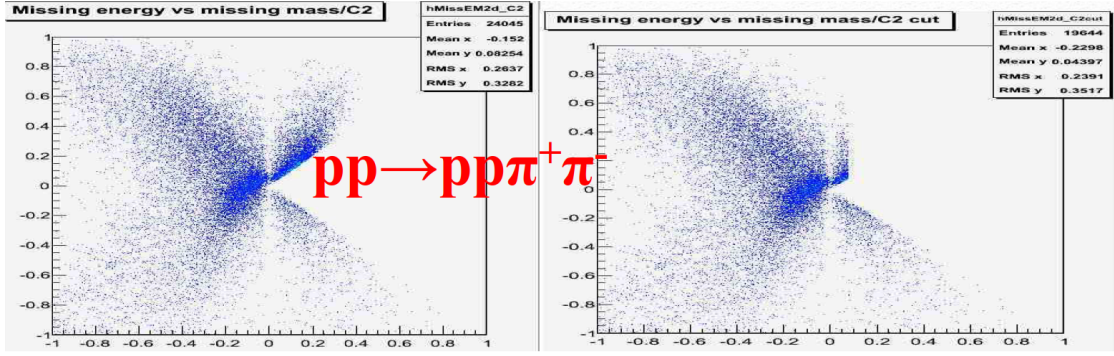


FIGURE 6.19: Total missing energy versus total missing mass for $pp \rightarrow pp\pi^+\pi^-$ simulation.

Figure 6.20 shows the total missing energy versus the total missing mass for $pp \rightarrow pp\pi^+\pi^-\pi^0$ decay channel and the effect of the cut on this reaction.

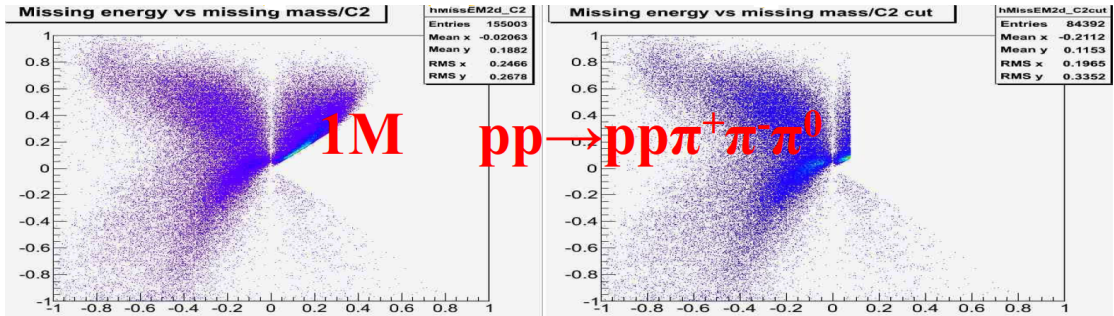


FIGURE 6.20: Total missing energy versus total missing mass for $pp \rightarrow pp\pi^+\pi^-\pi^0$ simulation.

6.6 Angular distributions in the $\eta \rightarrow e^+e^-\gamma$ channel

6.6.1 Angle between the η meson and the beam direction in laboratory frame.

The differences in the angular distributions of particle tracks that come from different reactions allow us to disentangle between different channels. Therefore we can constrain our sample by applying appropriate angular conditions. First of all, we are interested in a decay of the η meson that is produced in the collision of protons $pp \rightarrow pp\eta$. Therefore, we can reconstruct the missing four-vectors for two protons such as: $\mathbf{P}_{\text{miss}} = \mathbf{P}_{\text{b}} + \mathbf{P}_{\text{t}} - \mathbf{P}_{\text{p1}} - \mathbf{P}_{\text{p2}}$ where \mathbf{P}_{i} on the right side of the equation stand for the four-vector related to the beam, target and the two reconstructed (scattered) protons. The left side of the equation represents the missing four-vector. In case an η meson is produced it

would be \mathbf{P}_η . The figure 6.21 represents θ_{LAB} (angle with respect to the beam or Z axis in the laboratory reference frame) of this missing vector for two different Monte Carlo simulations, one with η meson production $pp \rightarrow pp\eta$ (blue), the other with direct pion production $pp \rightarrow pp\pi^+\pi^-\pi^0$ (black). We see that for reactions with pion production, the tail of this distribution is larger, thus it seems reasonable to make a cut on 30° (red line). Figure 6.22 shows the same distribution for the data sample.

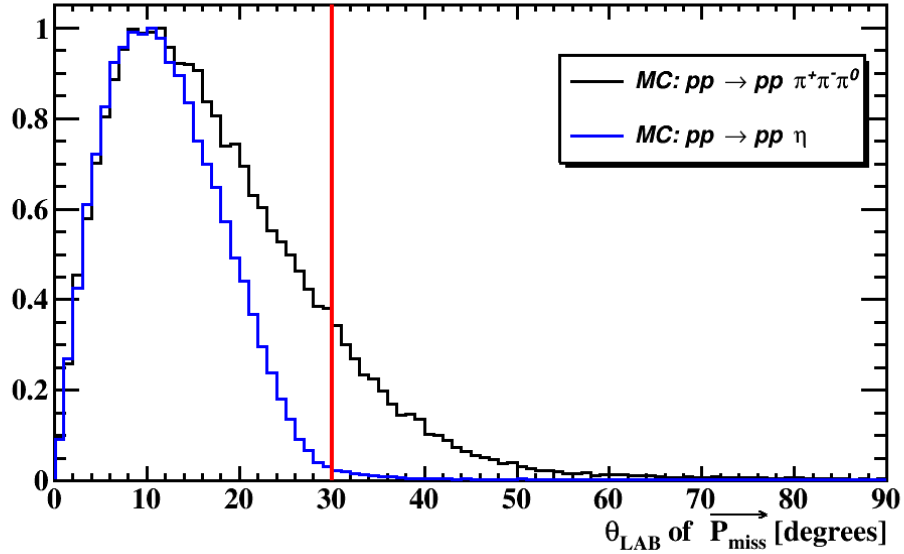
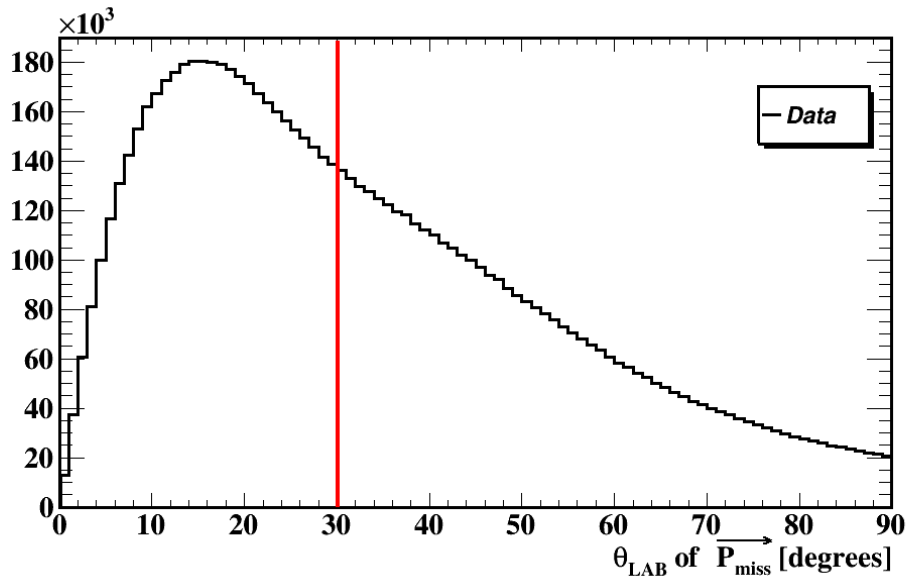
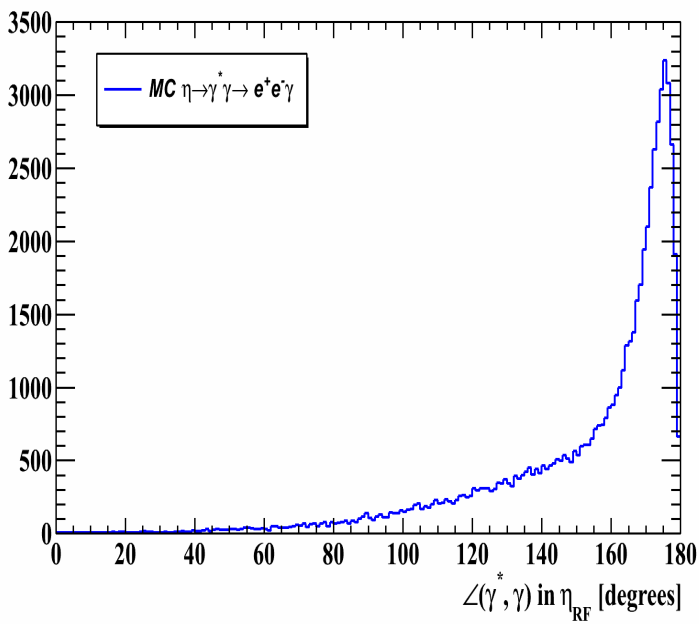
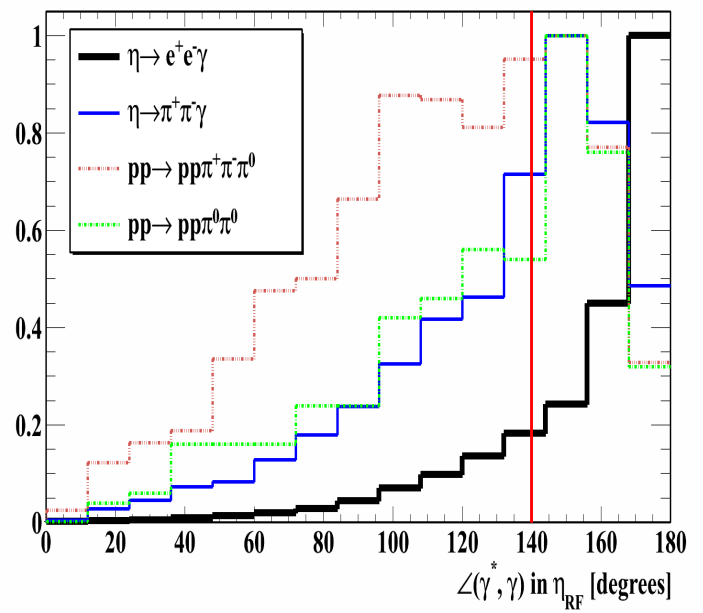


FIGURE 6.21: Theta angle of η meson in the laboratory reference frame - Monte Carlo simulations.

6.6.2 Angle between γ^* and γ in η meson rest frame.

The other important angular distribution, directly related to the selection of $\eta \rightarrow \gamma^*\gamma \rightarrow e^+e^-\gamma$ channel, is the angle between the virtual photon or dilepton γ^* and the true photon γ in the rest frame of η meson. Given the law of momentum conservation, this angle should be equal to 180° . In reality, due to uncertainties and errors introduced by the detection and measurement processes a distribution of angles appears (see figure 6.23a). The figure 6.23b represents those angular distributions for $\eta \rightarrow e^+e^-\gamma$ and three background channels normalized to the maximal value in order to emphasize the differences in shape. To improve the signal-to-background ratio, we cut-off events with angle between γ^* and γ in η meson rest frame lower than 140° .

FIGURE 6.22: Theta angle of η meson in the laboratory reference frame - data.(A) Wasa Monte Carlo $\eta \rightarrow e^+e^-\gamma$ 

(B) Different Wasa Monte Carlo channels

FIGURE 6.23: Distributions of the angle between γ^* and γ in η rest frame.

6.7 Summary of the $\eta \rightarrow e^+e^-\gamma$ selection

The table 6.1 summarizes the effects of the $\eta \rightarrow e^+e^-\gamma$ selection criteria on $\eta \rightarrow e^+e^-\gamma$ and different background channels.

TABLE 6.1: $\eta \rightarrow e^+e^-\gamma$ and background reactions

Reaction	N_{sim}	final selection	Acceptance	$N_{expected}$
$\eta \rightarrow e^+e^-\gamma$	$5 \cdot 10^6$	121447	0.0243	~ 10900
$pp \rightarrow pp\pi^0 (\rightarrow \gamma\gamma) \pi^0 (\rightarrow e^+e^-\gamma)$	10^7	492	$4.9 \cdot 10^{-5}$	~ 1200
$\eta \rightarrow \gamma\gamma$	10^7	176	$1.8 \cdot 10^{-5}$	~ 450
$\eta \rightarrow \pi^+\pi^-\gamma$	$4 \cdot 10^6$	2	$5 \cdot 10^{-7}$	~ 1
$pp \rightarrow pp\pi^+\pi^-\pi^0$	$3 \cdot 10^6$	1	$3.3 \cdot 10^{-7}$	~ 15
$pp \rightarrow pp\pi^+\pi^-$	$1.4 \cdot 10^7$	0	-	-
$pp \rightarrow p\Delta^+ \rightarrow ppe^+e^-$	10^6	0	-	-

6.8 Radius of closest approach after selection.

The only background channels that survive the selection process are $\eta \rightarrow \gamma\gamma$ and $pp \rightarrow pp\pi^0 (\rightarrow \gamma\gamma) \pi^0 (\rightarrow e^+e^-\gamma)$. In order to prove this statement we present the figure 6.24 that shows the distribution of the radius of the closest approach between e^+e^- pairs, i.e. the projection on the XY axis of the vector constructed by joining the center of the shortest segment between the two helices to the origin (interaction point).

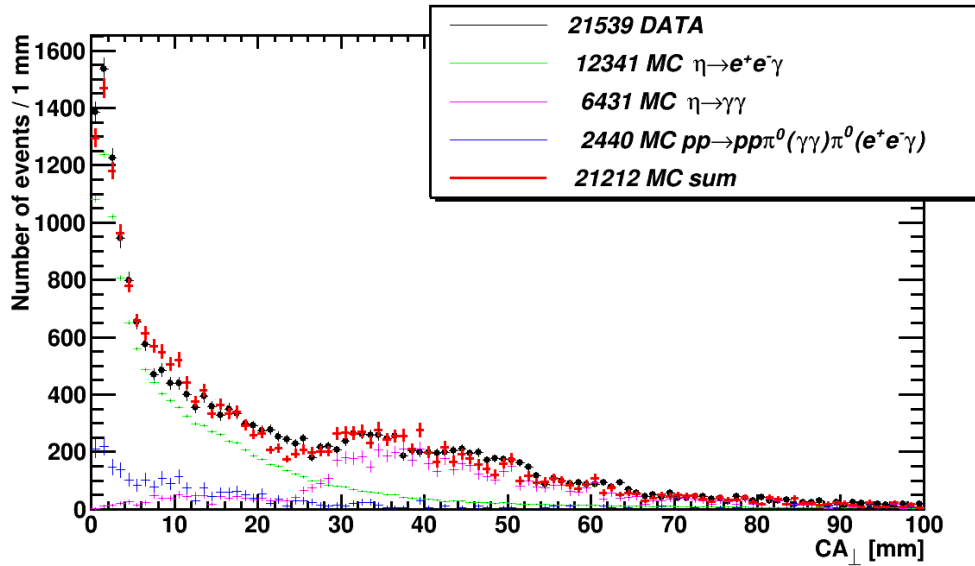


FIGURE 6.24: Radius of closest approach.

Pileup contribution doesn't appear on this plot for it is distributed randomly, often outside the considered range. We observe that the simulation of the $\eta \rightarrow e^+e^-\gamma$ channel and of the two background channel describes data with good accuracy.

6.9 Method for non- η background suppression.

In the previous sections, we made several selection cuts in order to extract our signal, the $\eta \rightarrow e^+e^-\gamma$ decay. The purpose of those conditions is to reject as much as possible of the background channels. Nevertheless, we know that there is some remaining background that, for non- η decays, should have a continuous contribution in the vicinity of the η meson peak. We will try to get rid of this background using the following procedure. We start with a bidimensional histogram (see figure 6.25), the missing mass of two protons versus the invariant mass of e^+e^- for the selected data set. The histograms that are shown in figure 6.27 are projections of 50 MeV/c^2 slices in e^+e^- invariant mass, from 0 to 400 MeV/c^2 on the missing mass axis. For each histogram, we perform a fit using the sum of a simulated $pp \rightarrow pp\pi^+\pi^-\pi^0$ background (to mimic a multiparticle phase space behavior) multiplied by a third order polynomial and a lorentzian function (that describes the $\eta \rightarrow e^+e^-\gamma$ signal). The figure 6.26 presents the global fit to the whole 0 – 400 MeV/c^2 e^+e^- invariant mass range. For each slice in the e^+e^- invariant mass, we extract the signal content i.e. the number of events in the lorentzian function needed to obtain the best agreement with data. The result of this fit together with a Monte Carlo simulation of $\eta \rightarrow e^+e^-\gamma$ signal, is shown in figure 6.28. This procedure removes most of the background with the exception of events from η meson decays.

The distribution of events in figure 6.25 is nonuniform, the number of events strongly decreases with increasing e^+e^- invariant mass. It is therefore natural to apply different binning in different mass ranges. It would also allow to test the fit stability and serve as check for systematical uncertainties. This will be done in section 8.1.2 where we present the results of this procedure applied to the case of the η form factor extraction.

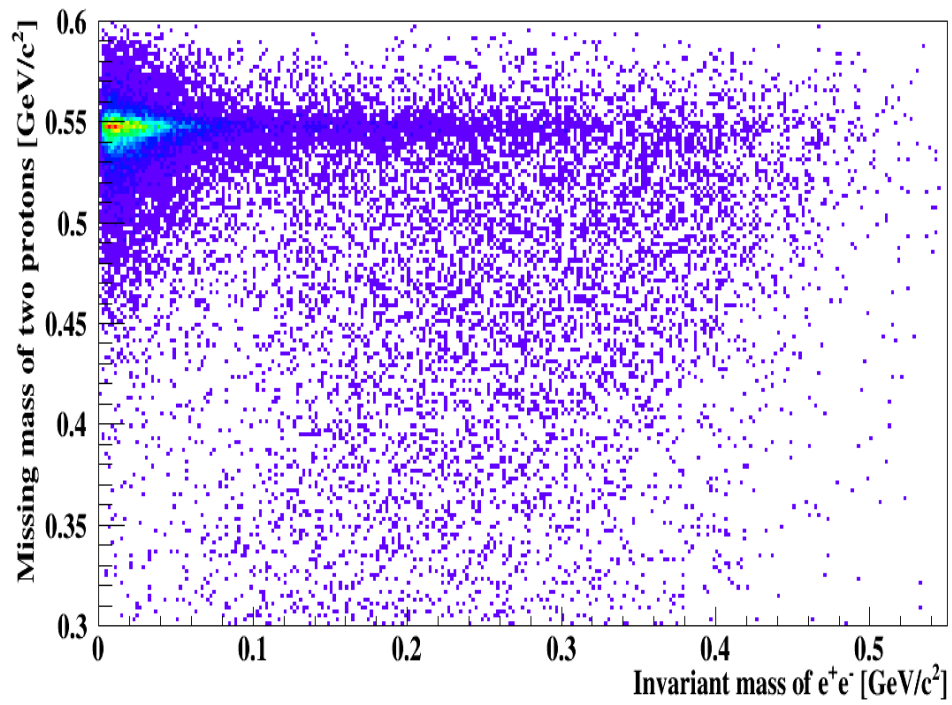
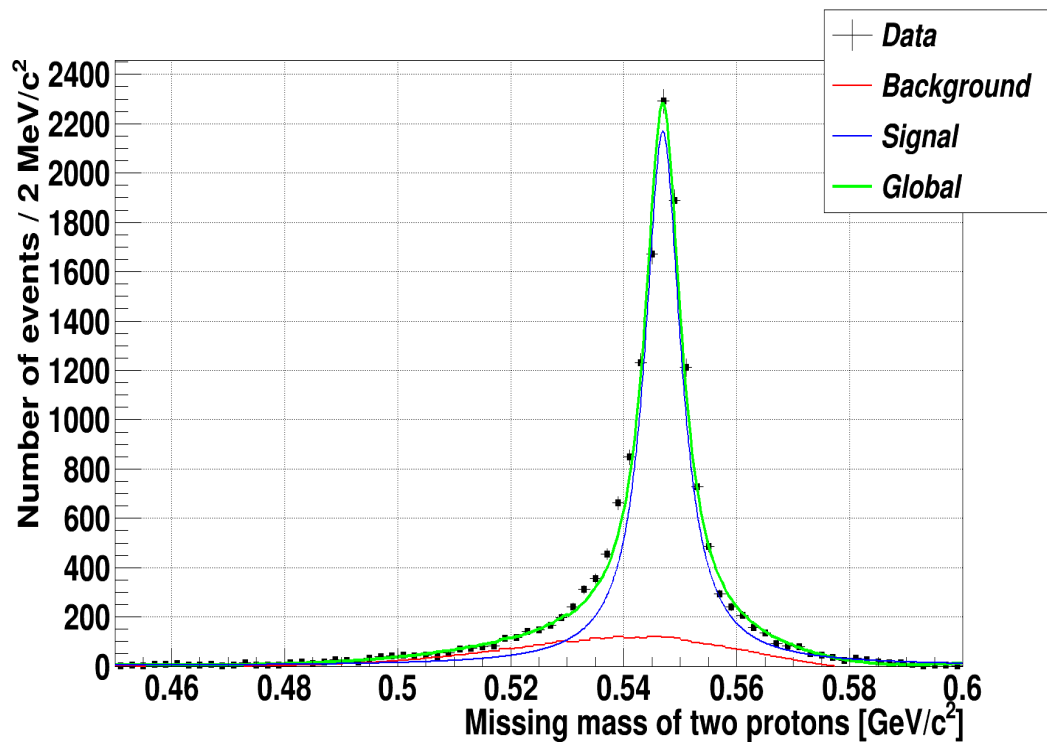
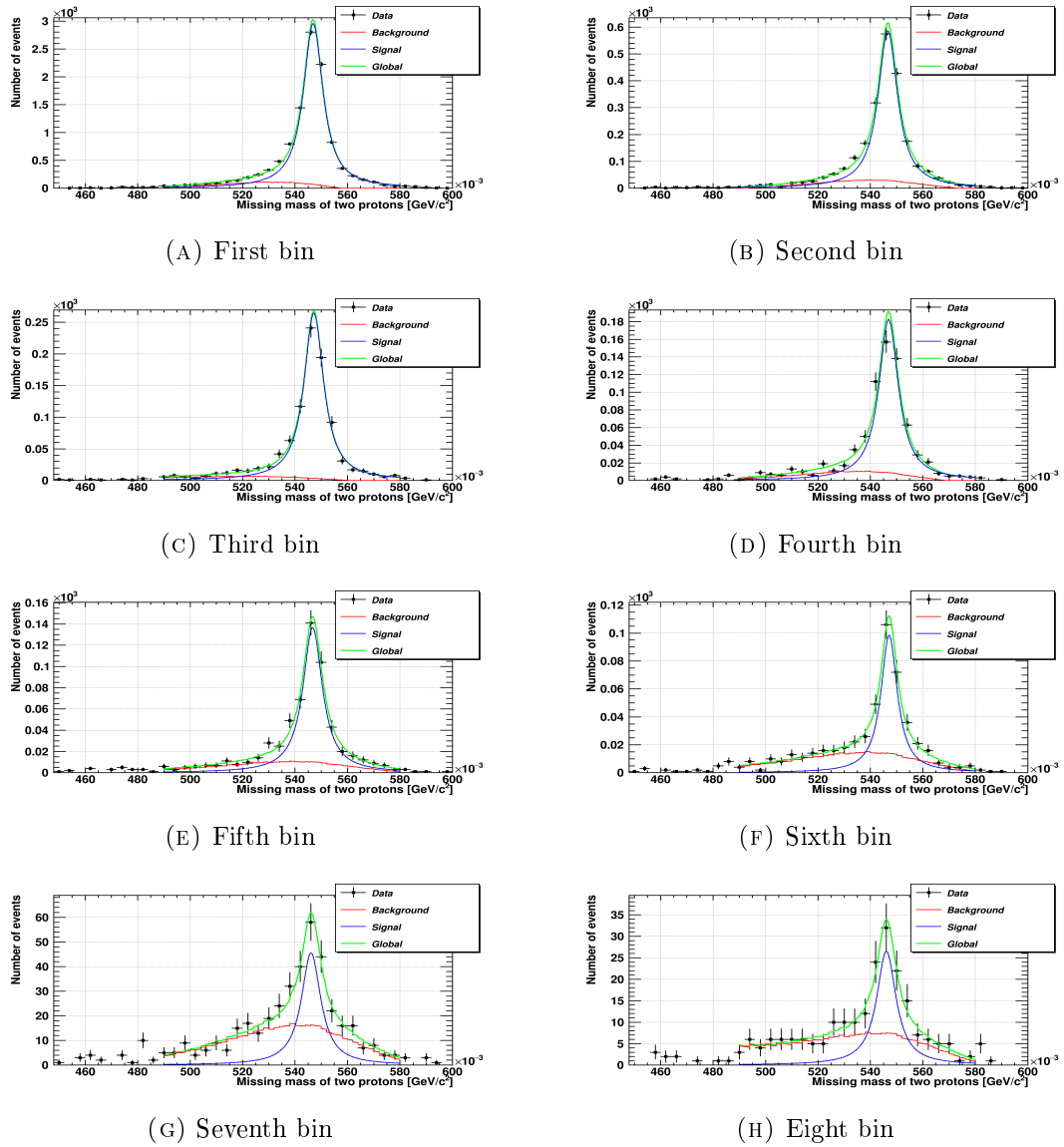
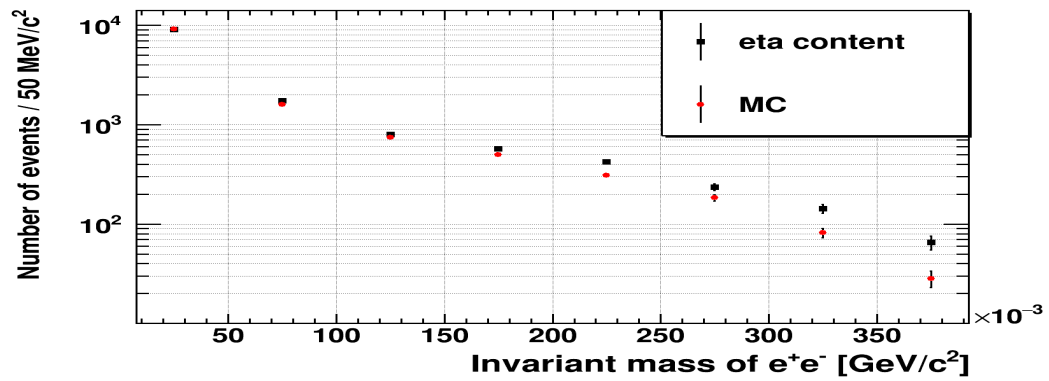
FIGURE 6.25: Missing mass of two protons versus invariant mass of e^+e^- (data).

FIGURE 6.26: Global fit to the missing mass of two protons.

FIGURE 6.27: Fits to eight $50 \text{ MeV}/c^2$ slices in protons missing mass.FIGURE 6.28: Invariant mass of e^+e^- - extracted η content.

6.10 Combinatorial background.

There are two sources of combinatorial background. One of them is the wrong combinations of tracks originating from the same reaction (event) and the other are random coincidences. The first case arises when many e^+e^- pairs are produced in a reaction, for example in the so-called double Dalitz decay $\eta \rightarrow e^+e^-e^+e^-$, or when a pion is misidentified and treated as a lepton (electron or positron). Since the reconstruction algorithm is not perfectly efficient, some of the physical electron tracks are not reconstructed. Sometimes a particle is not detected due to the detector geometry, when, for example, it escapes through the beam tube. The analysis criteria could then lead to the wrong choice of a charged pair. This type of background can, in principle, be assessed directly by simulating the relevant channels.

The second source of combinatorial background, called random (or accidental) coincidences or “pile-ups”, is more difficult to handle. It is due to the overlapping of tracks from different events and reactions¹. The temporal resolution of the data acquisition is finite, therefore we can expect situations where the particles coming from two different reactions are merged into one event. The selection criteria implemented in previous sections reject only a part of the pile-up contribution. The simulation of this background is possible but it would require to generate a Monte Carlo cocktail of all possible reactions weighted by their relative occurrence in the sample. In the next section, we propose a simpler way around allowing us to estimate the distribution of this background.

6.10.1 Estimation of the number of random coincidences

Our estimate of the combinatorial background is based on the following approach. We assume that the main sources of combinatorial background are events with three charged tracks. An example of such event is a $\eta \rightarrow e^+e^-\gamma$ reaction with an additional pion track (f.e. from direct pion production) if the pion is misidentified as an electron. There are two classes of such events:

- class N^{21} with $N_+ = 2$ and $N_- = 1$
- class N^{12} with $N_+ = 1$ and $N_- = 2$

¹For example, the overlapping between $pp \rightarrow pp(\eta \rightarrow e^+e^-\gamma)$ and a large cross section channel like $pp \rightarrow pn\pi^+$.

We neglect events with two charged pairs. This class of events can also contribute to the combinatorial background but with much lower probability². Anyway, four track events are very rare (see figure 6.29).

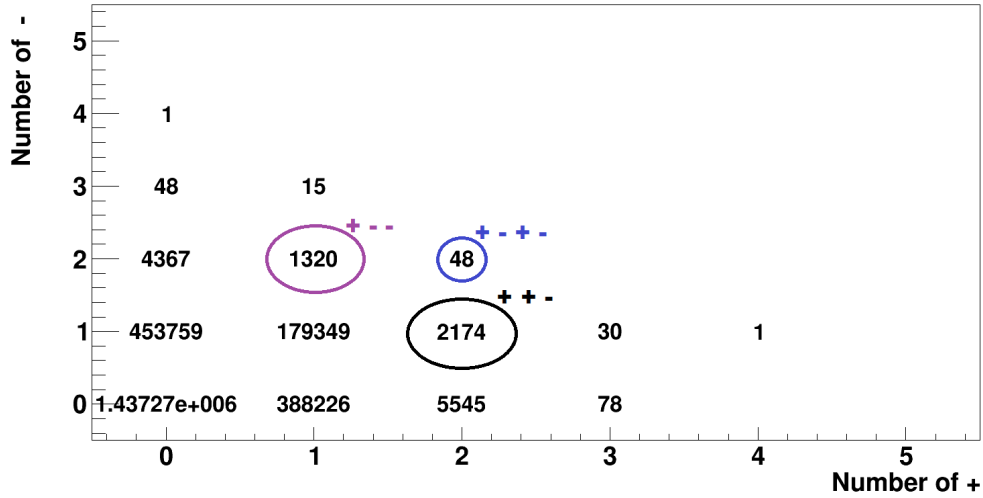


FIGURE 6.29: Charged tracks multiplicity after particle identification.

We know that for one N^{21} class event there is one wrong $+-$ combination, one correct $+-$ pair and one (obviously wrong) $++$ combination. Therefore, $N_{+-}^{21} = N_{++}$ where N_{+-}^{21} represents the number of combinatorial background events from N^{21} subset. Analogically, we have $N_{+-}^{12} = N_{--}$ combinatorial background events from N^{12} class events. Summing up those contributions we estimate the number of combinatorial background events:

$$N_{+-}^{CB} = N_{+-}^{21} + N_{+-}^{12} = N_{++} + N_{--} \quad (6.1)$$

In order to extract N_{++}^{21} and N_{--}^{12} , we process our data sample using our standard selection cuts and require exactly two identically charged particles after identification. We find that $N_{++} = 42$ and $N_{--} = 16$.

This leads us to the estimation of the number of combinatorial background in our sample $N_{+-}^{CB} = 42 + 16 = 58$.

²If the random coincident particles are pions then the PID must fail at least once and at least two correct tracks must be rejected by the selection process.

6.10.2 Invariant mass distribution of random coincidences

The sum of the e^+e^- invariant mass distributions of N_{++} and N_{--} events provides us with the expected distribution of the e^+e^- invariant mass of the combinatorial background. Given the low statistics of those events, we fit a third order polynomial to the binned ($40 \text{ MeV}/c^2$) histogram, then we create a histogram based on the fitted function (see figure 6.30). This smooth histogram will be used further in this work.

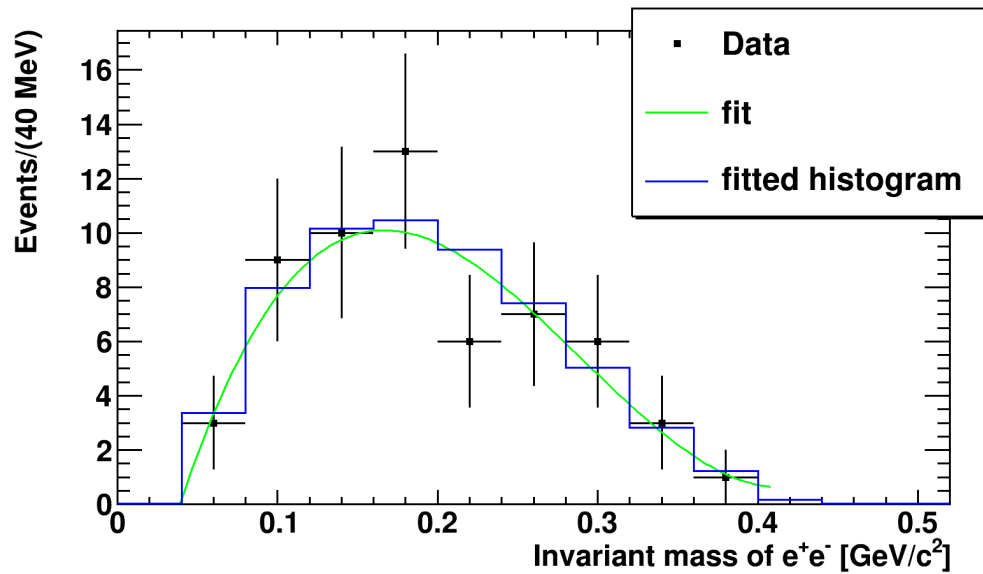


FIGURE 6.30: Invariant mass of e^+e^- distribution for combinatorial background.

Chapter 7

Analysis of $\eta \rightarrow e^+e^-$ channel

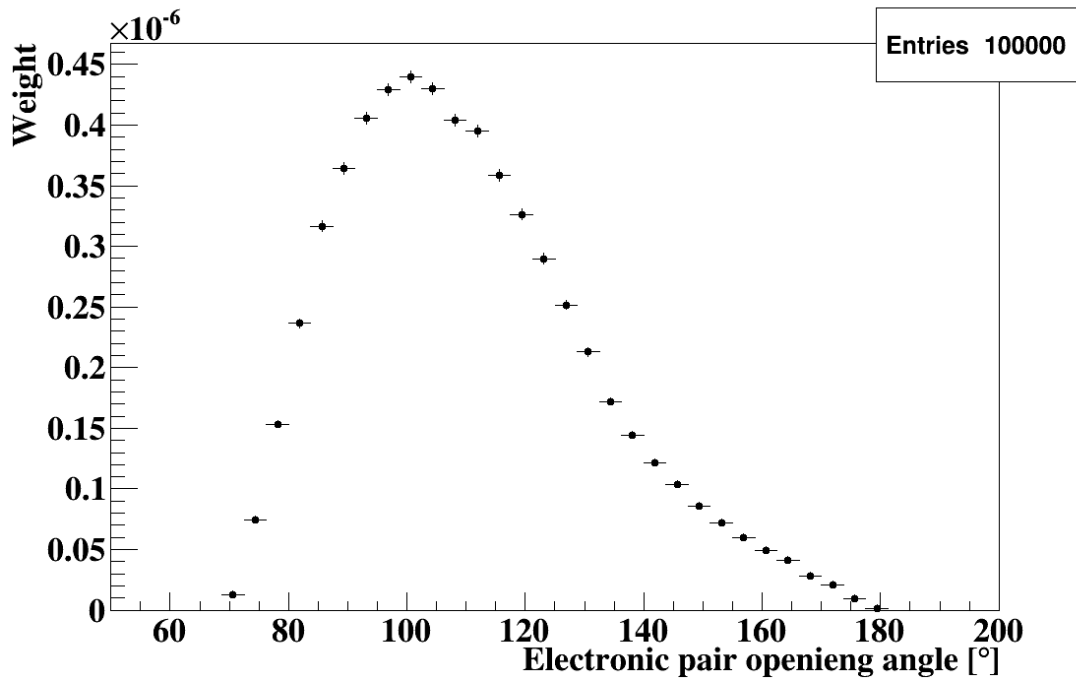
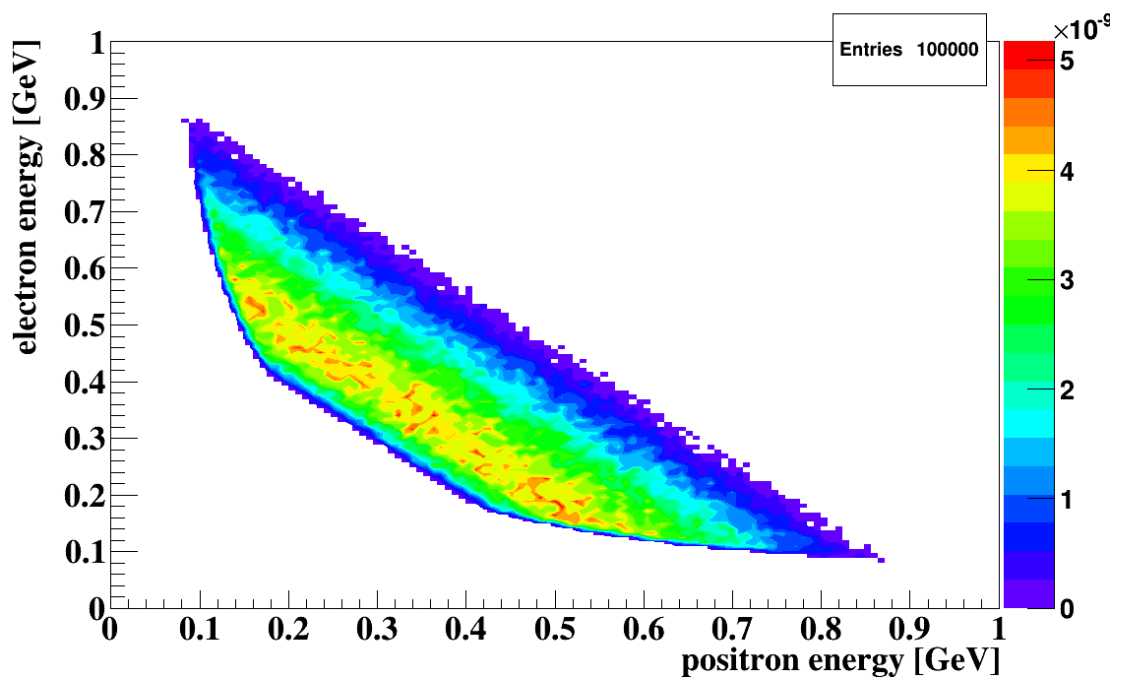
As it was already described in section 1.5.2 the $\eta \rightarrow e^+e^-$ is a very rare two-body decay. A massive η particle disintegrate into an electron-positron pair. This reaction has simple kinematics, especially in the η meson rest frame. The opening angle between e^+e^- in this frame is exactly 180° . It is transformed by the Lorentz boost to the laboratory frame and this effect, neglecting detector and reconstruction smearing, is shown on figure 7.1 for an incident proton kinetic energy of 1.4 GeV. The invariant mass of $\eta \rightarrow e^+e^-$ system is equal to η meson mass, $547 \text{ MeV}/c^2$, and each lepton carries on average 300 MeV that are almost completely deposited in the calorimeter (see figure 7.2). Those characteristics, among many other, are used in order to select $\eta \rightarrow e^+e^-$ candidates from the data sample. They are presented in section 7.1.

7.1 Summary of $\eta \rightarrow e^+e^-$ selection criteria

The analysis of this channel is based on the same 2012 data set as in the case of $\eta \rightarrow e^+e^-\gamma$ reaction. The sample after the data reduction described in section 5.1 is suitable for this analysis as it contains events with two charged tracks in CD without any condition on neutral tracks. The criteria that were used to select the $\eta \rightarrow e^+e^-$ candidates are the following¹:

- special trigger that select events with two clusters with energy deposit above threshold in CD
- exactly two charged tracks in CD and in FD, no neutral CD tracks

¹The missing values are calculated by taking the difference between four-vectors. For example, the missing polar angle of pe^+e^- is the polar angle of the four-vector $\mathbf{P}_{\text{beam}} + \mathbf{P}_{\text{target}} - \mathbf{P}_{\text{p1}} - \mathbf{P}_{\text{p2}} - \mathbf{P}_{\text{e+}} - \mathbf{P}_{\text{e-}}$.

FIGURE 7.1: Angle between e^+e^- pair (laboratory frame): $\eta \rightarrow e^+e^-$ simulationFIGURE 7.2: Energy of e^+ and e^- : $\eta \rightarrow e^+e^-$ simulation

- particle identification such as $0.8 < \left| \frac{\text{momentum}}{\text{energy}} \right| < 1.1$ for each charged track
- sum of energy deposits of the two charged tracks > 550 MeV
- energy deposit for each track > 320 MeV
- angle between electrons in space $> 89^\circ$
- angle between electrons on OXY plane $> 135^\circ$
- $500 \text{ MeV}/c^2 < \text{invariant mass of } e^+e^- < 700 \text{ MeV}/c^2$
- $500 \text{ MeV}/c^2 < \text{missing mass of two protons} < 600 \text{ MeV}/c^2$
- missing polar angle of $ppe^+e^- < 6^\circ$
- missing momentum of $ppe^+e^- > -500 \text{ MeV}/c$
- missing energy of $ppe^+e^- > -200 \text{ MeV}$
- missing mass of $ppe^+e^- > 1750 \text{ MeV}/c^2$
- mean time of protons - time of each electron < 10 ns
- mean time of protons - mean time of electrons < 8 ns
- η emission polar angle $\theta_{ee} < 30^\circ$

Those selection conditions are based on the work of dr. Marcin Berłowski described in his PhD thesis [66]. The purpose of this new analysis consists of several interesting aspects:

- we use a larger data set from another period (2012)
- we include the whole range of θ angles by using all calorimeter modules (forward, central and backward)
- we use a different trigger - at least two clusters above threshold (≈ 100 MeV) in CD for each track
- we broaden the condition on the time difference between tracks in FD and charged tracks in CD from 10 ns to 20 ns
- we use a different particle identification (graphical cut)

7.2 Selection of $\eta \rightarrow e^+e^-$ event candidates

There are several sources of background to $\eta \rightarrow e^+e^-$ reaction. We will focus on two reactions that have the most important contribution to this background due to their high cross section and/or the difficulty to disentangle their final state from our signal. Those channels are $pp \rightarrow pp\pi^+\pi^-$ and $\eta \rightarrow e^+e^-\gamma$.

7.2.1 $pp \rightarrow pp\pi^+\pi^-$ background

The importance of this channel is due to its large cross-section (~ 0.6 mb) with respect to η production ($\sim 10 \mu\text{b}$) coupled with the same final state - two charged particles in CD. This channel has no peak in the η mass region but rather contributes to the continuous background. In order to get rid of it we also exploit the fact that while most of the electrons stop in the electromagnetic calorimeter thus leaving all their energy inside (via electromagnetic showers), the pions pass through the SEC and leave only a part of their energy².

7.2.2 $\eta \rightarrow e^+e^-\gamma$ background

Although most of the e^+e^- pairs from this reaction have low invariant masses, we need to consider the case when the virtual photon takes most of the decay energy, leading to large e^+e^- masses. Then, the real photon has low energy and can easily go undetected due to the threshold values of the detector elements. In this case, the final state is the same as in $\eta \rightarrow e^+e^-$ and the kinematics are very similar.

7.2.3 Baryonic resonance background

The main background from baryonic resonances could originate from $pp \rightarrow p\Delta^+ (\rightarrow pe^+e^-)$ channel. However, the cross section for Δ^+ production is of the order of 1 mb while $BR(\Delta^+ \rightarrow pe^+e^-) = 4 \cdot 10^{-5}$ we can neglect this channel in comparison to $\eta \rightarrow e^+e^-\gamma$. We generated 10^6 Monte Carlo events with PLUTO and obtained zero remaining events after all selection.

²With the exception of those pions that decay inside the detector or undergo nuclear interactions.

7.2.4 Combinatorial background

Using the same approach as described in section 6.10 we find $N_{++} = 11$ and $N_{--} = 5$. Therefore we estimate the combinatorial background contribution to be of the order of 16 events.

7.2.5 Data selection

Figures 7.3a, 7.3b, 7.4a, 7.4b, 7.5a and 7.5b illustrate some of the selection criteria presented in 7.1 by comparing data with the Monte Carlo simulation of the signal reaction $\eta \rightarrow e^+e^-$:

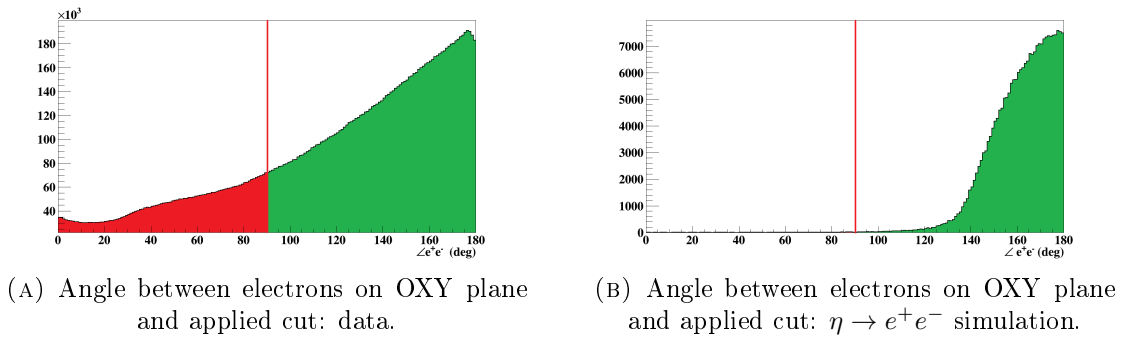


FIGURE 7.3: Illustration of angular condition applied for data and $\eta \rightarrow e^+e^-$ simulation.

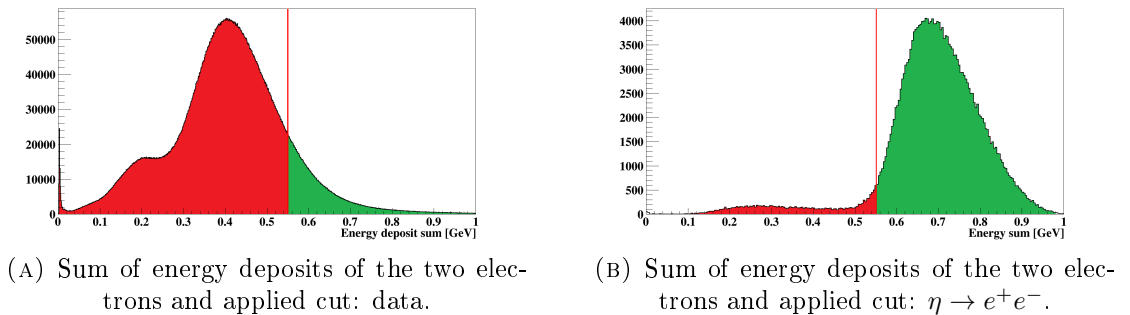


FIGURE 7.4: Illustration of energy condition applied for data and $\eta \rightarrow e^+e^-$ simulation.

7.3 Summary of $\eta \rightarrow e^+e^-$ selection

Table 7.1 shows the simulated acceptances and expected number of events for different channels.

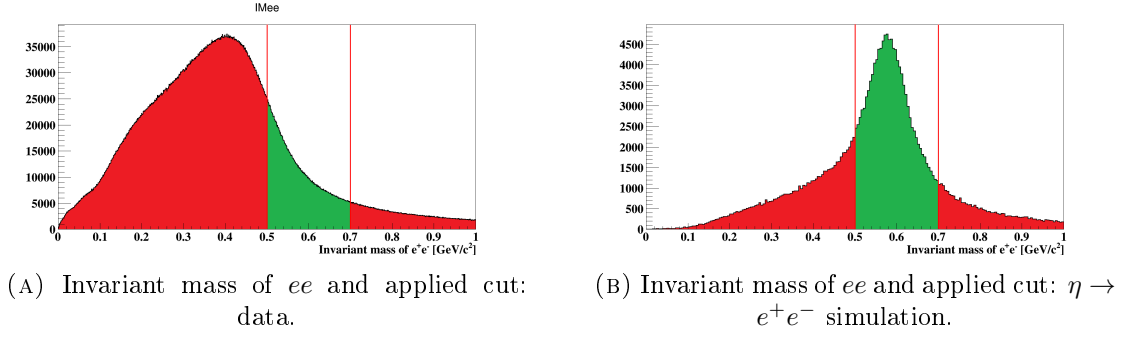


FIGURE 7.5: Illustration of invariant mass condition applied for data and $\eta \rightarrow e^+e^-$ simulation.

TABLE 7.1: $\eta \rightarrow e^+e^-$ and background reactions

Reaction	N_{sim}	final selection	$N_{expected}$
$\eta \rightarrow e^+e^-$	$8.4 \cdot 10^5$	$2.1 \cdot 10^3$	-
$\eta \rightarrow e^+e^-\gamma$	$5 \cdot 10^6$	1 (4.36) 90% C.L.	~ 1
$pp \rightarrow pp\pi^+\pi^-$	$1.4 \cdot 10^7$	0 (2.44) 90% C.L.	~ 680
$pp \rightarrow pp\pi^+\pi^-$ [66]	10^7	-	$\sim 156^{+248}_{-27}$
combinatorial background	-	-	~ 16

The ratio between $\sigma(pp \rightarrow pp\pi^+\pi^-)$ and $pp \rightarrow pp\eta$ at 1.4 GeV is around $\frac{600 \mu b}{10 \mu b} = 60$. The number of expected $pp \rightarrow pp\pi^+\pi^-$ events 680 is, in fact, and upper limit due to the limited statistics of the simulation, e.g. if we generated 10 times more $pp \rightarrow pp\pi^+\pi^-$ events and obtained zero events after selection, the number of expected events would be 68.

The $pp \rightarrow pp\pi^+\pi^-$ simulation in [66] was performed in such a way that $IM_{\pi^+\pi^-} = M_\eta$, therefore we consider the resulting number of expected $pp \rightarrow pp\pi^+\pi^-$ events to be a better estimate for this background channel.

Chapter 8

Results and Discussion

8.1 Determination of the transition form factor.

We have seen in section 1.4.1 that the transition form factor can be extracted by comparing (dividing) the experimental spectrum of e^+e^- invariant mass from $\eta \rightarrow e^+e^-\gamma$ decay with its theoretical pure QED contribution. First, we need to select a clean sample of $\eta \rightarrow e^+e^-\gamma$ events. In this work, we have used two different approaches.

8.1.1 Background subtraction using $\eta \rightarrow e^+e^-\gamma$ selection cuts.

The data sample we use here is produced by directly applying a set of criteria to the initial data. Those are described in the sections 5.1, 6.1, 6.2, 6.3, 6.4, and 6.6.

The final distribution is obtained by subtracting the subsisting background channels $\eta \rightarrow \gamma\gamma$ and $pp \rightarrow pp\pi^0 (\rightarrow \gamma\gamma) \pi^0 (\rightarrow e^+e^-\gamma)$. In order to extract the transition form factor, we divide the resulting data spectra by the simulated pure QED $\eta \rightarrow e^+e^-\gamma$ decay. As input we use three sets of data and simulations resulting from a modification of the missing mass condition:

- Sample A: missing mass of two protons in [520, 580] MeV/c² range
- Sample B: missing mass of two protons in [530, 570] MeV/c² range
- Sample C: missing mass of two protons in [535, 565] MeV/c² range

The resulting histograms are represented in figures 8.1, 8.2, 8.3, 8.5, 8.6 and 8.7 using the combinatorial background contribution consistent with the analysis described in section 6.10 (58 events). We show those plots for two different bin widths, 20 MeV/c² and 40 MeV/c². The fit function used is the square of the slightly transformed equation 1.9:

$$[F(q^2)]^2 = \left(\frac{1}{1 - \frac{q^2}{\Lambda^2}} \right)^2 = \left(\frac{1}{1 - b_\eta \cdot q^2} \right)^2 \quad (8.1)$$

with the fit parameter $b_\eta = \Lambda^{-2}$.

The table 8.1 presents the results of different fits.

TABLE 8.1: Results of the form factor fits

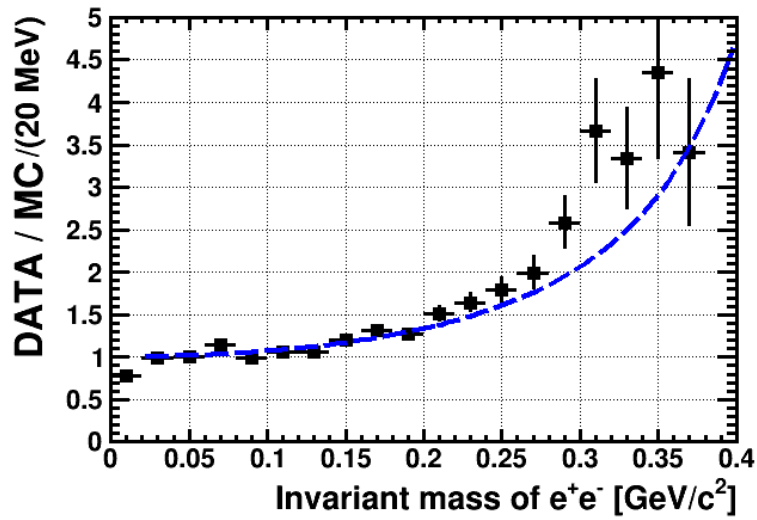
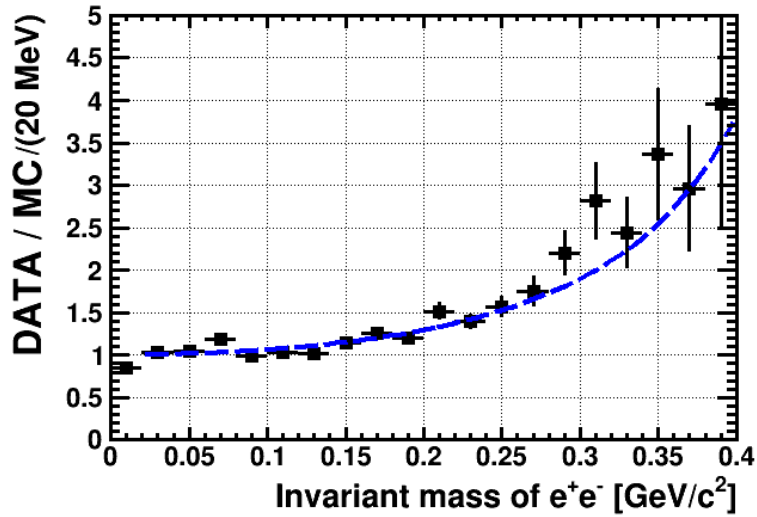
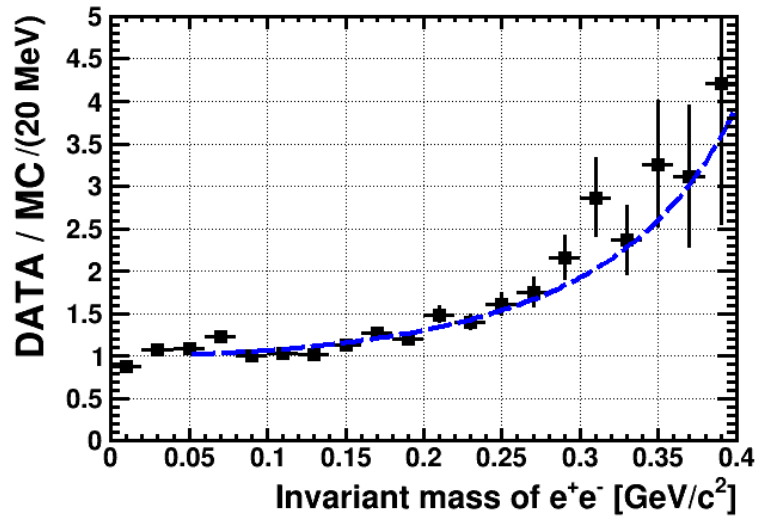
Sample	Bin width	CB events	Λ^{-2} [GeV ⁻²]	χ^2/ndf
Sample A	20 MeV/c ²	58	3.38 ± 0.12	1.9
		280	2.89 ± 0.21	1.1
	40 MeV/c ²	58	3.54 ± 0.12	2.3
		280	3.10 ± 0.21	1.5
Sample B	20 MeV/c ²	58	3.05 ± 0.15	1.3
		280	2.29 ± 0.28	1.1
	40 MeV/c ²	58	3.18 ± 0.14	1.4
		280	2.44 ± 0.29	1.7
Sample C	20 MeV/c ²	58	3.01 ± 0.15	1.4
		280	2.14 ± 0.31	1.3
	40 MeV/c ²	58	3.13 ± 0.15	1.7
		280	2.27 ± 0.31	2.2

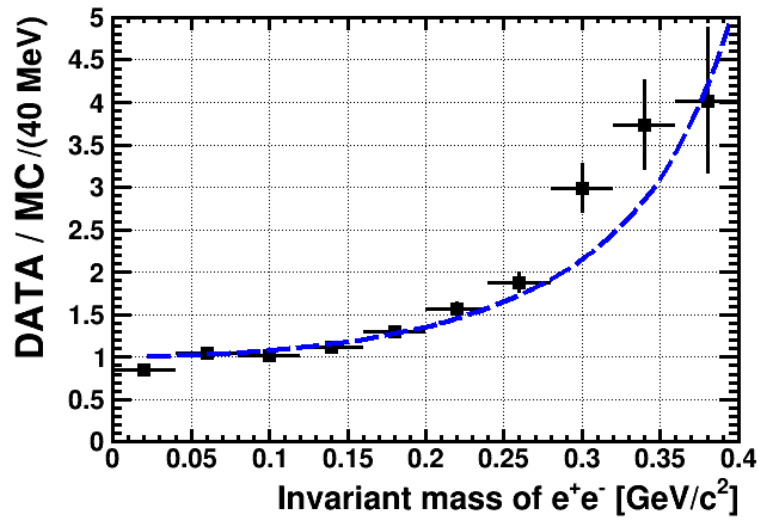
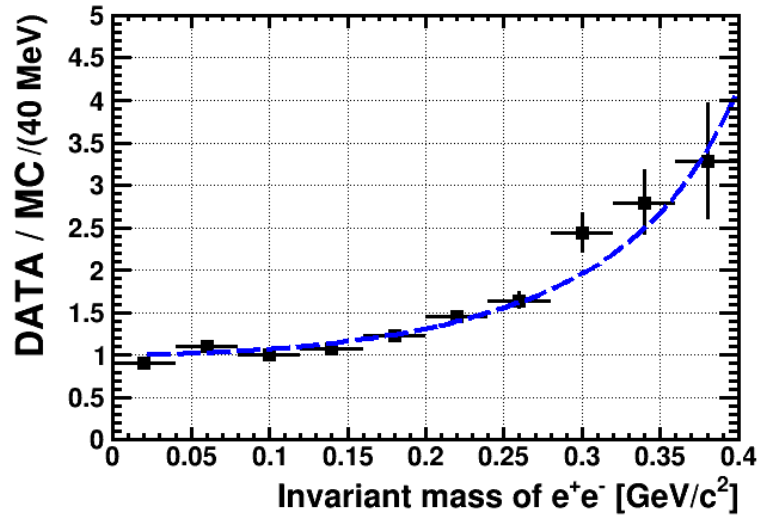
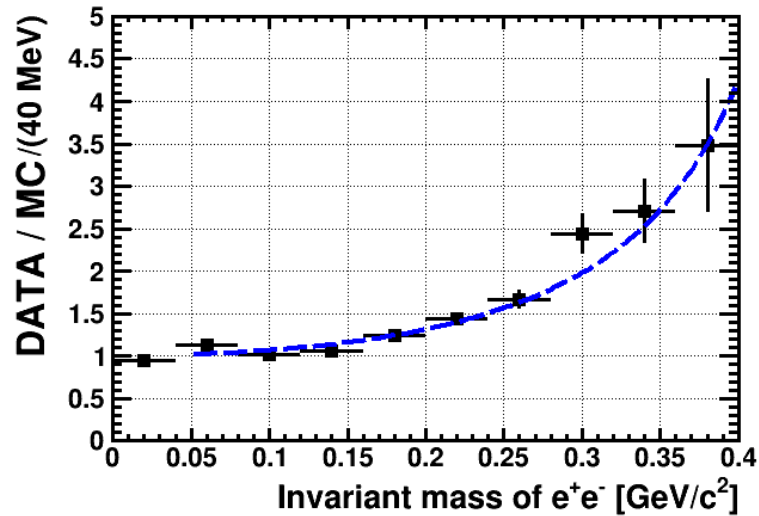
The uncertainties that appear in the table 8.1 are of statistical nature. In order to estimate the systematic uncertainty we choose a reference value for Λ^{-2} . In our case, it will be the measurement with the lowest χ^2/ndf value and 15 pileup events (3.05 ± 0.15) GeV⁻². The systematic uncertainty is then calculated using the following formula:

$$\sigma_{sys} = \frac{1}{N} \sqrt{\sum_i (x_{ref} - x_i)^2} \quad (8.2)$$

where x_{ref} is the reference value and x_i the N measurements. Equation 8.2 leads to the following result: $\Lambda^{-2} = (3.05 \pm 0.15_{stat} \pm 0.15_{sys})$ GeV⁻².

We see that we have a systematic discrepancy for masses above 280 MeV/c² which is more pronounced for sample A (less strict missing mass of two protons cut). This could be explained by the presence of non- η background events with high invariant masses that were not rejected by selection criteria of our analysis. An attempt to solve this problem was described in section 6.9 and its results are presented in section 8.1.2.

FIGURE 8.1: Direct form factor determination (20 MeV/c² bin width): Sample A.FIGURE 8.2: Direct form factor determination (20 MeV/c² bin width): Sample B.FIGURE 8.3: Direct form factor determination (20 MeV/c² bin width): Sample C.FIGURE 8.4: Transition form factor fits for 20 MeV/c² bin width (standard combinatorial background).

FIGURE 8.5: Direct form factor determination ($40 \text{ MeV}/c^2$ bin width): Sample A.FIGURE 8.6: Direct form factor determination ($40 \text{ MeV}/c^2$ bin width): Sample B.FIGURE 8.7: Direct form factor determination ($40 \text{ MeV}/c^2$ bin width): Sample C.FIGURE 8.8: Transition form factor fits for $40 \text{ MeV}/c^2$ bin width (standard combinatorial background).

8.1.2 Background subtraction using the fit to two proton missing mass distribution.

The procedure used here was described in section 6.9. We use the same data selection that in section 8.1.1 and remove the non- η background by a fitting procedure on the proton missing mass. As a result we get a distribution of e^+e^- invariant mass. In order to extract the form factor, we need to divide this distribution by the $\eta \rightarrow e^+e^-\gamma$ simulation with the form factor equal to 1. Then, analogously to section 8.1.1 we fit the obtained data points to extract the transition form factor. As an example, the result for a uniform 50 MeV/ c^2 binning, is presented in figure 8.9:

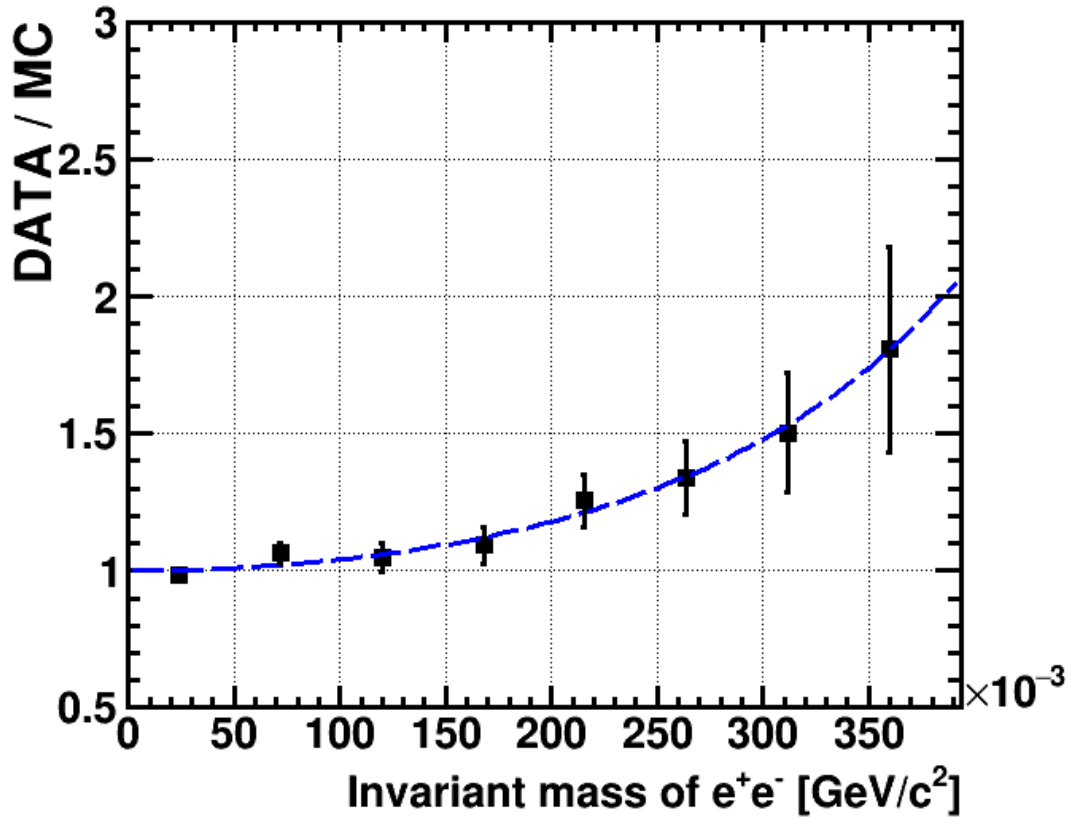


FIGURE 8.9: Form factor resulting from fit based background subtraction.

This fit leads to the form factor parameter value of $\Lambda^{-2} = (1.97 \pm 0.29) \text{ GeV}^{-2}$ while the fit $\chi^2 = 0.48$. We treat this measurement as our reference value. As announced in section 6.9, we will perform some systematical checks by varying numerous parameters that influence the fitting.

First, we change the bin width, independently in the $0 - 100 \text{ MeV}/c^2$ and in the $100 - 400 \text{ MeV}/c^2$ e^+e^- invariant mass range. For example, we change the bin width in the $0 - 100 \text{ MeV}/c^2$ mass range to $25 \text{ MeV}/c^2$, such plot is shown in figure 8.10.

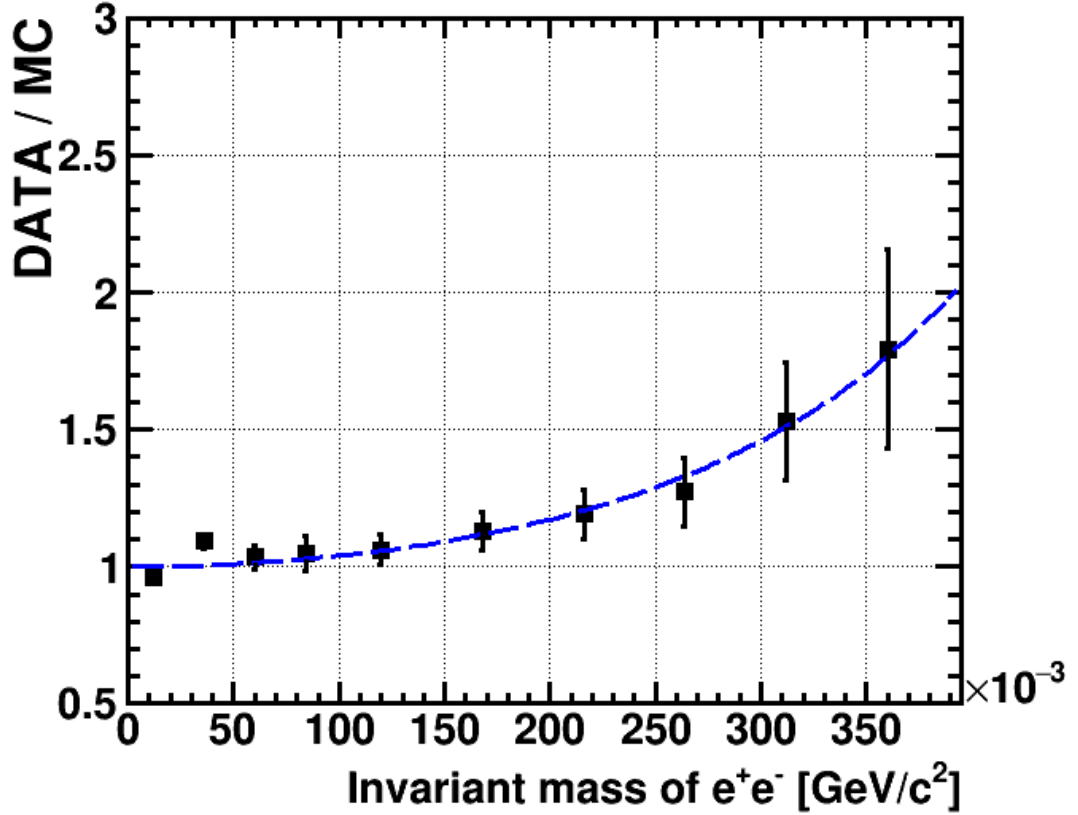


FIGURE 8.10: Form factor fit based background subtraction (bin width modified for $0 - 100 \text{ MeV}/c^2$).

This fit $\chi^2 = 1.36$ and the form factor parameter is $\Lambda^{-2} = (1.91 \pm 0.29) \text{ GeV}^{-2}$. In this highly populated low mass region the fit is rather stable, the main issue is to check the stability of the large mass region (above $100 \text{ MeV}/c^2$). The fit and consequently the form factor value depends mostly of the behavior of the fit function for large masses where the statistic is low. It is therefore important to check the fit stability for $\text{IM}_{ee} > 100 \text{ MeV}/c^2$. The figure 8.11 shows the fit for a $30 \text{ MeV}/c^2$ bin width.

Here, the form factor parameter is $\Lambda^{-2} = (1.97 \pm 0.30) \text{ GeV}^{-2}$ while the fit $\chi^2 = 1.15$.

The table 8.2 summarizes the results of form factor fits for different sets of parameters. The first column indicates the data sample. The sample C was already used in section 8.1.1 while the sample D has more stringent time cuts (see also section 6.2 and figures 6.8a and 6.8b). Here t_{FD} is the mean time of two protons chosen in the Forward

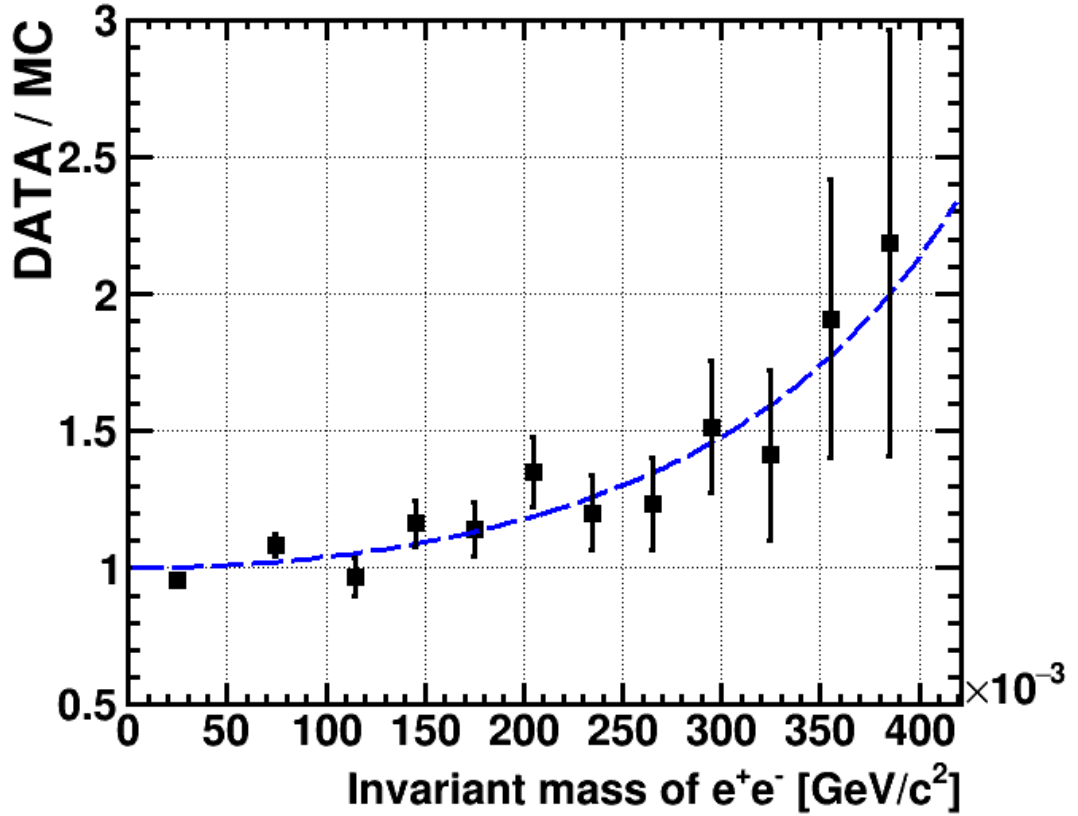


FIGURE 8.11: Form factor fit based background subtraction (bin width modified for 100 – 400 MeV/c^2).

Detector while t_{CDC} and t_{CDN} , are the times of, respectively, charged and neutral tracks in the CD.

Sample C:

- $-16 \text{ ns} < t_{CDC} - t_{FD} < -6 \text{ ns}$
- $-21 \text{ ns} < t_{CDN} - t_{FD} < 5 \text{ ns}$

Sample D:

- $-14 \text{ ns} < t_{CDC} - t_{FD} < -4 \text{ ns}$
- $-19 \text{ ns} < t_{CDN} - t_{FD} < 3 \text{ ns}$

The second column contains the bin width used for the fitting of the signal content. The third column describes the range of the signal content fit. The fourth column stipulates

the bin width used for the form factor fit in the 100-400 MeV/c² range¹. The last two columns contain the Λ^{-2} value and the associated χ^2 .

TABLE 8.2: Results of the form factor fits

Sample	MM2P fit bin	MM2P fit range	FF fit bin	Λ^{-2} [GeV ⁻²]	χ^2/ndf
Sample C	2 MeV/c ²	480-580 MeV/c ²	100 MeV/c ²	1.88 ± 0.28	0.3
			60 MeV/c ²	2.21 ± 0.29	1.2
			50 MeV/c ²	2.50 ± 0.28	1.9
		420-580 MeV/c ²	100 MeV/c ²	1.89 ± 0.28	0.2
	60 MeV/c ²		2.13 ± 0.31	2.3	
	50 MeV/c ²		2.03 ± 0.30	3.3	
	4 MeV/c ²		480-580 MeV/c ²	100 MeV/c ²	1.75 ± 0.29
		60 MeV/c ²		1.77 ± 0.30	0.5
50 MeV/c ²		1.82 ± 0.31		0.4	
420-580 MeV/c ²		100 MeV/c ²	1.89 ± 0.28	0.2	
	60 MeV/c ²	1.77 ± 0.31	0.6		
	50 MeV/c ²	1.85 ± 0.31	0.3		
	Sample D	2 MeV/c ²	480-580 MeV/c ²	100 MeV/c ²	1.66 ± 0.30
60 MeV/c ²				1.78 ± 0.33	2.3
50 MeV/c ²				2.14 ± 0.31	2.6
420-580 MeV/c ²			100 MeV/c ²	1.93 ± 0.29	0.6
			60 MeV/c ²	2.00 ± 0.32	2.1
			50 MeV/c ²	2.11 ± 0.32	1.9
4 MeV/c ²		480-580 MeV/c ²	100 MeV/c ²	1.87 ± 0.29	0.7
			60 MeV/c ²	1.82 ± 0.31	0.9
			50 MeV/c ²	1.86 ± 0.32	1.0
		420-580 MeV/c ²	100 MeV/c ²	1.81 ± 0.28	0.2
			60 MeV/c ²	1.89 ± 0.30	0.4
			50 MeV/c ²	1.94 ± 0.30	0.5

We take the mean of all results with $\chi^2/ndf \leq 2.706$ - it corresponds to a 90% confidence level. We then calculate the systematic uncertainty in the same way we did in section 8.1.1. The result is $\Lambda^{-2} = (1.92 \pm 0.30_{\text{stat}} \pm 0.18_{\text{sys}}) \text{ GeV}^{-2}$.

Finally, taking into account a systematic uncertainty interval of [1.74; 2.1] our reference value becomes:

$$\boxed{1.97 \pm 0.29_{\text{stat}} \begin{matrix} +0.13_{\text{sys}} \\ -0.23_{\text{sys}} \end{matrix}} \quad (8.3)$$

The figure 8.12 shows this result in comparison to CB/TABS (see reference [26]) as well as to the vector meson dominance model and the pure QED (point-like) approach.

¹The bin width value for the 0-100 MeV/c² range is set to 100 MeV/c² (only one bin) for it has low influence on the form factor fit.

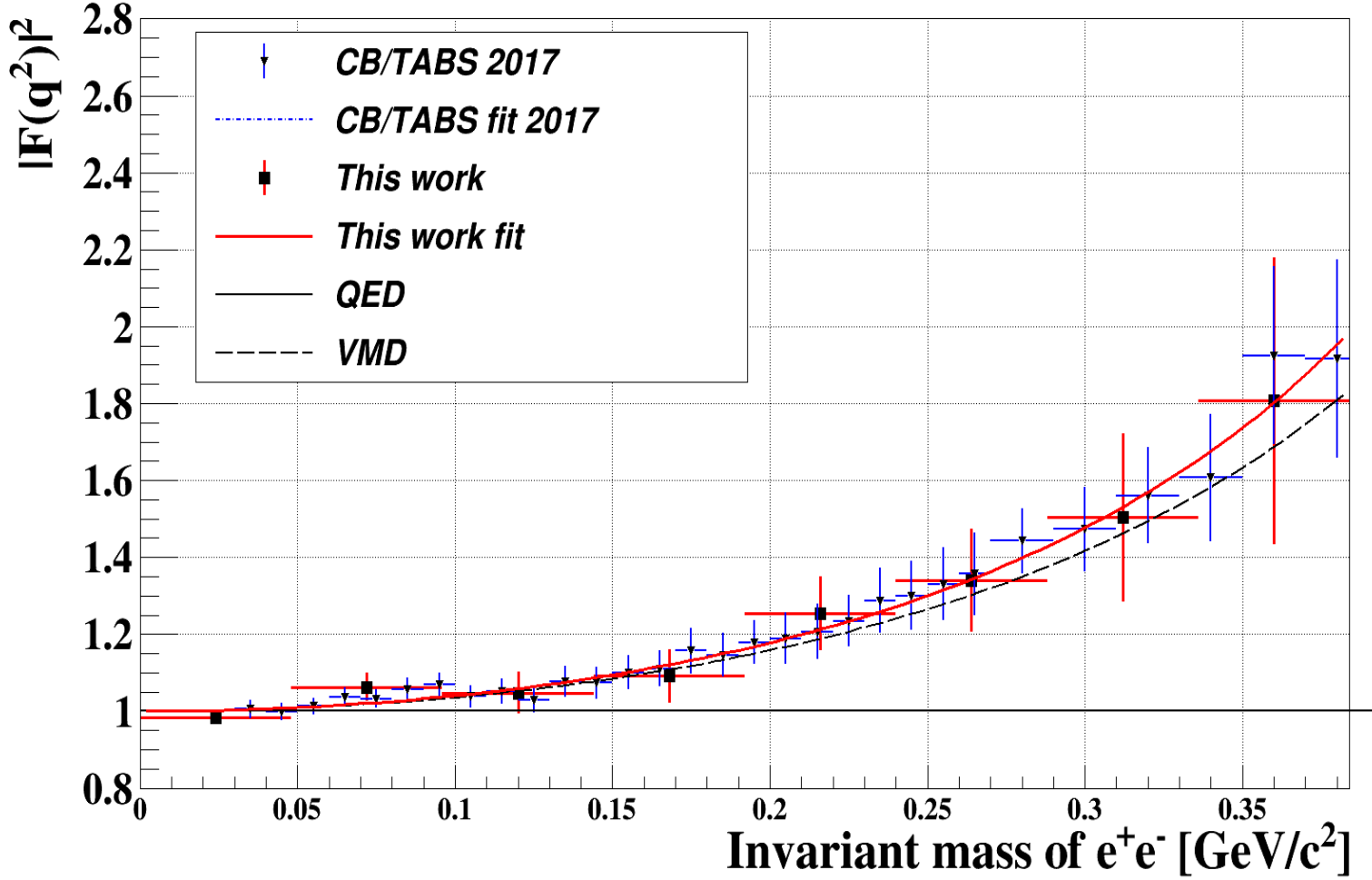


FIGURE 8.12: Form factor comparison between this work and other measurements.

Table 8.3 summarizes the results from different experiments and basic information about those.

TABLE 8.3: FF fits from various experiments

Experiment	Source of η	$\eta \rightarrow e^+e^-\gamma$ candidates	Λ^{-2} [GeV^{-2}]
CB/TABS	$\gamma p \rightarrow \eta p$	$5.4 \cdot 10^4$	$(1.97 \pm 0.11_{\text{tot}})$
WASA [67]	$pd \rightarrow {}^3\text{He}\eta$	$5.2 \cdot 10^2$	$(2.27 \pm 0.73_{\text{stat}} \pm 0.46_{\text{sys}})$
WASA [68]	$pp \rightarrow pp\eta$	$3.1 \cdot 10^3$	$(1.9 \pm 0.33_{\text{stat}})$
WASA this work	$pp \rightarrow pp\eta$	$1.1 \cdot 10^4$	$1.97 \pm 0.29_{\text{stat}} \begin{smallmatrix} +0.13_{\text{sys}} \\ -0.23_{\text{sys}} \end{smallmatrix}$

8.2 Constraint on the $U - \gamma$ coupling.

As it was already mentioned in section 1.4.3, the signature of a hypothetical massive dark boson decaying into e^+e^- pair could be observed as an initially narrow peak, smeared by detector resolution and reconstruction features, superimposed on the usual Dalitz distribution of e^+e^- invariant mass spectrum. The first step consisted in selecting $\eta \rightarrow e^+e^- \gamma$ events candidates using criteria that were presented and discussed in chapter 6. The figure 8.13 shows the final e^+e^- spectrum for data, Monte Carlo simulations of the three main background channels - $\eta \rightarrow \gamma\gamma$, $pp \rightarrow pp\pi^0\pi^0$ with one Dalitz decay, pileups - as well as the sum of those. On figure 8.14 one can observe the difference between data and all backgrounds. We do not observe any statistically significant peak and therefore we can set an upper limit on the branching ratio for an hypothetical $\eta \rightarrow U\gamma$ decay, directly related to the $U - \gamma$ coupling strength parameter ϵ .

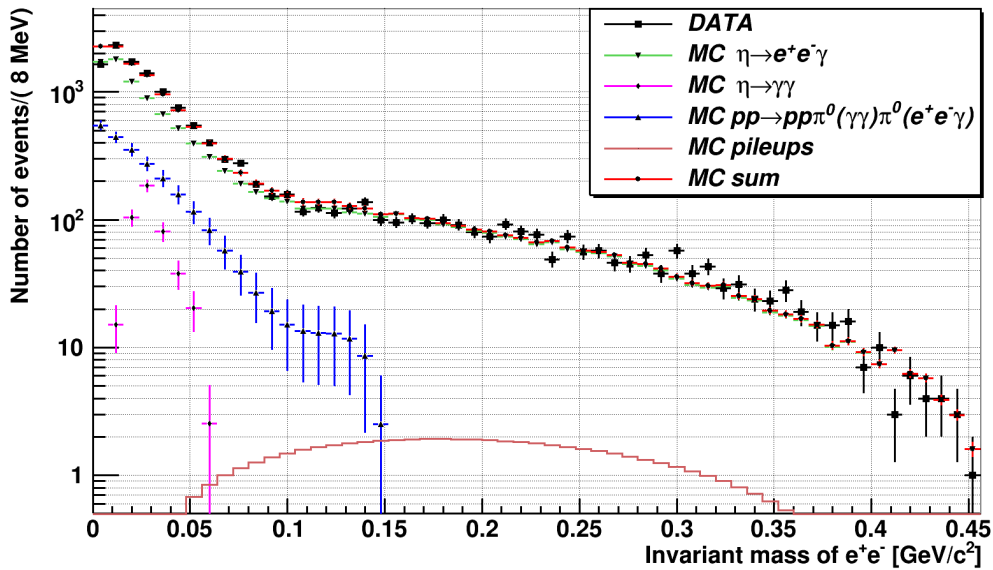


FIGURE 8.13: Invariant mass of e^+e^- - data and background simulations.

In order to extract this limit we follow a similar approach to [16]. For a given value of the U boson mass corresponding to the k^{th} true invariant mass bin, the number of events in the i^{th} bin of reconstructed invariant mass of e^+e^- can be expressed by:

$$N_i/N_{tot} = \frac{1}{\Gamma^b} \sum_j S_{ij} \eta_j^b \nu_j^b + S_{ik} \eta_k \beta \quad (8.4)$$

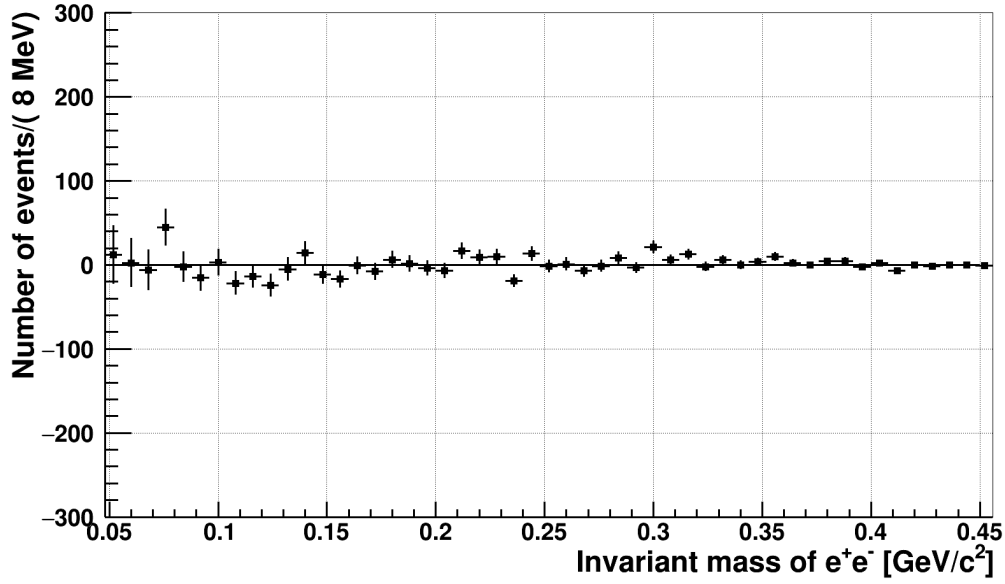


FIGURE 8.14: Invariant mass of e^+e^- - difference between data and sum of background Monte Carlo simulations.

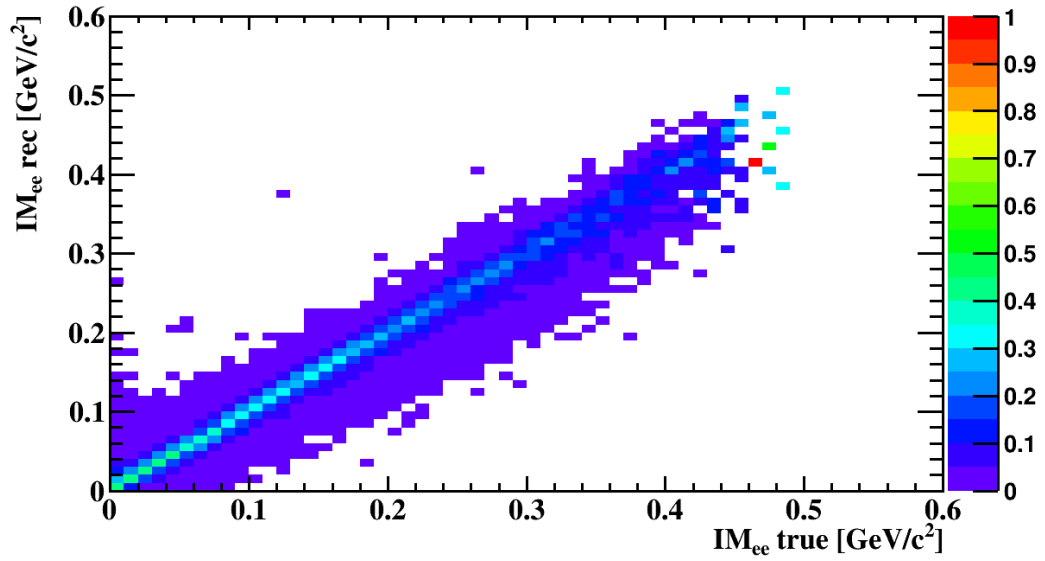
The j and k indices correspond to the true, unperturbed mass distribution while i represents the reconstructed mass distribution. The experimental smearing² is characterized by the S_{ik} matrix (normalized such that $\sum_k S_{ik} = 1$, see figure 8.15a), the content of each true k mass contributes to a range of i reconstructed mass bins. The effect of the selection criteria is described by the acceptance function η_k presented on figure 8.15b. The first term on the right side of equation 8.4 describes the contribution of $\eta \rightarrow e^+e^-\gamma$ and background channels (sum over b) while the second term corresponds to the hypothetical $\eta \rightarrow U\gamma$ channel and a subsequent $U \rightarrow e^+e^-$ decay. N_{tot} is the number of η mesons produced and effectively detected. In this formalism, the parameter β represents the branching ratio of the $\eta \rightarrow U\gamma$ channel.

We can write the equation 8.4 in a simplified form:

$$N_i = \sum_b N_i^b + n_i^k \beta \quad (8.5)$$

where $n_i^k = N_{tot} S_{ik} \eta_k$ represents the reconstruction effect for a given M_U . The corresponding histograms for different values of M_U are shown in figure 8.16.

²The smearing is due to the finite detector resolution and to uncertainties and approximations of the measurement of parameters that are needed to compute the invariant mass of ee .



(A) The smearing matrix.

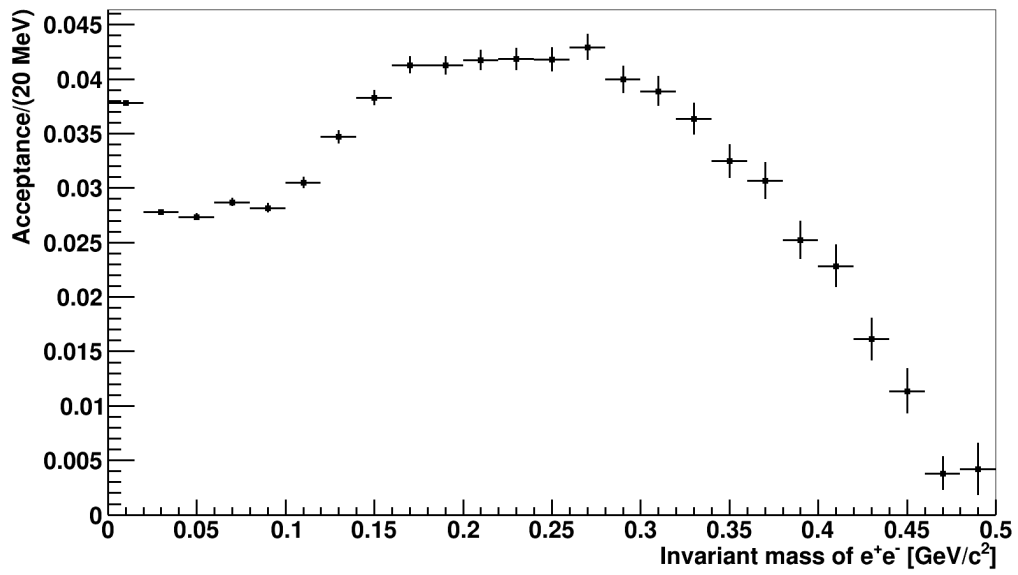
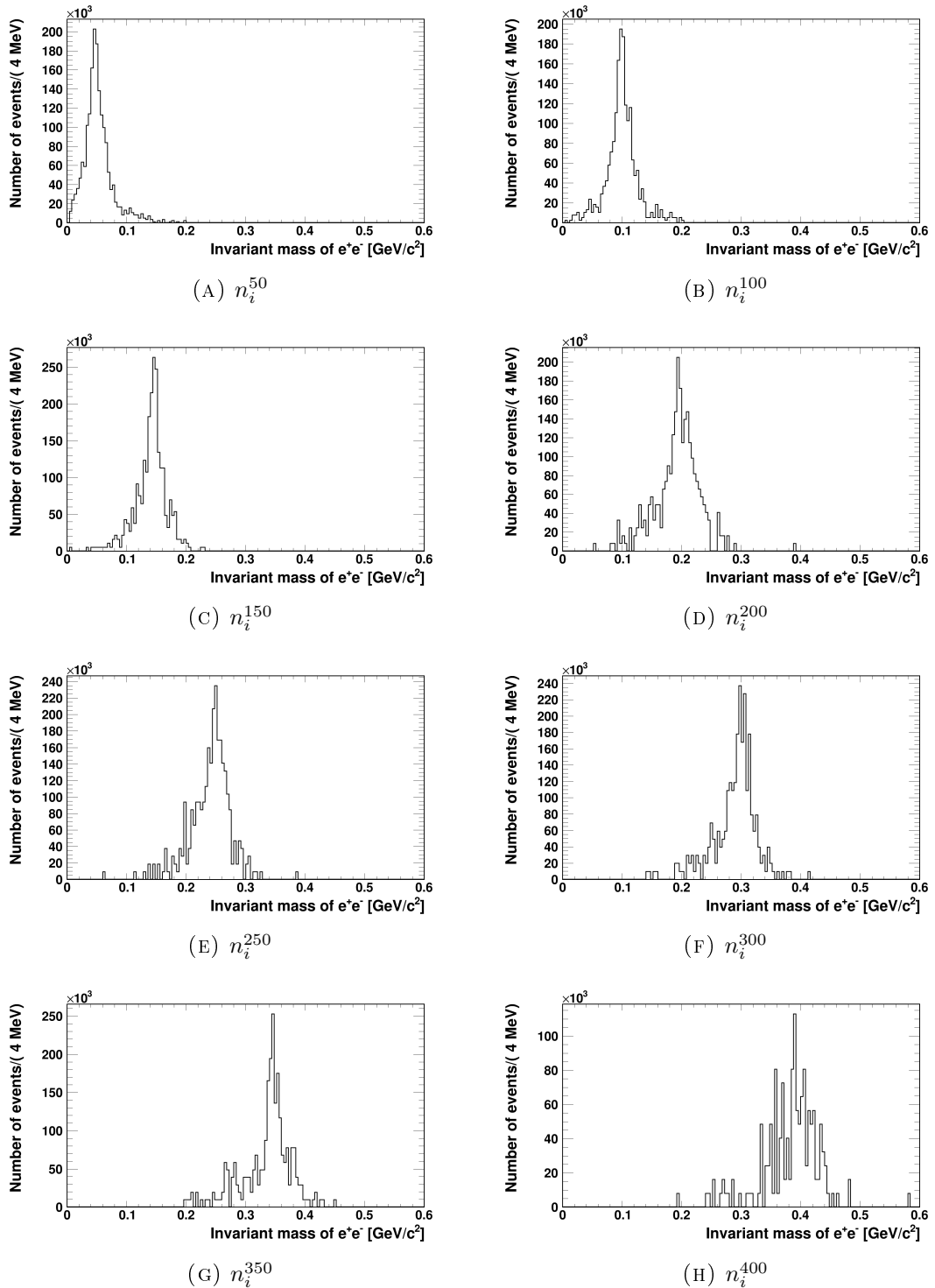
(B) Acceptance of $\eta \rightarrow U(\rightarrow e^+e^-)\gamma$.

FIGURE 8.15: Illustration of reconstruction effects.

FIGURE 8.16: Smearing and acceptance effects for different M_U values.

We solve this equation for each k thus for each U boson true mass M_U (index k). The parameter $\beta = \eta \rightarrow U(\rightarrow e^+e^-)\gamma$ is fitted using the Least Squares Method (implemented in ROOT environment) for each M_U . The figure 8.17 shows the resulting upper limit β as a function of M_U .

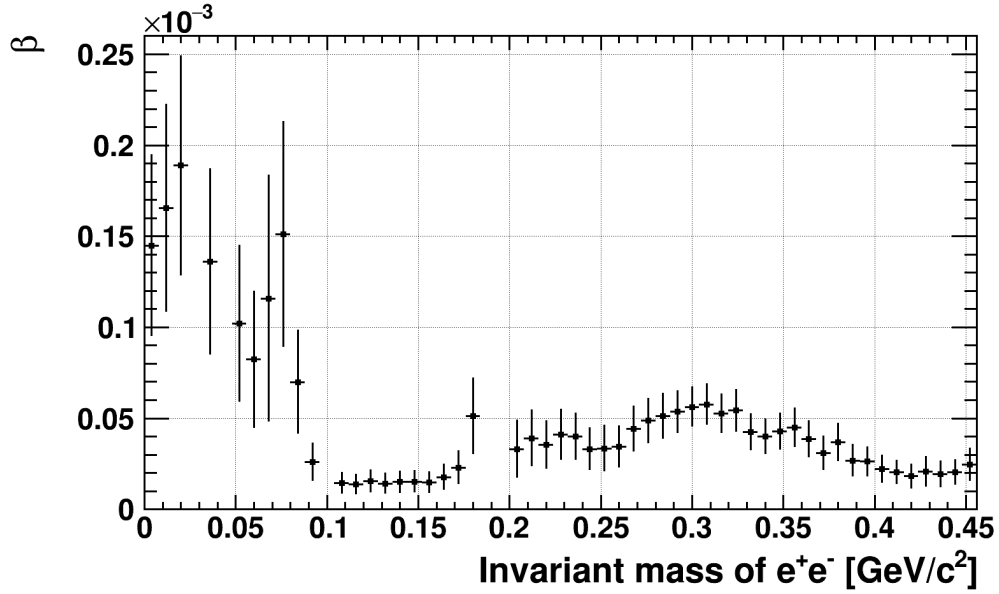


FIGURE 8.17: Upper limit on β as a function of U boson mass M_U .

In order to compare this result with other experiments, we convert the upper limit on β into a limit on the coupling parameter ϵ . We use the following transformation:

$$\epsilon^2 = \frac{\beta}{2BR(\eta \rightarrow \gamma\gamma) \cdot BR(U \rightarrow e^+e^-)} \left(1 - \frac{M_U^2}{M_\eta^2}\right)^{-3} |F(M_U)|^{-2} \quad (8.6)$$

Where,

$$BR(U \rightarrow e^+e^-) = \frac{1}{1 + \sqrt{1 - \frac{4m_\mu^2}{M_U^2}} \left(1 + \frac{2m_\mu^2}{M_U^2}\right)} \quad (8.7)$$

is the branching ratio of the $U \rightarrow e^+e^-$ decay that decreases for $M_U^2 \geq 2m_\mu$ due to the opening of a new decay channel $U \rightarrow \mu^+\mu^-$. The form factor $F(M_U) = \left(1 - \frac{M_U^2}{\Lambda^2}\right)$ is calculated at the η meson mass and $\Lambda = 0.72$ [24] [21].

Figure 8.18 shows the effect of variations of event selection criteria on ϵ^2 calculation. The systematical uncertainties on the ϵ^2 value due the systematical uncertainty on the number of η mesons were investigated and found to be negligible. The final variation of the ϵ^2 limit with U boson mass (e^+e^- invariant mass) is shown on figure 8.19.

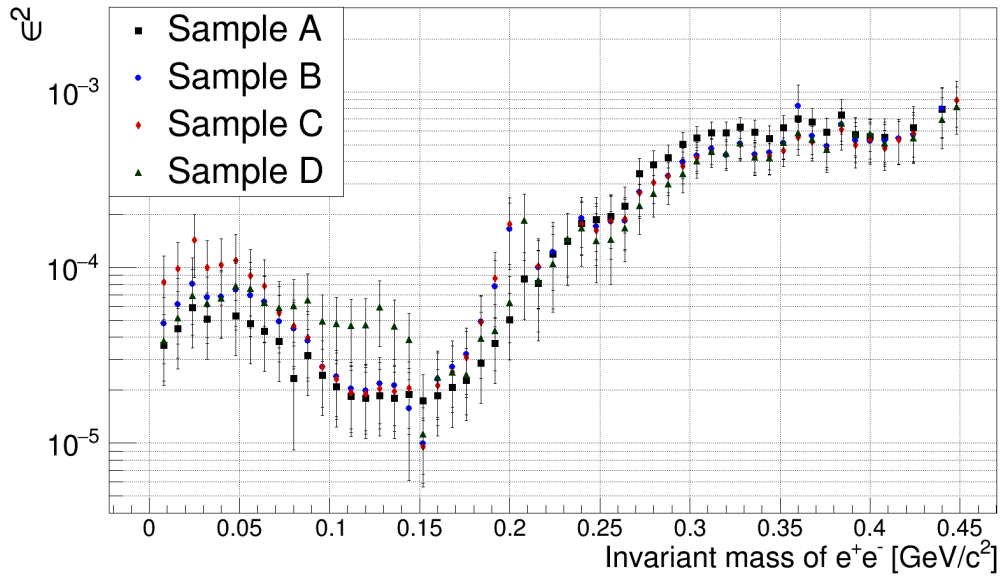


FIGURE 8.18: Upper limit on ϵ^2 as a function of e^+e^- invariant mass (U boson mass). The spread of points reflects the effect of changes in missing mass and time selection.

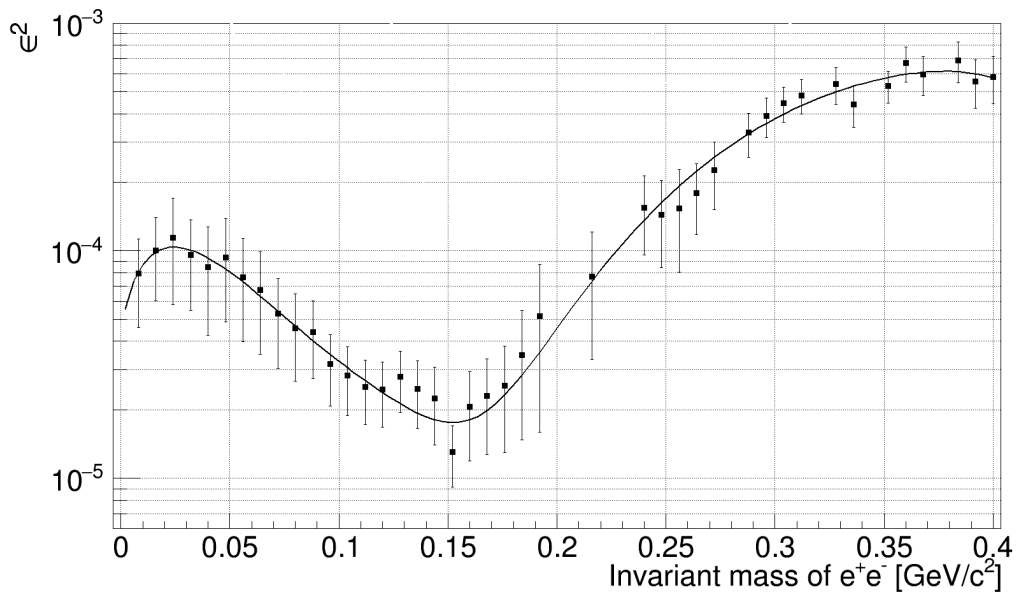


FIGURE 8.19: Upper limit on ϵ^2 as a function of e^+e^- invariant mass (U boson mass).

8.3 Results from $\eta \rightarrow e^+e^-$ channel

After repeating the analysis chain used in [66] to the data sample collected in 2012, we find 191 subsisting $\eta \rightarrow e^+e^-$ candidates. We fit the two proton missing mass distribution with a polynomial representing the background and a Lorentz function that represents the signal. The latter is centered at the η meson mass $547 \text{ MeV}/c^2$ and its width is limited to the $8 - 9 \text{ MeV}/c^2$ range. This constraint on the signal is determined from an $\eta \rightarrow e^+e^-$ Monte Carlo simulation (see figure 8.20). Figures 8.25, 8.26 and 8.27 show fits for different bin widths in a $530 - 580 \text{ MeV}/c^2$ mass range, while figures 8.29, 8.30 and 8.31 regard a $520 - 590 \text{ MeV}/c^2$ mass range.

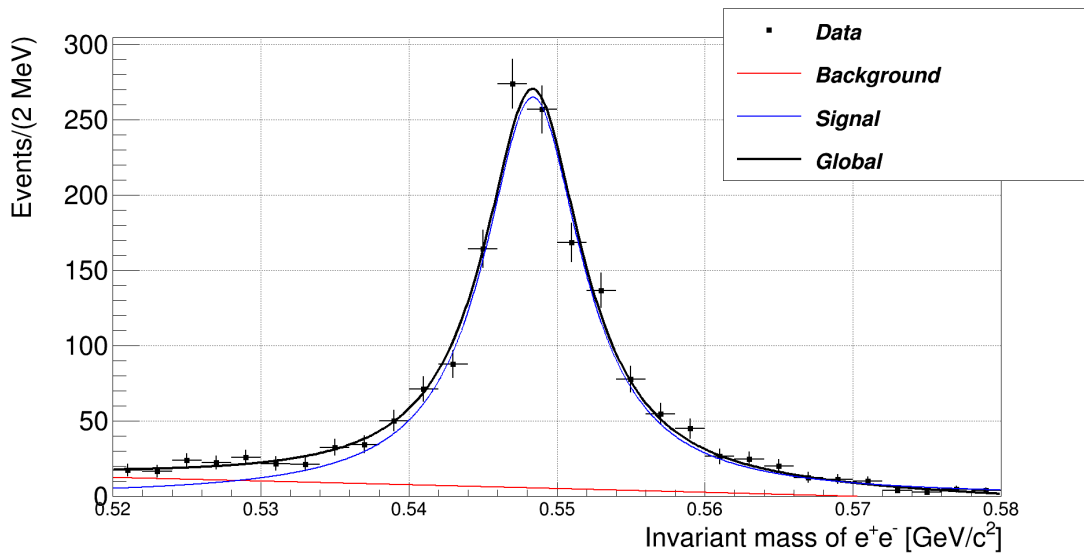


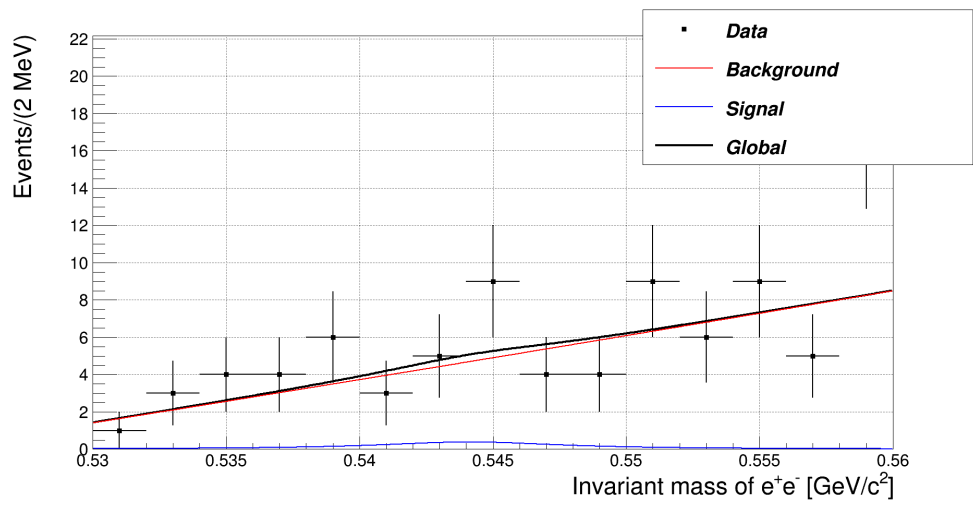
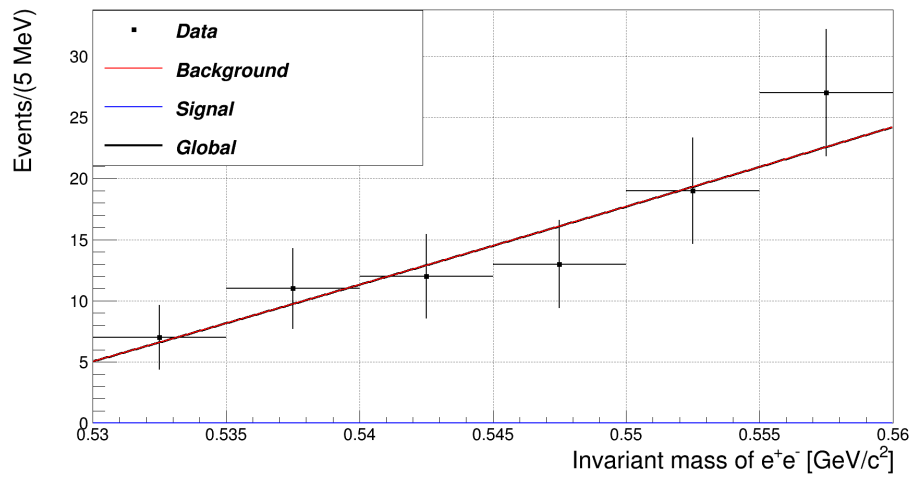
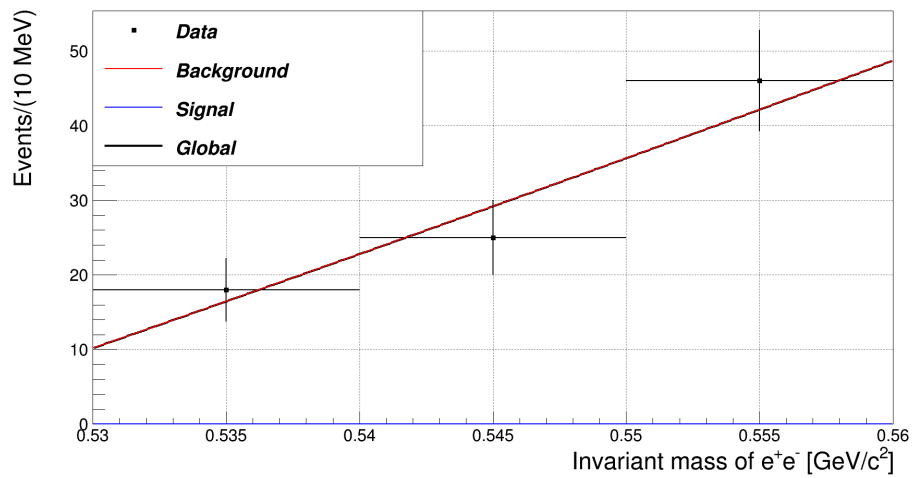
FIGURE 8.20: Fit to the $\eta \rightarrow e^+e^-$ missing mass distribution.

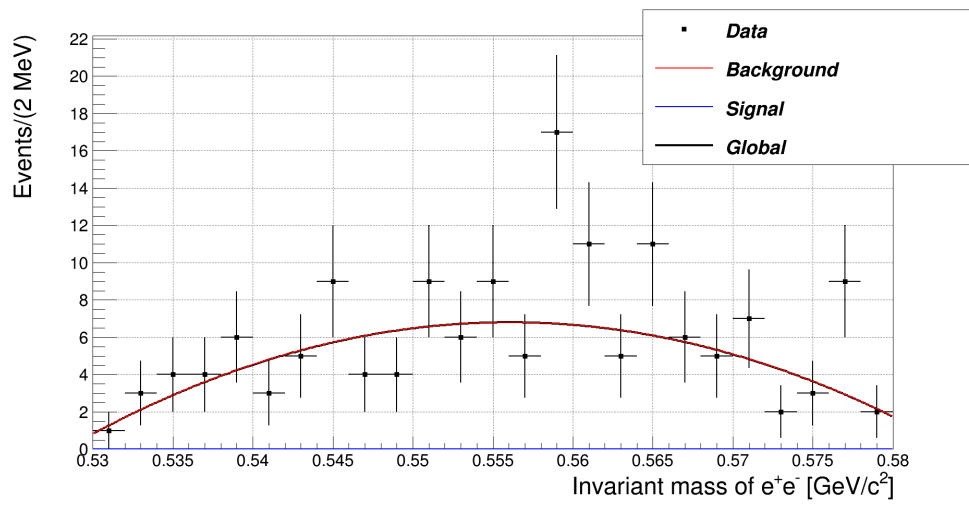
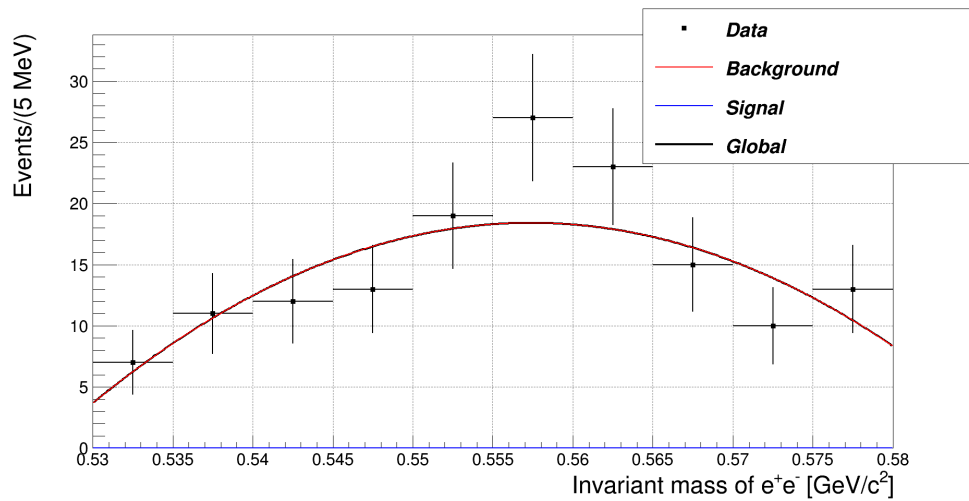
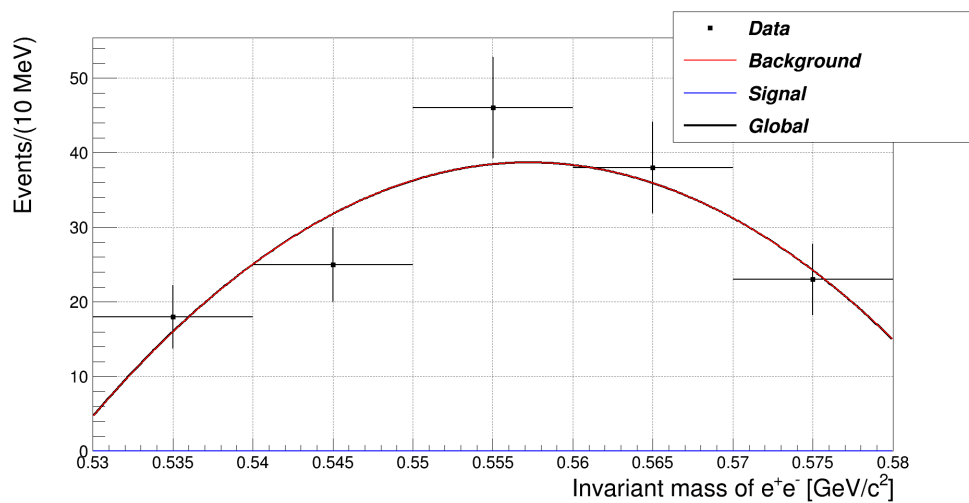
From those fits we can deduce the limit on $\eta \rightarrow e^+e^-$ branching ratio. The formula used is taken from Feldman and Cousins [69]:

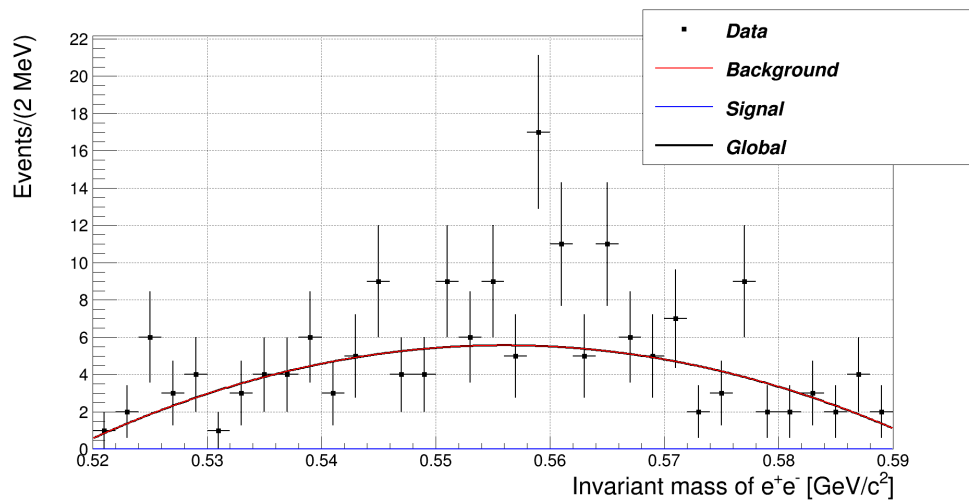
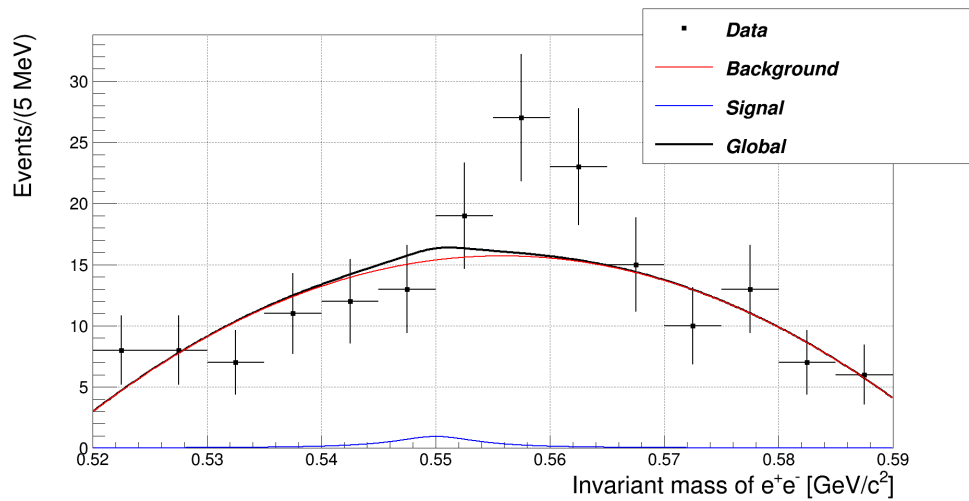
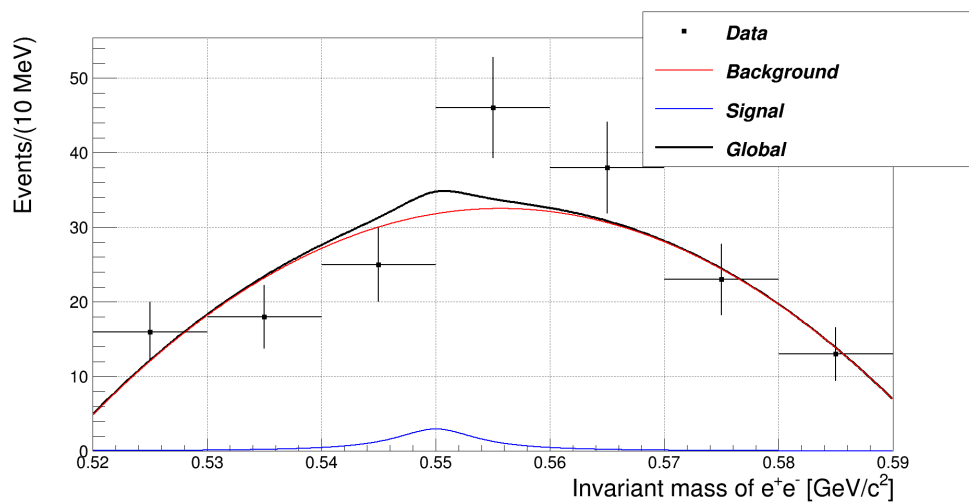
$$BR_{limit} = BR + \lambda \cdot \sigma_{BR} = \frac{(N_{ev} - N_{back}) + \lambda \cdot \sigma_{ev}}{Acc \cdot N_{\eta}} \quad (8.8)$$

where N_{ev} is the number of event candidates with its statistical uncertainty σ_{ev} , N_{back} is the number of background events, Acc is the acceptance on the $\eta \rightarrow e^+e^-$ channel and N_{η} is the number of η mesons present in data.

The λ coefficient depends on the assumed confidence level via the formula:

FIGURE 8.21: 2 MeV/ c^2 bin widthFIGURE 8.22: 5 MeV/ c^2 bin widthFIGURE 8.23: 10 MeV/ c^2 bin widthFIGURE 8.24: Fits to the two protons missing mass (530 – 560 MeV/ c^2 mass range).

FIGURE 8.25: 2 MeV/c^2 bin widthFIGURE 8.26: 5 MeV/c^2 bin widthFIGURE 8.27: 10 MeV/c^2 bin widthFIGURE 8.28: Fits to the two protons missing mass (530 – 580 MeV/c^2 mass range).

FIGURE 8.29: 2 MeV/c^2 bin widthFIGURE 8.30: 5 MeV/c^2 bin widthFIGURE 8.31: 10 MeV/c^2 bin widthFIGURE 8.32: Fits to the two protons missing mass (520 – 590 MeV/c^2 mass range).

$$CL = \int_{-\infty}^{\mu+\lambda\sigma} \frac{1}{\sigma\sqrt{2\pi}} \exp\left[-\frac{1}{2}\left(\frac{x-\mu}{\sigma}\right)^2\right] dx = \frac{1}{2} \left[1 + \operatorname{erf}\left(\frac{\lambda}{\sqrt{2}}\right)\right] \quad (8.9)$$

where the mean μ and its standard deviation σ correspond, in our case, to BR and σ_{BR} . For a 90% confidence level $\lambda = 1.28$.

The table 8.4 summarizes the results of $BR(\eta \rightarrow e^+e^-)$ limit for different fits.

TABLE 8.4: Results of the BR_{limit} fits

	Bin width [MeV/c ²]	BR limit [/10 ⁻⁵]	χ^2
530 – 560 MeV/c ²	2	6.3	1.47
	5	2.8	0.34
	10	1.7	0.58
530 – 580 MeV/c ²	2	2.1	1.37
	5	3.6	1.87
	10	1.7	0.70
520 – 590 MeV/c ²	2	5.3	1.35
	5	4.9	1.65
	10	15.7	8.92

We reject the last measurement given its high χ^2 value. The mean from other fits leads us to the result:

$$BR_{limit}(\eta \rightarrow e^+e^-) = 6.2 \cdot 10^{-5} \quad (8.10)$$

where the systematical and statistical uncertainties were integrated in the upper limit.

8.4 Summary and outlook

Using data collected in 2012 at COSY synchrotron in Jülich (Germany) we selected a large sample (~ 11000) of $\eta \rightarrow e^+e^-\gamma$ events from recorded proton interactions with a windowless frozen hydrogen pellet target. The analysis was exclusive i.e. we selected full events where all particles from the $\eta \rightarrow e^+e^-\gamma$ reaction were reconstructed. In order to limit the initial amount of data, we applied a preliminary selection that distinguished between the neutral and charged decays. Then, we conceived an analysis procedure, based on the analysis of Monte Carlo simulations of various reactions and their interaction with the WASA detector. The η mesons were tagged by the missing mass of the forward scattered protons detected in the FD. To this purpose, the energy calibration of the FD was performed. A particle identification method was tested and applied to data. We have also developed a new identification procedure that could be exploited in further studies. We have studied the trigger efficiency and analyzed a neutral $\eta \rightarrow \gamma\gamma$ decay to extract the number of produced η mesons independently. An estimation of the combinatorial background was done and the resulting distribution was included as an additional background channels. We have reduced all background contributions and demonstrated that we control our data sample by matching the experimental distributions with simulations. A method of non- η background subtraction by fitting the two protons missing mass spectra was developed. The resulting e^+e^- invariant mass spectrum was used to extract the η transition form factor and to search for a hypothetical dark photon.

The transition form factor parameter was found and systematical uncertainties were analyzed leading to the value of $\Lambda^{-2} = 1.97 \pm 0.29_{\text{stat}}^{+0.13_{\text{sys}}} \text{ GeV}^{-2}$.

The search for a dark photon was performed by fitting the whole range of e^+e^- invariant mass distribution and taking into account the experimental resolution (smearing matrix) and the acceptance function. With no signal from a dark boson observed, we have set an upper limit on the coupling parameter between this dark particle and real photons (see figure 8.19).

The data were also used to search for the very rare $\eta \rightarrow e^+e^-$ decay. Since no signal was observed, we used a fitting procedure to set up an upper limit on this channel branching ratio with 90% confidence level: $BR(\eta \rightarrow e^+e^-) < 6.2 \cdot 10^{-5}$.

In the future, data sets from different years can be merged. It would significantly increase the available statistics which would improve all the results presented in this work.

Another possible study would consist in performing an inclusive measurement of the e^+e^- invariant mass distribution. This would allow us to work with statistics larger by about two orders of magnitude.

Bibliography

- [1] G. Aad et al. Observation of a new particle in the search for the Standard Model Higgs boson with the ATLAS detector at the LHC. *Phys. Lett.*, B716:1–29, 2012. doi: 10.1016/j.physletb.2012.08.020.
- [2] S. Chatrchyan et al. Observation of a new boson at a mass of 125 GeV with the CMS experiment at the LHC. *Phys. Lett.*, B716:30–61, 2012. doi: 10.1016/j.physletb.2012.08.021.
- [3] S. Kullander, H. Calen, K. Fransson, A. Kupsc, B. Morozov, R. Ruber, V. Sopov, J. Stepaniak, and V. Chernyshev. Rare eta decays and the CP symmetry. *Acta Phys. Polon.*, B29:97–111, 1998.
- [4] T. Feldmann, P. Kroll, and B. Stech. Mixing and decay constants of pseudoscalar mesons. *Phys. Rev.*, D58:114006, 1998. doi: 10.1103/PhysRevD.58.114006.
- [5] Y. Hsiao, C. Chang, and X. He. A global $SU(3)/U(3)$ flavor symmetry analysis for $B \rightarrow PP$ with $\eta - \eta'$ Mixing. *Phys. Rev.*, D93(11):114002, 2016. doi: 10.1103/PhysRevD.93.114002.
- [6] O. Adriani et al. An anomalous positron abundance in cosmic rays with energies 1.5-100 GeV. *Nature*, 458:607–609, 2009. doi: 10.1038/nature07942.
- [7] O. Adriani et al. Cosmic-Ray Positron Energy Spectrum Measured by PAMELA. *Phys. Rev. Lett.*, 111:081102, 2013. doi: 10.1103/PhysRevLett.111.081102.
- [8] J. Chang et al. An excess of cosmic ray electrons at energies of 300-800 GeV. *Nature*, 456:362–365, 2008. doi: 10.1038/nature07477.
- [9] F. Aharonian et al. The energy spectrum of cosmic-ray electrons at TeV energies. *Phys. Rev. Lett.*, 101:261104, 2008. doi: 10.1103/PhysRevLett.101.261104.
- [10] M. Vecchi. Precision measurement of the $(e^+ + e^-)$ flux in primary cosmic rays from 0.5 GeV to 1 TeV with the Alpha Magnetic Spectrometer on the International Space Station. In *25th European Cosmic Ray Symposium (ECRS 2016)*

- Turin, Italy, September 04-09, 2016, 2017. URL <http://inspirehep.net/record/1508148/files/arXiv:1701.02212.pdf>.
- [11] P. Jean et al. Early SPI / INTEGRAL measurements of 511 keV line emission from the 4th quadrant of the Galaxy. *Astron. Astrophys.*, 407:L55, 2003. doi: 10.1051/0004-6361:20031056.
- [12] P. Fayet. Effects of the Spin 1 Partner of the Goldstino (Gravitino) on Neutral Current Phenomenology. *Phys. Lett.*, B95:285–289, 1980. doi: 10.1016/0370-2693(80)90488-8.
- [13] M. I. Dobroliubov and A. Yu. Ignatiev. Neutral Pion Radiative Decay as an Efficient Tool for Searching for New Light Gauge Bosons. *Phys. Lett.*, B206:346–348, 1988. doi: 10.1016/0370-2693(88)91519-5.
- [14] C. Boehm and P. Fayet. Scalar dark matter candidates. *Nucl. Phys.*, B683:219–263, 2004. doi: 10.1016/j.nuclphysb.2004.01.015.
- [15] J. Alexander et al. Dark Sectors 2016 Workshop: Community Report. 2016. URL <http://inspirehep.net/record/1484628/files/arXiv:1608.08632.pdf>.
- [16] P. Adlarson et al. Search for a dark photon in the $\pi^0 \rightarrow e^+e^-\gamma$ decay. *Phys. Lett.*, B726:187–193, 2013. doi: 10.1016/j.physletb.2013.08.055.
- [17] A. Kotlewski. Preprint. 1973.
- [18] M. R. Jane et al. A Measurement of the Electromagnetic Form-Factor of the eta Meson and of the Branching Ratio for the eta Dalitz Decay. *Phys. Lett.*, B59:103, 1975. doi: 10.1016/0370-2693(75)90168-9. [Erratum: *Phys. Lett.*B73,503(1978)].
- [19] L. G. Landsberg. Electromagnetic Decays of Light Mesons. *Phys. Rept.*, 128:301–376, 1985. doi: 10.1016/0370-1573(85)90129-2.
- [20] R. I. Dzhelyadin et al. Investigation of η Meson Electromagnetic Structure in $\eta \rightarrow \mu^+\mu^-\gamma$ Decay. *Phys. Lett.*, B94:548, 1980. doi: 10.1016/0370-2693(80)90937-5. [*Yad. Fiz.*32,998(1980)].
- [21] R. Arnaldi et al. Study of the electromagnetic transition form-factors in $\eta \rightarrow \mu^+\mu^-\gamma$ and $\omega \rightarrow \mu^+\mu^-\pi^0$ decays with NA60. *Phys. Lett.*, B677:260–266, 2009. doi: 10.1016/j.physletb.2009.05.029.
- [22] R. Arnaldi et al. Precision study of the $\eta \rightarrow \mu^+\mu^-\gamma$ and $\omega \rightarrow \mu^+\mu^-\pi^0$ electromagnetic transition form-factors and of the $\rho \rightarrow \mu^+\mu^-$ line shape in NA60. *Phys. Lett.*, B757:437–444, 2016. doi: 10.1016/j.physletb.2016.04.013.

- [23] M. N. Achasov et al. Search for the radiative decay $\eta \rightarrow \pi^0 \gamma \gamma$ in the SND experiment at VEPP-2M. *Nucl. Phys.*, B600:3–20, 2001. doi: 10.1016/S0550-3213(01)00040-2.
- [24] H. Berghauer et al. Determination of the η -transition form factor in the $\gamma p \rightarrow p\eta \rightarrow p\gamma e^+e^-$ reaction. *Phys. Lett.*, B701:562–567, 2011. doi: 10.1016/j.physletb.2011.06.069.
- [25] C. Terschlusen and S. Leupold. Electromagnetic transition form factors of light vector mesons. *Phys. Lett.*, B691:191–201, 2010. doi: 10.1016/j.physletb.2010.06.033.
- [26] P. Adlarson et al. Measurement of the $\omega \rightarrow \pi^0 e^+e^-$ and $\eta \rightarrow e^+e^-\gamma$ Dalitz decays with the A2 setup at MAMI. *Phys. Rev.*, C95(3):035208, 2017. doi: 10.1103/PhysRevC.95.035208.
- [27] B. D. Hyams, W. Koch, D. C. Potter, L. Von Lindern, E. Lorenz, G. Luetjens, U. Stierlin, and P. Weilhammer. Observation of the $\mu^+\mu^-$ decay mode of the η -neutral meson. *Phys. Lett.*, 29B:128–131, 1969. doi: 10.1016/0370-2693(69)90264-0.
- [28] H. J. Behrend et al. A Measurement of the π^0 , η and η' electromagnetic form-factors. *Z. Phys.*, C49:401–410, 1991. doi: 10.1007/BF01549692.
- [29] J. Gronberg et al. Measurements of the meson - photon transition form-factors of light pseudoscalar mesons at large momentum transfer. *Phys. Rev.*, D57:33–54, 1998. doi: 10.1103/PhysRevD.57.33.
- [30] A. E. Dorokhov. Rare decay $\pi^0 \rightarrow e^+e^-$ as a Test of Standard Model. *Phys. Part. Nucl. Lett.*, 7:229–234, 2010. doi: 10.1134/S1547477110040023.
- [31] E. Abouzaid et al. Measurement of the Rare Decay $\pi^0 \rightarrow e^+e^-$. *Phys. Rev.*, D75:012004, 2007. doi: 10.1103/PhysRevD.75.012004.
- [32] A. E. Dorokhov. Recent results on rare decay $\pi^0 \rightarrow e^+e^-$. *Nucl. Phys. Proc. Suppl.*, 181-182:37–41, 2008. doi: 10.1016/j.nuclphysbps.2008.09.018.
- [33] M. J. Savage, M. E. Luke, and M. B. Wise. The Rare decays $\pi^0 \rightarrow e^+e^-$, $\eta \rightarrow e^+e^-$ and $\eta \rightarrow \mu^+\mu^-$ in chiral perturbation theory. *Phys. Lett.*, B291:481–483, 1992. doi: 10.1016/0370-2693(92)91407-Z.
- [34] D. Gomez Dumm and A. Pich. Long distance contributions to the $K_L \rightarrow \mu^+\mu^-$ decay width. *Phys. Rev. Lett.*, 80:4633–4636, 1998. doi: 10.1103/PhysRevLett.80.4633.

- [35] A. E. Dorokhov and M. A. Ivanov. Rare decay $\pi^0 \rightarrow e^+e^-$: Theory confronts KTeV data. *Phys. Rev.*, D75:114007, 2007. doi: 10.1103/PhysRevD.75.114007.
- [36] T. Petri. *Anomalous decays of pseudoscalar mesons*. PhD thesis, Institut für Kernphysik Forschungszentrum, Jülich, Germany, 2010.
- [37] A. E. Dorokhov, M. A. Ivanov, and S. G. Kovalenko. Complete structure dependent analysis of the decay $P \rightarrow l^+l^-$. *Phys. Lett.*, B677:145–149, 2009. doi: 10.1016/j.physletb.2009.05.033.
- [38] M. Knecht, S. Peris, M. Perrottet, and E. de Rafael. Decay of pseudoscalars into lepton pairs and large N(c) QCD. *Phys. Rev. Lett.*, 83:5230–5233, 1999. doi: 10.1103/PhysRevLett.83.5230.
- [39] M. Berłowski et al. Measurement of eta meson decays into lepton-antilepton pairs. *Phys. Rev.*, D77:032004, 2008. doi: 10.1103/PhysRevD.77.032004.
- [40] G. Agakishiev et al. Inclusive dielectron spectra in p+p collisions at 3.5 GeV. *Eur. Phys. J.*, A48:64, 2012. doi: 10.1140/epja/i2012-12064-y.
- [41] D. Prasuhn, J. Dietrich, R. Maier, R. Stassen, H. J. Stein, and H. Stockhorst. Electron and stochastic cooling at COSY. *Nucl. Instrum. Meth.*, A441:167–174, 2000. doi: 10.1016/S0168-9002(99)01128-6.
- [42] H. Stockhorst, R. Maier, D. Prasuhn, R. Stassen, and T. Katayama. Stochastic Momentum Cooling Experiments with a Barrier Bucket Cavity and Internal Targets at COSY-Julich in Preparation for HESR at FAIR. *Conf. Proc.*, C100523:MOPD068, 2010.
- [43] B. Trostell. Vacuum injection of hydrogen microsphere beams. *Nucl. Instrum. Meth.*, A362:41–52, 1995. doi: 10.1016/0168-9002(95)00302-9.
- [44] C. Ekstrom, C. J. Friden, A. Jansson, S. Kullander, A. Larsson, G. Norman, and J. Karlsson. Hydrogen pellet targets for circulating particle beams. *Nucl. Instrum. Meth.*, A371:572–574, 1996. doi: 10.1016/0168-9002(96)00009-5.
- [45] M. Jacewicz. *Measurement Of The Reaction Proton-proton Decaying To Proton-proton-pion(+)-pion(-)-pions With Celsius/wasa At 1.36 Gev*. PhD thesis, Uppsala U., 2004.
- [46] R. J. M. Y. Ruber. *An ultrathin walled superconducting solenoid for meson decay physics*. PhD thesis, Uppsala U., 1999. URL <http://wwwlib.umi.com/dissertations/fullcit?p181697>.

- [47] C. Bargholtz et al. The WASA Detector Facility at CELSIUS. *Nucl. Instrum. Meth.*, A594:339–350, 2008. doi: 10.1016/j.nima.2008.06.011.
- [48] D. Lersch. *Investigation of dipion final state interactions in $pp \rightarrow pp[\eta \rightarrow \pi^+\pi^-\gamma]$* . PhD thesis, Fachbereich für Mathematik und Naturwissenschaften der Bergischen Universität Wuppertal, 2014.
- [49] I. Frohlich et al. Pluto: A Monte Carlo Simulation Tool for Hadronic Physics. *PoS, ACAT2007:076*, 2007.
- [50] R. Schicker et al. Acceptance and resolution simulation studies for the dielectron spectrometer HADES at GSI. *Nucl. Instrum. Meth.*, A380:586–596, 1996. doi: 10.1016/0168-9002(96)00732-2.
- [51] F. James. Monte-Carlo phase space. 1968.
- [52] R. Brun, F. Bruyant, F. Carminati, S. Giani, M. Maire, A. McPherson, G. Patrick, and L. Urban. GEANT Detector Description and Simulation Tool. 1994.
- [53] S. Burkhard, B. Thomas, H. Fabio, M. Guilherme, R. Peter, and W. Martin. GEANT - Detector Description and Simulation Tool. Technical report, CERN, 1993.
- [54] W. G. Jones, D. M. Binnie, A. Duane, J. P. Horsey, and D. C. Mason. η Production near Threshold. *Phys. Lett.*, 23:597, 1966. doi: 10.1016/0031-9163(66)91016-X.
- [55] W. B. Richards et al. Production and neutral decay of the η meson in π^-p collisions. *Phys. Rev.*, D1:10–19, 1970. doi: 10.1103/PhysRevD.1.10.
- [56] F. Bulos et al. Charge exchange and production of eta mesons and multiple neutral pions in π^-p reactions between 654 and 1247 MeV/c². *Phys. Rev.*, 187:1827–1844, 1969. doi: 10.1103/PhysRev.187.1827.
- [57] M. Batinic, A. Svarc, and T. S. H. Lee. Near threshold η production in proton proton collisions. *Phys. Scripta*, 56:321–324, 1997. doi: 10.1088/0031-8949/56/4/001.
- [58] H. Calen et al. The $pp \rightarrow pp\eta$ reaction near the kinematical threshold. *Phys. Lett.*, B366:39–43, 1996. doi: 10.1016/0370-2693(95)01313-X.
- [59] A. M. Bergdolt et al. Total cross-section of the $pp \rightarrow pp\eta$ reaction near threshold. *Phys. Rev.*, D48:R2969–R2973, 1993. doi: 10.1103/PhysRevD.48.R2969.
- [60] P. Adlarson et al. Measurement of the $\omega \rightarrow \pi^+\pi^-\pi^0$ Dalitz plot distribution. *Phys. Lett.*, B770:418–425, 2017. doi: 10.1016/j.physletb.2017.03.050.

- [61] B. Krusche and C. Wilkin. Production of η and η' mesons on nucleons and nuclei. *Prog. Part. Nucl. Phys.*, 80:43–95, 2014. doi: 10.1016/j.pnpnp.2014.10.001.
- [62] E. L. Bratkovskaya, O. V. Teryaev, and V. D. Toneev. Anisotropy of dilepton emission from nuclear collisions. *Phys. Lett.*, B348:283–289, 1995. doi: 10.1016/0370-2693(95)00164-G.
- [63] H. Leutwyler. Implications of eta eta-prime mixing for the decay $\eta \rightarrow 3\pi$. *Phys. Lett.*, B374:181–185, 1996. doi: 10.1016/0370-2693(96)00167-0.
- [64] C. Amsler et al. eta decays into three pions. *Phys. Lett.*, B346:203–207, 1995. doi: 10.1016/0370-2693(95)00094-2.
- [65] P. Adlarson et al. $\pi^0\pi^0$ production in proton-proton collisions at $T_p = 1.4$ GeV. *Phys. Lett.*, B706:256–262, 2012. doi: 10.1016/j.physletb.2011.11.041.
- [66] M. Berłowski. *Study of η meson leptonic decays with WASA detector*. PhD thesis, National Centre for Nuclear Research, 2013.
- [67] M. Hodana. *Study of the $\eta \rightarrow e^+e^-\gamma$ decay using WASA-at-COSY detector system*. PhD thesis, Jagiellonian University, Cracow, 2012.
- [68] B. Himani. *Study of a rare decay $\eta \rightarrow e^+e^-\gamma$ using WASA-at-COSY*. PhD thesis, Department of Physics, Indian Institute of Technology, Bombay, 2011.
- [69] G. J. Feldman and R. D. Cousins. A Unified approach to the classical statistical analysis of small signals. *Phys. Rev.*, D57:3873–3889, 1998. doi: 10.1103/PhysRevD.57.3873.